ASSESSMENT OF ADAPTIVE GUIDANCE FOR REUPONSIVE LAUNCH VEHICLES AND SPACECRAFT

"

Ping Lu

Iowa State University
Department of Aerospace Engineering
2271 Howe Hall
Ames, IA 50011-2271

29 April 2009

Final Report

AIR FORCE RESEARCH LABORATORY
Space Vehicles Directorate
3550 Aberdeen Ave SE
AIR FORCE MATERIEL COMMAND
KIRTLAND AIR FORCE BASE, NM 87117-5776

//signature//

//signature//

_____

Frank R. Chavez, Program Manager

_____

WADE H. VAUGHT, Lt Col, USAF
  Acting Chief, Integrated Experiments
    and Evaluation Division

REPORT DOCUMENTATION PAGE

1. REPORT DATE (DD-MM-YYYY)	2. REPORT TYPE	3. DATES COVERED (From - To)
29-04-2009	Final Report	20-04-2005 - 29-01-2009

4. TITLE AND SUBTITLE	5a. CONTRACT NUMBER
Assessment of Adaptive Guidance for Responsive Launch Vehicles and Spacecraft	FA9453-05-C-0268
	5b. GRANT NUMBER
	5c. PROGRAM ELEMENT NUMBER 63401F

6. AUTHOR(S)	5d. PROJECT NUMBER 2181
Ping Lu	5e. TASK NUMBER SW
	5f. WORK UNIT NUMBER 7S

7. PERFORMING ORGANIZATION NAME(S) AND ADDRESS(ES)	8. PERFORMING ORGANIZATION REPORT NUMBER
Iowa State University Department of Aerospace Engineering 2271 Howe Hall Ames, IA 50011-2271	

9. SPONSORING / MONITORING AGENCY NAME(S) AND ADDRESS(ES)	10. SPONSOR/MONITOR'S ACRONYM(S) AFRL/RVES
Air Force Research Laboratory Space Vehicles Directorate 3550 Aberdeen Ave SE Kirtland AFB, NM 87117-5776	11. SPONSOR/MONITOR'S REPORT NUMBER(S) AFRL-RV-PS-TR-2009-1023

12. DISTRIBUTION / AVAILABILITY STATEMENT
Approved for public release; Distribution is unlimited. (377ABW-2009-0721 dated 08 Jun 2009.)

13. SUPPLEMENTARY NOTES

14. ABSTRACT
This project sets out to identify and address the need for adaptive ascent guidance techniques necessary for responsive launch. This report provides comprehensive details to two recent advanced ascent guidance algorithms, tailored to endo-atmospheric and exo-atmospheric optimal ascent with possibly multiple stages, respectively. These algorithms generate optimal ascent guidance commands based on the current state of the vehicle, the currently selected targeting condition, and available vehicle/environment modeling and wind information. The algorithms depend on no vehicle-specific characteristics therefore are applicable to different types of launch vehicles without the need for significantly modifying the software. Verification, validation and extensive testing of the algorithms are performed with many mission scenarios and a number of different launch vehicle configurations, including winged reusable and conventional expandable, single-stage and multiple-stage, launch vehicles. This work demonstrates that promising techniques and algorithms have reached a level where launch ascent planning can benefit from automation based on these advances to significantly reduce ascent guidance planning time and potential realization of fully closed-loop optimal ascent guidance from liftoff to orbital insertion is possible.

15. SUBJECT TERMS
Launch vehicles; Responsive launch, Ascent guidance; Adaptive guidance; Trajectory optimization

16. SECURITY CLASSIFICATION OF:			17. LIMITATION OF ABSTRACT	18. NUMBER OF PAGES	19a. NAME OF RESPONSIBLE PERSON Dr. Frank R. Chavez
a. REPORT Unclassified	**b. ABSTRACT** Unclassified	**c. THIS PAGE** Unclassified	Unlimited	122	**19b. TELEPHONE NUMBER**

This page is intentionally left blank.

Table of Contents

List of Figures

vi

List of Tables

This page is intentionally left blank.

1

Summary

This project sets out to identify and address the need for adaptive ascent guidance techniques necessary for responsive launch. The required short response time and potential unavailability of mission scenario specifics dictate that the conventional launch ascent guidance technology, which relies heavily on pre-mission planning and requires significant lead time, is simply incompatible to the needs in responsive launch. This report provides comprehensive details to two recent advanced ascent guidance algorithms, tailored to endo-atmospheric and exo-atmospheric optimal ascent, respectively. These algorithms generate *optimal* ascent guidance commands based on the current state of the vehicle, the currently selected targeting condition, and available vehicle/environment modeling and wind information. Should any in-flight changes occur in vehicle condition, vehicle health status, and mission objective (such as call back and change of targeting condition), the guidance algorithms would be able to adapt to the changes. Throughout the report, verification, validation and extensive testing of the algorithms have been performed with many mission scenarios and a number of different launch vehicle configurations, including winged reusable and conventional expandable, single-stage and multiple-stage, launch vehicles. This work has clearly demonstrated that promising techniques and algorithms have reached a level where they could potentially lead to fully automated closed-loop optimal ascent guidance from liftoff to orbital insertion. It is strongly recommended that continuing efforts be made to further enhance, develop, and mature these algorithms and techniques to pave the way to their eventual adaptation in launch operations.

2

Introduction

2.1   State of Current Launch Ascent Guidance Technology

The Air Force's interests in achieving operationally responsive launch and executing time-critical, global-reach missions from space require far greater autonomy, flexibility, and capability of the guidance systems than currently exist for launch vehicles and entry spacecraft. The driving motivation for this research is that the challenges for realizing responsive access to and from space lie not only in hardware and operations, but also equally in software and algorithms. Traditionally, launch and entry guidance and control (G&C) software and parameters are designed for a specified mission, payload, and targeting condition. In ascent guidance, the current technology employs open-loop ascent guidance during the atmospheric portion of the flight. The guidance commands are generated on the ground based on the orbital insertion conditions, vehicle Modeling, and vehicle load and integrity constraints. Prior to launch, the day-of-launch wind profile is used to update the ascent guidance commands which are then uploaded into the launch vehicle. Such elaborate planning and updates are essential for the open-loop guidance to ensure that the load limits will not be exceeded during ascent in the inevitable presence of winds, the performance is optimal, and the targeting conditions can be met. But this is a time-consuming and labor-intensive process, done well in advance of the actual mission. In 2004 the Missile Defense Agency reported that it typically take up to 6 months to update, re-validate, and check out the guidance and control software and I-loads when targeting conditions and mission parameters change. See MDA04-103, Research Project Call "Flexible, Rapid Launch Vehicle Control Software Generation and Checkout". The following is the excerpt:

Current inability to rapidly generate and test launch vehicle control software limits MDA's capability for responding to late-developing modifications to test requirements that affect ballistic missile target presentations. If modifications to test requirements involve changes to target flight dynamics, trajectory, separation events, etc., software for launch vehicle control must be re-generated, verified, re-installed, and validated in the launch vehicle through check-out procedures to include integrated testing. For multi-stage vehicles, typical times for developing guidance, navigation and control (GN&C) software alone approach **six months**...

In crewed launch missions, the lead time required for planning is even longer, up to **two years**. Below is the personal communication from a senior engineer working in the Flight Dynamics Department for the Space Shuttle, in response to the inquiry on Shuttle launch planning related to GN&C and the man-power requirement:

The Space Shuttle flight design process can take anywhere from **9 months to 2 years,** *depending on the mission. Flights that involve unique payloads are more complex, the most recent example that I can think of would be STS-93 the deploy of the Chandra observatory. That payload was very heavy with an aft CG that made the design of Ascent Abort trajectories a challenge, particularly the glided side of the abort with full OMS pods, and a heavy payload. Recently however, all the flights are going to the International Space Station which has simplified the flight design process since all the flights now have similar weight and trajectory constraints (51.6 deg. Inclination, ground up rendezvous with ISS, and medium sized payloads due to limitations on payload mass to high inclination orbits). This has also helped with the flight design for STS-300, which is a Launch on Need (LON) rescue flight to the ISS. If the orbiter gets damaged and can not return, we would get out the STS-300 trajectory products and refine them for the current situation and launch within 40 days.*

On the days prior to launch a small group of people work to update, many of the ascent I-loads (see below for a definition of I-Load) for the conditions on launch day, this is called the "Day of Launch I-Load Update (DOLILU, pronounced "doll ee lou"). Atmospheric conditions (winds, and atmospheric density), and final estimates of propellant loading all factor into these final adjustments to the Iloads. Items that get updated: First stage steering commands, Throttle bucket, OMS Assist quantity, etc. DOLILU team 6-10 people.

The Flight Design and Dynamics department has about **350** *employees that do everything from simulation software modification and maintenance to the actual I-load design. Many of these people are dedicated to areas that would not apply to other launch vehicles like Ascent Aborts, Entry, and Orbit Operations. Additionally, there is a significant amount of effort that goes into producing crew procedures, and many of the people in this department also work on console during the mission. Also they are staffed to support a flight rate of 6-8 flights a year plus development of new programs.*

2.2   Benefits and Objectives of the Research

Until the technical challenges in update and design of G&C algorithms and software on a short notice are satisfactorily addressed, on-demand launch would not be realistic even for a vehicle already on the launch pad or in orbit. Adaptive closed-loop ascent guidance technology through the atmosphere is not only desirable, but may be necessary to truly achieve on-demand responsive space launch.

Listed below are some of the major benefits of such an adaptive closed-loop ascent guidance technology that are unmatched by the open-loop guidance, and directly tied to the Air Force's goal of responsive, reliable and affordable access to space:

- Significantly shortened pre-launch guidance preparation. With closed-loop ascent guid-

ance, there is little or no need for off-line guidance planning and analysis. The day-of-launch wind data can be incorporated into the guidance algorithm. Therefore, pre-launch guidance command update is unnecessary. In fact, when and if in-flight means for real-time wind speed measurement becomes available, the measured wind profile could be directly fed to the closed-loop ascent guidance algorithm which in turn would generate corresponding optimal guidance commands. In such a scenario the pre-launch process of taking wind measurements, which typically takes hours, could even be eliminated.

- Operational flexibility. Closed-loop ascent guidance would be fully automated and require no labor-intensive pre-mission analysis and re-planning whenever the mission profile changes. Last-minute changes of the target orbit in time-critical missions could be easily handled by the guidance system. Even in-flight change of target orbit could be possible.

- Dramatically reduced reoccurring costs related to guidance. The same features of the closed-loop ascent guidance that provide operational flexibility also result in greatly reduced need for human intervention. Thus the operational costs related to ascent guidance could be reduced to minimum.

- Fault Tolerance. A closed-loop ascent guidance system is capable of adapting to severe off-nominal conditions. It could readily make use of vehicle health information, accommodate recoverable system failures, and still successfully complete the mission. An example is the failure of one engine (or multiple engines, as long as the remaining engines can still put the vehicle into orbit). The closed-loop ascent guidance algorithm could compute new optimal guidance commands based on the remaining thrust of the vehicle, and guide the vehicle to fly a different (longer) trajectory to the target orbit.

In pursuit of the required technical advances in realizing adaptive ascent guidance, the chief goals of this project are as follows:

1. Identify and evaluate advanced algorithms that may be the candidate for rapid space launch mission planning and potentially closed-loop endo-atmospheric ascent guidance. Develop new algorithm or enhancements to an existing algorithm where appropriate.

2. Develop robust, reliable and fast exo-atmospheric ascent guidance algorithm for optimal ascent of multi-stage launch vehicles. The algorithm should allow full autonomous guidance for optimal coasts between two burns/stages.

3. Integrate the endo- and exo-atmospheric optimal ascent guidance algorithms for complete end-to-end launch operations.

4. Develop testing scenarios and evaluation metrics to test the ascent guidance algorithms; validate the algorithms with other existing standard aerospace industry trajectory software.

5. Demonstrate the applicability and versatility of the ascent guidance algorithms to widely different launch vehicle configurations, including winged reusable launch vehicle and axial-symmetric expendable launch vehicle.

This final report is organized in accordance with the above stated goals.

3

Coordinate Systems

The need to define appropriate coordinate systems arises from two considerations. First, there may be some particular coordinate system in which the position and velocity of the flight vehicle "make sense". For navigation we are concerned with position and velocity with respect to the Earth, whereas for vehicle aerodynamic performance we need position and velocity with respect to the atmosphere. Second, there are coordinate systems in which the phenomena of interest are most naturally expressed. The direction of a rocket's thrust may often be considered fixed with respect to the body of the vehicle. There are three

coordinate systems used in this report – Earth Centered Inertial coordinate system (ECI), guidance coordinate system (or launch plumbline frame), and vehicle body frame. This section provides descriptions of above three coordinate systems and of the algorithms used to transform quantities between different systems.

3.1   Earth Centered Inertial Coordinate System $X_I Y_I Z_I$

As its name suggests this coordinate system has its origin at the center of the Earth. The z-axis Z_I is parallel to the Earth's rotation axis (positive to the North). It is assumed that the x-axis X_I points toward the intersection of the Equator and the Greenwich Meridian at the time of launch (this is a simplification that can be easily removed). The y-axis Y_I completes the right-hand coordinate system. Thus it is convenient for specifying the location of ground stations and ground-based experiments as these are fixed quantities in the ECI system.

When ECI coordinates are expressed in spherical form, the latitude component is identical to what is termed geocentric latitude by astronomers and geographers. However, note that this is different to the system of geodetic latitude used in normal map-making. The geodetic latitude at any location is the angle between the equatorial plane and the local normal to the Earth's surface. In general that normal is not parallel to a radius vector because the shape of the Earth is an oblate spheroid and not a sphere.
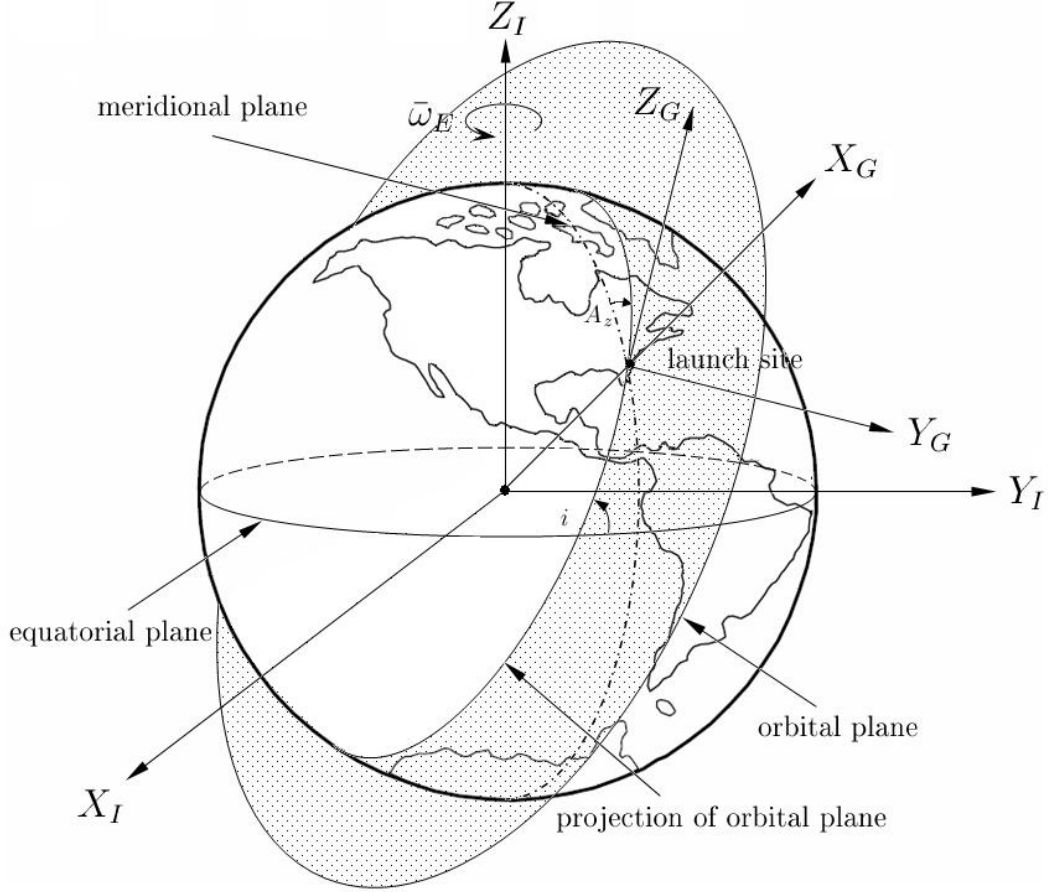
Figure 1: Earth centered inertial and launch plumbline coordinate systems

3.2   Launch Guidance (Plumbline) System $X_P Y_P Z_P$

The guidance system is an inertial system, which is also called the inertial launch plumbline coordinate system whose origin is at the center of the Earth. The x-axis X_P is defined from the center of the Earth, parallel to the gravity direction at the launch site and positive up (the same as X_G in Fig. 1). The z-axis Z_P is pointing downrange along the launch azimuth direction and the y-axis Y_P completes the right-hand system. The $X_P Y_P Z_P$ frame has its axes parallel (or coincide in the case of the x-axis) with those of the $X_G Y_G Z_G$ frame in Fig. 1, except that the latter has its origin at the launch site. The longitude and geocentric latitude of the launch site is defined by (Θ, Φ_c). The launch azimuth A_z for an ascending orbit is defined by

$$A_z = \sin^{-1}\left(\frac{\cos i}{\cos \Phi_c}\right) \qquad \text{for ascending orbit}$$

$$A_z = \frac{\pi}{2} + \sin^{-1}\left(\frac{\cos i}{\cos \Phi_c}\right) \qquad \text{for descending orbit}$$

(1)

where i is the target orbital inclination.
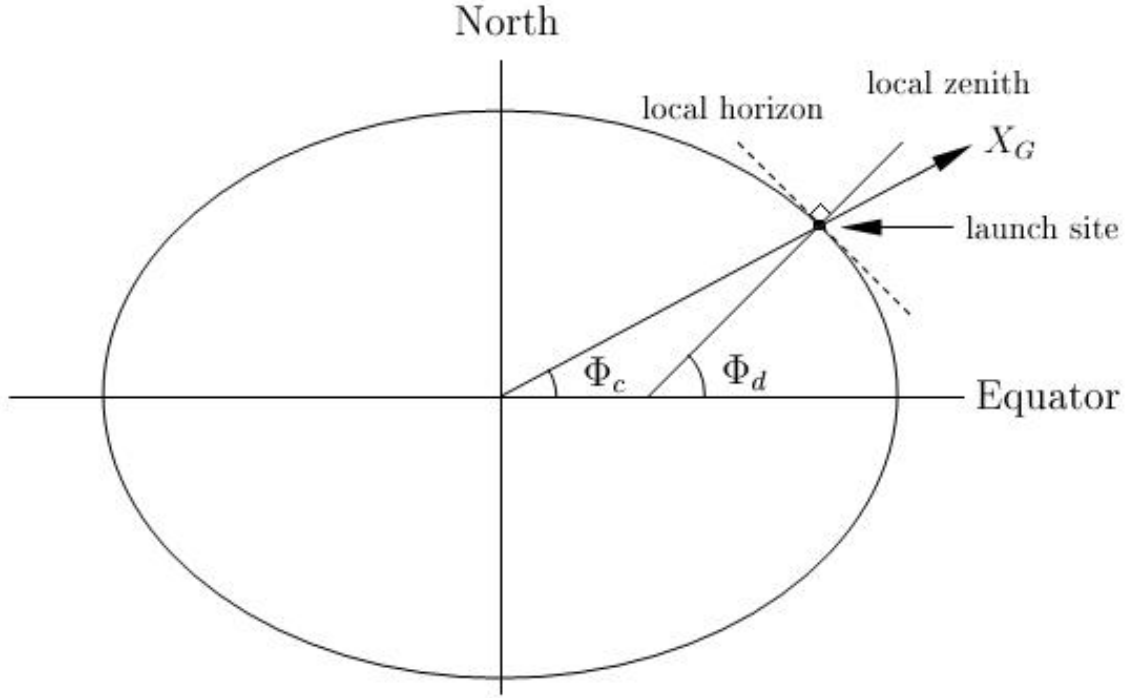
Figure 2: Geodetic and geocentric latitude

Note that geocentric latitude Φ_c is used instead of geodetic latitude Φ_d. The geocentric latitude of a point is the angle between the equatorial plane and a ray through the point from the Earth's center. The geodetic latitude is the angle between the local zenith and the equatorial plane. Due to the Earth's oblateness, geodetic latitudes (the most common form of Earth location) are slightly greater than geocentric latitudes except at the equator and poles where they are identical. The relationship between Φ_c and Φ_d is given by

$$\tan \Phi_c = (1 - e^2) \tan \Phi_d \tag{2}$$

where $e = 0.0818191$ is the eccentricity of the Earth.

3.3   North-East-Down (NED) System

This is an inertial system with the origin at the launch site at the launch time. The x-axis points to the North, the y-axis to the local East, and the z-axis completes a right-hand system (down).
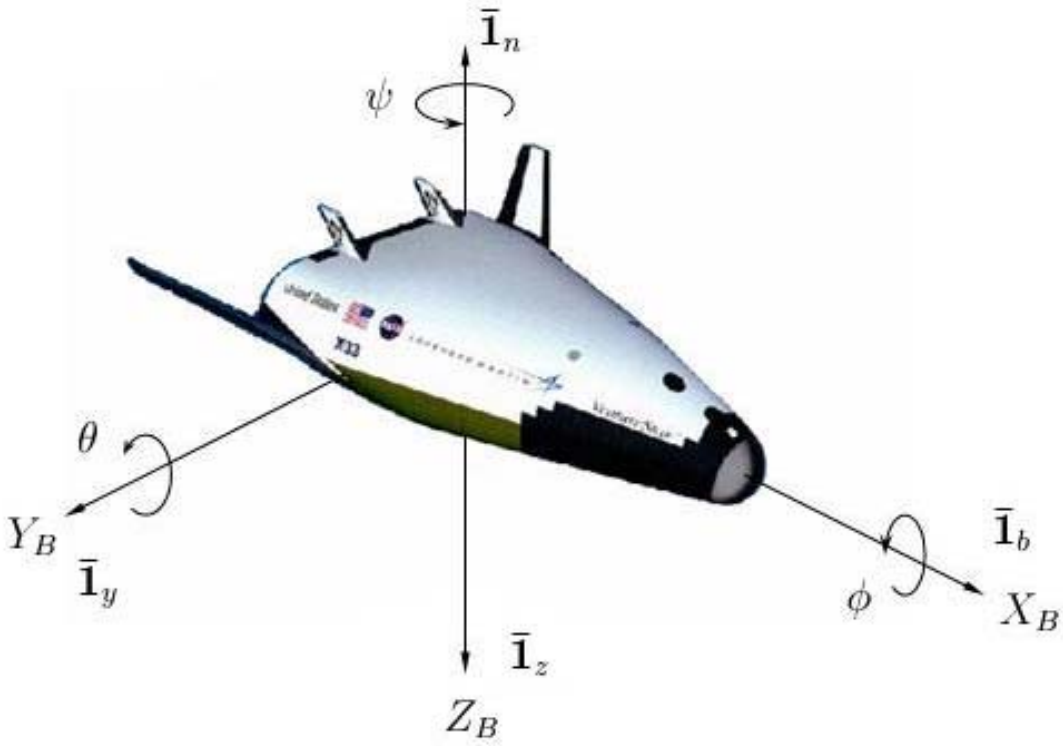
Figure 3: Vehicle body coordinate system showing Euler angles

3.4 Vehicle Body Coordinate System $X_B Y_B Z_B$

The vehicle body coordinate system is fixed to the vehicle as shown in Fig. 3. The x-axis X_B coincides with the vehicle body longitudinal axis. The z-axis Z_B lies in the plane of symmetry (or some reference plane in the case of asymmetric shapes), pointing "downward". The y-axis Y_B is perpendicular to these axes forming a right-handed coordinate system. Positive Y_B, thus points to the right when looking forward. The origin is generally taken at the vehicle center of gravity or at a fixed reference location relative to the geometry.

The Euler angles are also shown in Fig. 3. The yaw, pitch and roll angles are denoted by θ, ψ, and ϕ, respectively.

3.5 Coordinate Transformation

Let T_{EP} be the coordinate transformation matrix from ECI coordinate system to the plumbline frame.

$$T_{EP} = \begin{bmatrix} \cos\Theta\cos\Phi & \sin\Theta\cos\Phi & \sin\Phi \\ -\sin\Theta\cos A_z + \cos\Theta\sin\Phi\sin A_z & \cos\Theta\cos A_z + \sin\Theta\sin\Phi\sin A_z & -\cos\Phi\sin A_z \\ -\sin\Theta\sin A_z - \cos\Theta\sin\Phi\cos A_z & \cos\Theta\sin A_z - \sin\Theta\sin\Phi\cos A_z & \cos\Phi\cos A_z \end{bmatrix} \quad (3)$$

where Θ is the launch site longitude, Φ is the launch site geocentric latitude, and A_z is the launch azimuth (see Equation 1). Using T_{EP}, we can easily do the coordinate transformation from ECI system to plumbline frame, and vice versa. Using rotation sequence of pitch-yaw-roll (also referred to as 2-3-1 rotation), the coordinate transformation matrix T_{BP}, from body frame to plumbline frame is

$$T_{BP} = \begin{bmatrix} \cos\theta\cos\psi & \sin\theta\sin\phi - \cos\theta\sin\psi\cos\phi & \sin\theta\cos\phi + \cos\theta\sin\psi\sin\phi \\ \sin\psi & \cos\psi\cos\phi & -\cos\psi\sin\phi \\ -\sin\theta\cos\psi & \cos\theta\sin\phi + \sin\theta\sin\psi\cos\phi & \cos\theta\cos\phi - \sin\theta\sin\psi\sin\phi \end{bmatrix} \quad (4)$$

where θ, ψ, ϕ are the three Euler angles - pitch, yaw, and roll, respectively. The three columns of T_{BP}, are indeed the three unit vectors of the body axes $\mathbf{1}_b$, $\mathbf{1}_y$, $\mathbf{1}_z$ in plumbline frame. Therefore, the unit vector of the body x-axis is given by

$$\mathbf{1}_b = \begin{bmatrix} \cos\theta\cos\psi \\ \sin\psi \\ -\sin\theta\cos\psi \end{bmatrix} \quad (5)$$

The unit vector of the body y-axis in plumbline frame is defined as

$$\mathbf{1}_y = \begin{bmatrix} \sin\theta\sin\phi - \cos\theta\sin\psi\cos\phi \\ \cos\psi\cos\phi \\ \cos\theta\sin\phi + \sin\theta\sin\psi\cos\phi \end{bmatrix} \quad (6)$$

The body z-axis can be determined by imposing the right-hand rule

$$\mathbf{1}_z = \mathbf{1}_b \times \mathbf{1}_y = -\mathbf{1}_n \quad (7)$$

Once we find the three body axes in plumbline frame, the Euler angles could be easily calculated using the following relationship.

$$\theta = -\tan^{-1}\left(\frac{1_{bz}}{1_{bx}}\right)$$
$$\psi = \tan^{-1}\left(\frac{1_{by}}{1_{bx}\cos\theta - 1_{bz}\sin\theta}\right) \quad (8)$$
$$\phi = -\tan^{-1}\left(\frac{1_{zy}}{1_{yy}}\right)$$

where, 1_{bx}, 1_{by} and 1_{bz} are the three components of the unit vector $\mathbf{1}_b$. And 1_{yy}, 1_{zy}, are the y-components of unit vector $\mathbf{1}_y$ and $\mathbf{1}_z$ respectively.

4

Endo-Atmospheric Closed-Loop Ascent Guidance

4.1 Introduction

The ascent guidance system of a rocket-powered launch vehicle determines the attitude commands and, when applicable, engine throttle command during the ascent of the vehicle. It is well known that whether or not the ascent trajectory is optimal can have a significant impact on propellant usage for a given payload, or on payload weight for the same gross vehicle weight. Consequently ascent guidance commands are usually optimized in some fashion. In fact, ascent guidance is one of the most notable engineering fields where optimal control theory has found routine applications. Successful vacuum rocket guidance software based on the optimal control theory includes the Iterative Guidance Mode (IGM) for the Saturn rockets,[1] and the Powered Explicit Guidance (PEG) for the Space Shuttle.[2] These algorithms solve the optimal vacuum powered flight problem on-board in each guidance update cycle using the current condition as the initial condition of the solution. Therefore the guidance strategy in effect is closed-loop.

One of the major open challenges of ascent guidance lies in the endo-atmospheric portion of the flight. The presence of the aerodynamic forces, loads and winds significantly complicates the optimal ascent problem, making the solution process much more difficult to converge reliably and sufficiently fast for on-board applications. For these reasons typical current ascent guidance inside the atmosphere is open-loop.[3] In such an approach, the guidance commands are generated off-line, updated with the day-of-launch wind data prior to launch, and loaded into the launch vehicle for use during the ascent through the atmosphere. While very successful in nominal ascent guidance, the open-loop approach inherently lacks the adaptive capability to handle contingencies and aborts, even with extensive off-line planning at great costs. Open-loop guidance also does not possess the robustness necessary to cope with significant off-nominal conditions and system Modeling uncertainty, especially for new launch vehicles for which little or no flight data is available. The required re-planning and re-generation of the open-loop ascent guidance commands whenever any mission or system parameters change are costly in both developmental and operational phases of the

launch vehicle.

A closed-loop ascent guidance algorithm could address all of the above deficiencies of open-loop guidance. The search for a feasible algorithm to solve the optimal control problem on-board for closed-loop atmospheric ascent guidance dates back to the 1960s. The work by Brown and Johnson represents one of the earliest attempts in this direction.[4] In a series of recent work[5–7] that has stimulated renewed interest in this area, Calise *et al* develop a hybrid approach to the problem. In this approach the analytical solution of the optimal vacuum flight and numerical collocation for atmospheric portion are combined. The vacuum solution serves as the initial guess for the atmospheric flight, and a homotopy method is used to gradually phase in the aerodynamic terms and path constraint-related terms. References[8–11] contain further recent enhancements and more development in endo-atmospheric ascent guidance.

This part of the report describes the endo-atmospheric guidance algorithm used in this work.[12] The main components of this part of the report are:

- Comprehensive treatment to the 3-dimensional optimal ascent problem subject to the common path constraints and orbital insertion conditions, and techniques to address a number of on-board implementation issues, some of which are unique to non-axisymmetric launch vehicles (such as a lifting-entry reusable launch vehicle);

- Demonstration of the suitability for the solution of the ascent guidance problem by a classical finite-difference approach which can be interpreted as a special form of collocation, but is conceptually simpler and easier to implement;

- Illustration of the capability and feasibility of on-board closed-loop ascent guidance by a series of carefully designed tests.

4.2   Ascent Trajectory Dynamics

The equations of motion for a rocket-powered launch vehicle, in a central gravitational field, expressed in an inertial coordinate system are as follows:

$$\dot{\boldsymbol{r}} = \boldsymbol{V} \tag{1}$$

$$\dot{\boldsymbol{V}} = \boldsymbol{g}(\boldsymbol{r}) + \frac{T\boldsymbol{1}_b}{m(t)} + \frac{\boldsymbol{A}}{m(t)} + \frac{\boldsymbol{N}}{m(t)} \tag{2}$$

$$\dot{m} = -\frac{\eta T_{vac}}{g_0 I_{sp}} \tag{3}$$

where $\boldsymbol{r}$ and $\boldsymbol{V} \in R^3$ are the inertial position and velocity vectors; $\boldsymbol{g}$ the gravitational acceleration; T_{vac} the full vacuum thrust magnitude; $\eta > 0$ is the engine throttle; T the current thrust magnitude including effects of throttle modulation and thrust loss due to back pressure. In this formulation the total engine thrust is assumed to be aligned with the body longitudinal axis, and is not gimbaled independently. The vectors $\mathbf{A}$ and $\mathbf{N}$ are the

aerodynamic forces in the body longitudinal and normal direction, respectively; $\mathbf{1}_b$ the unit vector defining the launch vehicle body longitudinal axis; $m(t)$ is the mass of the launch vehicle at the current time t. The specific impulse of the engine is I_{sp} and g_0 represents the gravitational acceleration magnitude on the surface of the Earth.

4.3 Definition of Vehicle Body Axis Frame

The definition of vehicle body axis frame $x_b y_b z_b$ depends on how we want the vehicle to fly. We can choose to construct $\mathbf{1}_z$ (therefore the symmetric plane) so that the vehicle flies a zero degree ("heads-up") or 180 degree ("heads-down") bank angle trajectory.

$$\mathbf{1}_y = \frac{\mathbf{1}_b \times \mathbf{r}}{\|\mathbf{1}_b \times \mathbf{r}\|} \tag{4}$$

The Shuttle adopts this heads-down option. This heads-down position assists in communications with the ground and allows instruments within the cargo bay to be pointed back toward the Earth, which is required for many of the experiments carried within the bay. There is probably also some psychological benefit to the crew since they are given spectacular views of home rather than staring into the cold darkness of the great void of space.

We can also construct $\mathbf{1}_z$ so that the vehicle flies at zero sideslip angle.[13] The definition of vehicle body axis frame in this study follows this zero-sideslip formulation. In this formulation, the launch vehicle symmetric plane is assumed to be always the plane formed by the body-axis $\mathbf{1}_b$ and the Earth relative velocity vector $\mathbf{V}_r$. Thus the sideslip angle remains zero. Note that such a body-frame orientation necessitates a roll angle about the longitudinal axis $\mathbf{1}_b$ to null the sideslip in the presence of cross winds. Physically, this is the so-called "fly into the wind" maneuver as in the case of Space Shuttle ascent.

Thus the unit vector of the body x-axis is the same as $\mathbf{1}_b$; the unit vector of the body y-axis is defined as

$$\mathbf{1}_y = \frac{\mathbf{1}_{V_r} \times \mathbf{1}_b}{\|\mathbf{1}_{V_r} \times \mathbf{1}_b\|} \tag{5}$$

where, $\mathbf{1}_{V_r} = \mathbf{V}_r / V_r$ is the unit vector in the direction of $\mathbf{V}_r$. The unit vector of the body z-axis completes the right-hand system $\mathbf{1}_z = \mathbf{1}_b \times \mathbf{1}_y$. Denote the body-normal unit vector by $\mathbf{1}_n = -\mathbf{1}_z$. Then

$$\mathbf{1}_n = \mathbf{1}_b \times \frac{(\mathbf{1}_b \times \mathbf{V}_r)}{\|\mathbf{1}_b \times \mathbf{V}_r\|} \qquad (\ \alpha > 0\ ) \tag{6}$$

where, $\mathbf{V}_r = \mathbf{V} - \bar{\omega}_e \times \mathbf{r} =$ Earth relative velocity; $\bar{\omega}_e =$ Earth rotation vector in the plumbline launch frame. Note in this formulation, the sideslip $\beta \equiv 0$. Figure 4 shows this configuration. Clearly,

$$\cos \alpha = \mathbf{1}_b^T \mathbf{1}_{V_r} \quad or \quad |\sin \alpha| = \|\mathbf{1}_{V_r} \times \mathbf{1}_b\| \tag{7}$$

To avoid an instantaneous 180-degree rotation of $\mathbf{1}_n$, when α crosses $\alpha = 0$, $\mathbf{1}_n$ should be defined to be

$$\mathbf{1}_n = \mathbf{1}_b \times \frac{(\mathbf{V}_r \times \mathbf{1}_b)}{\|\mathbf{1}_b \times \mathbf{V}_r\|} \qquad (\ \alpha < 0\ ) \tag{8}$$

13
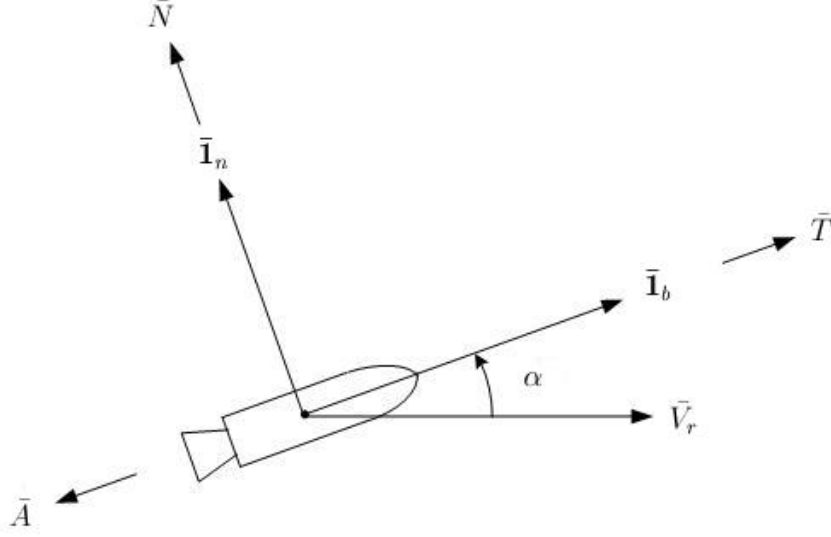
Figure 4: Launch vehicle body frame with relative velocity

The following expression for 1_y is preferred to Equation (5)

$$\mathbf{1}_y = \mathbf{1}_{V_r} \times \mathbf{1}_b / \sin \alpha \tag{9}$$

The reason is that this definition is valid for both $\alpha > 0$ and $\alpha < 0$ without causing the instantaneous 180-degree rotation in $\mathbf{1}_y$, when $\mathbf{1}_{V_r}$ and $\mathbf{1}_b$ cross over each other (α changes sign).

4.4 Nondimensionalization

For better numerical conditioning, the following nondimensionalization is used:

- The distances are normalized by R_0, the radius of the Earth at equator;

- Time is normalize by $\sqrt{R_0/g_0}$;

- The velocities are normalized by $\sqrt{R_0 g_0}$, the circular velocity around the Earth at R_0

The gravity is Modeled by the Newtonian central gravity field. With some abuse of notation, we use the same names hereafter for the dimensionless variables. Under the zero-sideslip formulation as shown in Fig. 4, the dimensionless equations of motion from Eqs (1) and (2) become

$$\begin{cases} \mathbf{r}' = \mathbf{V} \\ \mathbf{V}' = -\dfrac{1}{r^3}\mathbf{r} + (T - A)\mathbf{1}_b + N\mathbf{1}_n \end{cases} \tag{10}$$

14

where the differentiation is with respect to the dimensionless time. Now A and N are the aerodynamic accelerations in g_0 in the body longitudinal and normal direction respectively, and T the magnitude of the thrust acceleration in g_0. The magnitudes of the dimensionless aerodynamic and thrust accelerations are given by

$$A = \frac{R_0}{2m(t)}\rho(r)V_r^2 S_{ref} C_A(M_a, \alpha) \tag{11}$$

$$N = \frac{R_0}{2m(t)}\rho(r)V_r^2 S_{ref} C_N(M_a, \alpha) \tag{12}$$

$$T = [\eta T_{vac} + \Delta T(r)]/m(t)g_0 \tag{13}$$

where, $\rho(r)$ is the dimensional atmospheric density at radius r; V_r is the magnitude of the dimensionless Earth-relative velocity

$$\boldsymbol{V}_r = \boldsymbol{V} - \bar{\omega}_E \times \boldsymbol{r} - \boldsymbol{V}_w \tag{14}$$

where $\boldsymbol{V}_w$ is the wind velocity vector and $\bar{\omega}_E$ is the Earth angular rotation rate vector. The axial and normal aerodynamic coefficients C_A and C_N are functions of Mach number M_a and angle of attack α. They are expressed in analytical forms by curving-fitting the tabulated data. The thrust loss ΔT due to the back pressure is a function of altitude through the dependence of ΔT on ambient pressure. Note that the mass flow rate will be reduced by the same percentage as the thrust when the thrust is throttled down.

4.5 Guidance Problem and Constraints

The current conditions $\boldsymbol{r}_0$ and $\boldsymbol{V}_0$ are assumed to be known. The ascent guidance problem is to find the desired body-axis orientation $\boldsymbol{1}_b(t)$ at each instant which determines the thrust direction and aerodynamic forces during the atmospheric portion of the ascent. The engine throttle η will also need to be determined for enforcing some of the path constraints, as will be discussed later. The final conditions will be the engine-cutoff conditions which ensure insertion into the required orbit. These orbital insertion conditions can in general be written as k, $0 < k \leq 6$, algebraic end conditions

$$\Psi(\boldsymbol{r}(t_f), \boldsymbol{V}(t_f)) = 0, \quad \Psi \in R^k \tag{15}$$

Specifics on (15) will also be discussed later. In addition, there will be path constraints on the trajectory for safety and vehicle integrity. The three most common path constraints in ascent guidance will be considered: the product of dynamic pressure and α, axial thrust acceleration, and dynamic pressure

$$|q\alpha| \leq Q_\alpha \tag{16}$$

$$T \leq T_{max} \tag{17}$$

$$q \leq q_{max} \tag{18}$$

where $q = \rho V_r^2/2$. The constants Q_α, T_{max}, and q_{max} are the respective limits for each of the corresponding constraints. Another common path constraint on $|q\beta|$, the product of dynamic

pressure and sideslip angle, is not included here because in our zero-sideslip formulation, this quantity usually already has small magnitude. The constraints on normal acceleration $|N|$ and angle of attack α, if necessary, can be handled in the same way as constraint (16) is handled. Thus they will not be discussed separately. Collectively, the above path constraints may be written in a compact form

$$\boldsymbol{S}(\boldsymbol{r}, \boldsymbol{V}, \boldsymbol{1}_b, t) \leq 0 \tag{19}$$

4.6 Optimal Control Problem and Necessary Conditions

The mathematical tool used to find the optimal ascent guidance commands is the optimal control theory. In this setting a performance index is defined. The minimization of this performance index is usually tied in one way or the other to the minimization of propellant usage. Denote the performance index by

$$J = \phi(\boldsymbol{r}_f, \boldsymbol{V}_f, t_f) \tag{20}$$

where t_f is the engine cutoff time and $\boldsymbol{r}_f$ and $\boldsymbol{V}_f$ are the position and inertial velocity of the launch vehicle at t_f. The functional form of J is best selected to be most convenient for a particular formulation of the optimal ascent problem. Typical choices are $J = t_f$, for the minimum-time problem, or $J = 1/r_f - V_f^2$, for the maximum-energy problem with a fixed t_f.

Most recently it has been shown that in general no singular optimal thrust programs exist in atmospheric ascent.[8] Therefore the optimal throttle is bang-bang type. In this report the engine throttle η is treated as a given (possibly time-varying) input. Thus the variation of the mass $m(t)$ is considered a prescribed function of time, not a state. In order to focus on the presentation of the essentials of the approach, the path constraints Eqs. (16-18) will be added later. With these assumptions and noting the constraint $\boldsymbol{1}_b^T \boldsymbol{1}_b = 1$, we define the Hamiltonian

$$H = \boldsymbol{p}_r^T \boldsymbol{V} + \boldsymbol{p}_V^T \left[-\frac{1}{r^3} \boldsymbol{r} + (T - A) \boldsymbol{1}_b + N \boldsymbol{1}_n \right] + \mu(\boldsymbol{1}_b^T \boldsymbol{1}_b - 1) \tag{21}$$

where μ is a scalar multiplier, and $\boldsymbol{p}_r$ and $\boldsymbol{p}_V \in R^3$ are the so-called costate vectors. Let the asterisk signify the optimal values of the relevant variables. The standard necessary conditions for the optimal solution are[14] (using the notion of *Maximum Principle*)

$$\boldsymbol{p}_r' = -\frac{\partial H}{\partial \boldsymbol{r}} \tag{22}$$

$$\boldsymbol{p}_V' = -\frac{\partial H}{\partial \boldsymbol{V}} \tag{23}$$

$$H(\boldsymbol{p}_r, \boldsymbol{p}_V, \boldsymbol{r}^*, \boldsymbol{V}^*, \boldsymbol{1}_b^*, t) = \max_{\boldsymbol{1}_b} H(\boldsymbol{p}_r, \boldsymbol{p}_V, \boldsymbol{r}^*, \boldsymbol{V}^*, \boldsymbol{1}_b, t) \tag{24}$$

16

The derivation of the expressions of the costate equations (22-23) is quite involved. The detailed equations are provided in Appendix A. The optimal solution must also satisfy the terminal constraints (15) and the following transversality conditions

$$
\boldsymbol{p}_r(t_f) = -\frac{\partial \phi(\boldsymbol{r}_f, \boldsymbol{V}_f, t_f)}{\partial \boldsymbol{r}_f} + \left(\frac{\partial \Psi}{\partial \boldsymbol{r}_f}\right)^T \nu \tag{25}
$$

$$
\boldsymbol{p}_V(t_f) = -\frac{\partial \phi(\boldsymbol{r}_f, \boldsymbol{V}_f, t_f)}{\partial \boldsymbol{V}_f} + \left(\frac{\partial \Psi}{\partial \boldsymbol{V}_f}\right)^T \nu \tag{26}
$$

$$
H(\boldsymbol{p}_r, \boldsymbol{p}_V, \boldsymbol{r}^*, \boldsymbol{V}^*, \boldsymbol{1}_b^*, t)|_{t_f} = \frac{\partial \phi}{\partial t_f} \tag{27}
$$

where $\nu \in R^k$ is a constant multiplier vector. The last condition (27) is for the cases where the final time t_f is not specified. The first two conditions (25-26) can be combined to eliminate the unknown vector ν and yield $6 - k$ independent conditions involving only final costate $\boldsymbol{p}_f = (\boldsymbol{p}_{r_f}^T \ \boldsymbol{p}_{V_f}^T)^T$ and final state $\boldsymbol{x}_f = (\boldsymbol{r}_f^T \ \boldsymbol{V}_f^T)^T$. The general approach will be first finding the $6 - k$ linear independent solutions of the homogeneous system

$$
\left(\frac{\partial \Psi}{\partial \boldsymbol{x}_f}\right) \xi = 0
$$

Let $\xi_i(\boldsymbol{x}_f) \in R^6$, $i = 1, ..., 6 - k$ be such solutions. Note that ξ_i's are functions of $\boldsymbol{x}_f$. Transversality conditions (25) and (26) are then equivalent to

$$
\left(\boldsymbol{p}_f + \frac{\partial \phi}{\partial \boldsymbol{x}_f}\right)^T \xi_i \triangleq \Gamma_i(\boldsymbol{p}_f, \boldsymbol{x}_f) = 0, \ i = 1, \ldots, 6 - k. \tag{28}
$$

The k terminal constraints (15) plus the above $6 - k$ conditions constitute the 6 terminal conditions for the optimal control problem. For a given problem, the conditions in (28) can often times be obtained more conveniently by using the terminal constraints (15) and taking dot products of Eqs. (25) and (26) with appropriate vectors related to the final state $\boldsymbol{x}_f$. Examples will be given later.

The optimality condition (24) necessitates

$$
\frac{\partial H}{\partial \boldsymbol{1}_b} = 0 \tag{29}
$$

Define $s = \|\boldsymbol{1}_b \times \boldsymbol{1}_{V_r}\|$. The expansion of the optimality condition $\partial H / \partial \boldsymbol{1}_b = 0$ requires, among other relationships, the following

$$
\frac{\partial \alpha}{\boldsymbol{1}_b} = \frac{\cos \alpha}{\sin \alpha} \boldsymbol{1}_b - \frac{1}{\sin \alpha} \boldsymbol{1}_{V_r} \tag{30}
$$

$$
\frac{\partial \boldsymbol{1}_n}{\partial \boldsymbol{1}_b} = \frac{1}{s} \left\{ (\boldsymbol{1}_{V_r}^T \boldsymbol{1}_b) I_3 + \boldsymbol{1}_b \boldsymbol{1}_{V_r}^T + \frac{1}{s^2} \left[(\boldsymbol{1}_{V_r}^T \boldsymbol{1}_b) \boldsymbol{1}_b - \boldsymbol{1}_{V_r} \right] \left[(\boldsymbol{1}_{V_r}^T \boldsymbol{1}_b) \boldsymbol{1}_{V_r} - \boldsymbol{1}_b \right]^T \right\} \tag{31}
$$

where I_3 is a 3×3 identity matrix. Let

$$
a = p_V[(\boldsymbol{1}_{V_r}^T \boldsymbol{1}_b)(\boldsymbol{1}_{p_V}^T \boldsymbol{1}_b) - (\boldsymbol{1}_{V_r}^T \boldsymbol{1}_{p_V})]/s
$$

$$
b = -p_V A_\alpha + a N_\alpha
$$

17

where $\mathbf{1}_{p_V} = \boldsymbol{p}_V / p_V$, $A_\alpha = \partial A / \partial \alpha$ and $N_\alpha = \partial N / \partial \alpha$. When evaluating $\partial H / \partial \mathbf{1}_b$, keep in mind that both A and N are functions of α, therefore functions of $\mathbf{1}_b$. Carrying out the differentiations and collecting terms, we eventually have

$$
\begin{aligned}
\mathbf{1}_b^* &= \frac{1}{(2\mu + b/\tan\alpha - aN/s^2)} \Big\{ -\big[T - A + N(\mathbf{1}_{V_r}^T \mathbf{1}_b^*)/s\big] \boldsymbol{p}_V \\
&\quad + \big[b/\sin\alpha - Np_V(\mathbf{1}_{p_V}^T \mathbf{1}_b^*)/s - aN(\mathbf{1}_{V_r}^T \mathbf{1}_b^*)/s^2\big] \mathbf{1}_{V_r} \Big\} \\
&\triangleq c_1(\boldsymbol{x},\boldsymbol{p},\mathbf{1}_b^*)\boldsymbol{p}_V + c_2(\boldsymbol{x},\boldsymbol{p},\mathbf{1}_b^*)\boldsymbol{V}_r
\end{aligned}
\tag{32}
$$

where c_1 and c_2 are scalar functions of the state, costate, and $\mathbf{1}_b^*$. Hence we conclude that the optimal body-axis lies in the plane formed by the primer vector $\boldsymbol{p}_V$ and relative velocity vector $\boldsymbol{V}_r$. A similar conclusion is reached by using a geometric approach in an earlier work by Vinh,[15] where the thrust direction and aerodynamic force vector are assumed to be independent controls.

The condition (32) suggests that the search for the optimal body-axis orientation can be reduced to a one-dimensional search in the plane of $\boldsymbol{p}_V$ and $\boldsymbol{V}_r$.[7] Let Φ be the angle between the vectors $\boldsymbol{p}_V$ and $\boldsymbol{V}_r$. At each instant with given state and costate, Φ is known. Denote by $\mathbf{1}_{p_r}$ and $\mathbf{1}_{p_V}$ the unit vectors in the directions of $\boldsymbol{p}_r$ and $\boldsymbol{p}_V$, respectively. Notice that $\mathbf{1}_b^T \mathbf{1}_{p_V} = \cos(\Phi - \alpha)$ and $\mathbf{1}_n^T \mathbf{1}_{p_V} = \sin(\Phi - \alpha)$. Using these two relationships in the expression of H in Eq. (21), it is clear that maximizing H with respect to $\mathbf{1}_b$ is equivalent to $\partial H / \partial \alpha = 0$, which in turn results in[7]

$$
\tan(\Phi - \alpha)(T - A + N_\alpha) - (A_\alpha + N) = 0
\tag{33}
$$

Since A, N, A_α and N_α are generally functions of α, the above equation needs to be solved numerically for α.

The cases for canted or gimbaled thrust vector are not included in above formulation. But the same conclusion can be reached in a similar fashion as in above analysis. This result is an extension of the well-known primer vector theory on optimal rocket flight in vacuum.[31]

Once α is found from Eq. (33), c_1 and c_2 in Eq. (32) can be solved in terms of α and Φ by taking the dot product of (32) with $\mathbf{1}_{p_V}$ and with $\mathbf{1}_{V_r}$

$$
\mathbf{1}_b^* = \left(\frac{\sin\alpha}{\sin\Phi}\right)\mathbf{1}_{p_V} + \left[\frac{\sin(\Phi - \alpha)}{\sin\Phi}\right]\mathbf{1}_{V_r}
\tag{34}
$$

Note that as the atmospheric density decreases (approaching vacuum flight), the aerodynamic terms diminish, and $\alpha \to \Phi$ from Eq. (33) . The optimal body axis in (34) and therefore the optimal thrust vector become aligned with the primer vector $\boldsymbol{p}_V$.[31]

4.7   Adding the Path Constraints

When inequality constraints (19) are added to the problem, the costate equations (22-23) will have additional terms related to the constraints, and the condition to determine the

controls will change. We shall discuss each of the three constraints in Eqs. (16-18) in the following.

Constraint $S_1 = q\alpha - Q_\alpha \leq 0$

Without loss of generality the absolute sign in Eq. (16) is removed for the simplicity of discussion. This constraint is a zeroth order constraint in that the control $\mathbf{1}_b$ appears explicitly (through α) in the constraint itself. In such a case, the costate equations take the form of

$$\mathbf{p}' = -\frac{\partial H}{\partial \mathbf{x}} - \lambda_{q\alpha}\frac{\partial S_1}{\partial \mathbf{x}} \tag{35}$$

where the multiplier $\lambda_{q\alpha} = 0$ and the problem is the same as in the preceding sections when $S_1 < 0$. When $S_1 = 0$, $\lambda_{q\alpha}$ satisfies the condition

$$\frac{\partial H}{\partial \mathbf{1}_b} + \lambda_{q\alpha}\frac{\partial S_1}{\partial \mathbf{1}_b} = 0 \tag{36}$$

Using condition (30) we have

$$\frac{\partial S_1}{\partial \mathbf{1}_b} = q\frac{\partial \alpha}{\mathbf{1}_b} = q\left(\frac{\cos\alpha}{\sin\alpha}\mathbf{1}_b - \frac{1}{\sin\alpha}\mathbf{1}_{V_r}\right) \tag{37}$$

Using condition (36) and the result in Eq. (37) and following the steps similar to those in Section 3.6, we can show that the optimal body axis $\mathbf{1}_b^*$ is again in the plane of $\mathbf{p}_V$ and $\mathbf{V}_r$ as before. Note that this conclusion cannot be assumed to be always true for any inequality constraints, and must be verified for each case. In this case condition (36) is equivalent to

$$\frac{\partial H}{\partial \alpha} + \lambda_{q\alpha}\frac{\partial S_1}{\partial \alpha} = 0 \tag{38}$$

Or,

$$\lambda_{q\alpha} = -\frac{\partial H/\partial \alpha}{q} \tag{39}$$

where

$$\frac{\partial H}{\partial \alpha} = p_V[(T - A + N_\alpha)\sin(\Phi - \alpha) - (A_\alpha + N)\cos(\Phi - \alpha)] \tag{40}$$

In a finite interval where $S_1 = 0$, the angle of attack is directly obtained from

$$\alpha = Q_\alpha/q \tag{41}$$

The direction of the body axis $\mathbf{1}_b$ is determined by α in the plane of $\mathbf{p}_V$ and $\mathbf{V}_r$ by Eq. (34) as before. The multiplier $\lambda_{q\alpha}$ is calculated from Eq. (39) and used in the costate equation (16) to propagate the costate.

Constraint $S_2 = T - T_{max} \leq 0$

Typically for the usual values of T_{max}, this constraint only becomes active after the trajectory is outside the dense atmosphere where $\Delta T(r) \approx 0$. Thus whether or not and

19

when this constraint will become active are uniquely determined by the prescribed engine throttle, not influenced by any of the trajectory state variables and the control $\mathbf{1}_b$. In this sense it is not a state or control constraint (recall that the engine throttle is regarded as a prescribed input). Once $S_2 = 0$, the engine throttle will be adjusted according to

$$\eta = \frac{T_{max}m(t)g_0}{T_{vac}} \tag{42}$$

to keep $S_2=0$. The costate equations are the same as in (22-23), and the optimal body axis $\mathbf{1}_b^*$ is found in Eq. (34) as before.

Constraint $S_3 = q - q_{max} \leq 0$

This is a first-order constraint because the control $\mathbf{1}_b$ appears in the first-order derivative of S_3. Recall that $q = \rho(r)V_r^2/2$, and $\mathbf{V}_r$ is defined in Eq. (14). So

$$S_3' = \frac{1}{2r}\rho_r V_r^2 \mathbf{r}^T \mathbf{V} + \rho \mathbf{V}_r^T \mathbf{V}_r' \tag{43}$$

where $\rho_r = \partial\rho/\partial r$ and

$$\mathbf{V}_r' = \mathbf{V}' - \bar{\omega}_E \times \mathbf{V} - \mathbf{V}_w' \tag{44}$$

Suppose that $S_3 = 0$ in a finite interval $[t_1, \ t_2]$. The costate equations in this interval are

$$\mathbf{p}' = -\frac{\partial H}{\partial \mathbf{x}} - \lambda_q \frac{\partial S_3'}{\partial \mathbf{x}} \tag{45}$$

The corresponding optimality condition is

$$\frac{\partial H}{\partial \mathbf{1}_b} + \lambda_q \frac{\partial S_3'}{\partial \mathbf{1}_b} = 0 \tag{46}$$

The costate will have a jump at t_1

$$\mathbf{p}(t_1^+) = \mathbf{p}(t_1^-) + \kappa \frac{\partial S_3}{\partial \mathbf{x}} \tag{47}$$

where κ is a constant multiplier. It can be shown that

$$\frac{\partial S_3'}{\partial \mathbf{1}_b} = d_1(\mathbf{x}, \mathbf{1}_b)\mathbf{V}_r + d_2(\mathbf{x}, \mathbf{1}_b)\mathbf{1}_b \tag{48}$$

where d_1 and d_2 are two scalar functions. Therefore using the derivations in Section 3.6, we can show that condition (46) still results in that the optimal body axis $\mathbf{1}_b^*$ lies in the plane of $\mathbf{p}_V$ and $\mathbf{V}_r$. Conditions similar to Eqs. (38) and (39) can now be readily derived. And the condition $S_3' = 0$ provides the equation for the solution of α in $[t_1, t_2]$.

With the above equations laid out, the optimal solution in principle can be found numerically. But two implementation issues arise: 1) the engine throttle is known to be more effective in regulating the dynamic pressure by slowing down the increase of the velocity; 2) the jump condition Eq. (47) makes it necessary to accurately estimate the time t_1 in the

solution process for it to converge quickly. The second issue may not be a problem if only nominal ascent is considered, because a good estimate of t_1 can be obtained off-line if the vehicle modeling, day-of-launch wind data, and mission parameters are well known. But a chief potential advantage of closed-loop ascent guidance is for autonomous abort guidance. In aborts, the conditions are inevitably well off nominal, and any off-line estimates of t_1 could be no better than an arbitrary guess.

In an on-board environment, the entire ascent trajectory $\boldsymbol{x}(\cdot)$, along with the control $\mathbf{1}_b(\cdot)$ and throttle $\eta(\cdot)$, is generated from the current condition $\boldsymbol{x}(t)$ to the target condition in each guidance cycle. The current attitude commands and throttle command are from $\mathbf{1}_b(t)$ and $\eta(t)$, the first data point in the guidance solution. To address the above issues and keep the algorithms reasonably simple and robust for on-board guidance purposes, we adopt the following approach: The optimal body-axes in the guidance solution are still determined as in Sections 3.5 with the prescribed throttle where no constraint on the dynamics pressure is considered. This is justified because we conclude that the optimal body axis remains in the plane of $\boldsymbol{p}_V$ and $\boldsymbol{V}_r$ even when $q \leq q_{max}$ is active. Next, we consider the first-order derivative of q at t that can obtained as

$$q'(t) = a_q(\boldsymbol{x}, \mathbf{1}_b)\eta(t) + b_q(\boldsymbol{x}, \mathbf{1}_b) \tag{49}$$

where η is the current engine throttle, and the expressions for a_q and b_q are readily available when one makes the substitutions. Let $\delta > 0$ be a time-increment. A first-order approximation of $q(t + \delta)$ is

$$q(t + \delta) \approx q(t) + q'(t)\delta = q(t) + [a_q(\boldsymbol{x}, \mathbf{1}_b)\eta(t) + b_q(\boldsymbol{x}, \mathbf{1}_b)]\delta \tag{50}$$

When deciding the throttle command at the current time t, we require that $q(t + \delta) \leq q_{max}$. Using the above approximation for $q(t + \delta)$ in this condition, we have

$$\eta(t) \leq \frac{q_{max} - q(t) - b_q\delta}{a_q\delta} \triangleq \eta_q \tag{51}$$

Most likely η will have a minimum allowable setting $\eta_{min} > 0$ during engine-on period. Let $\eta_{prb} > \eta_{min}$ be the otherwise prescribed throttle setting (e.g., η_{max}). The current engine throttle command is determined by

$$\eta = \begin{cases} \eta_{prb}, & \text{if } \eta_q > \eta_{prb} \\ \eta_q, & \text{if } \eta_{min} \leq \eta_q \leq \eta_{prb} \\ \eta_{min}, & \text{if } \eta_q < \eta_{min} \end{cases} \tag{52}$$

The last case in (52) would be when the dynamic pressure constraint cannot be met by lowering the engine throttle within the allowable range, which is an unlikely event.

Remarks:

1. Since a first-order expansion (50) is used in deriving (51), one may be tempted to suspect that the enforcement of $q \leq q_{max}$ by this approach is acceptable only when δ is small. On the contrary, it can be shown that as long as the trajectory begins in

the region where $q < q_{max}$, the throttle given by (52) *guarantees strict satisfaction of the constraint $q \leq q_{max}$ for any $\delta > 0$.* It turns out that when $q \rightarrow q_{max}$, $\eta = \eta_q$ drives $q' \rightarrow 0$ for any $\delta > 0$, and whenever $q = q_{max}$, $q' = 0$. A detailed discussion of strict enforcement of first-order constraints by this type of technique can be found in a previous work on constrained nonlinear control systems.[16]

2. Because of the above property, an appropriate value δ can always be chosen for a given vehicle to eliminate the undesirable jitters in throttle command when the dynamic pressure constraint is active, and still accurately enforce the constraint. Typically there is a minimum value of δ above which a δ will render the engine throttle commands from (52) to be sufficiently smooth.

3. The benefits of this approach for enforcing the constraint $q \leq q_{max}$ are its simplicity, robustness, and effectiveness. And there is no need for the estimate of the instant t_1 when the constraint becomes active. It is closed-loop in nature, unlike the open-loop "throttle bucket" approach currently in use for the Shuttle. It should be pointed out, however, that the adjustment of the throttle is done outside the solution process of the optimal control problem. Thus the guidance solution in the period when the dynamic pressure constraint is active is not strictly optimal in theory (although the body axis is still determined according to the necessary conditions of the optimal control problem). But this period is always relatively short compared to the total burn time. The impact of this short deviation from the theoretical optimal conditions on performance appears to be negligible. We have used two different state-of-the-art trajectory optimization software packages[17,18] to cross-check the performance of the trajectories obtained herein. The differences in terms of propellant consumption have been minimal (See numerical results later). A similar observation is also made by Corvin[19] on the effects of adjusting throttle to control dynamic pressure.

5

Numerical Method

5.1 Finite Difference Approach

Finite difference is one of several classical techniques used for two-point-boundary-value problems (TPBVPs).[20] For ascent guidance applications, we have found that this classical approach is well suited for the problem.

After substituting the control $\mathbf{1}_b$ of Eq. (34) in the equations of motion and costate equations, and denoting $\boldsymbol{y} = (\boldsymbol{x}^T \ \boldsymbol{p}^T)^T \in R^{2n}$ with $n = 6$, the complete TPBVP is now

$$\boldsymbol{y}' = \boldsymbol{f}(t, \boldsymbol{y}) \tag{1}$$

$$\boldsymbol{B}_0(\boldsymbol{y}_0) = 0 \tag{2}$$

$$\boldsymbol{B}_f(\boldsymbol{y}_f) = 0 \tag{3}$$

where $\boldsymbol{B}_0 = \boldsymbol{x}(t_0) - \boldsymbol{x}_0$ in our problem represents the given initial condition , and $\boldsymbol{B}_f(\boldsymbol{y}_f) = 0$ are the 6 final conditions from combining the orbital insertion conditions Eq. (15) and the transversality conditions (28). Let t_f be the specified final time. The TPBVP is to find a solution $\boldsymbol{y}(t)$ that satisfies the differential equations (1) and boundary conditions (2-3). To find the solution, divide the time interval $t_f - t_0$ into M subintervals of the same length $h = (t_f - t_0)/M$. Let $\boldsymbol{y}_k = \boldsymbol{y}(t_0 + kh)$ be the value of the solution at the node $t_k = t_0 + kh$, $k = 0, \ldots, M$. At the middle point between t_{k-1} and t_k, denoted by $t_{k-1/2} = t_k - h/2$, the differential equations (1) are approximated by central finite difference:

$$\frac{1}{h}(\boldsymbol{y}_k - \boldsymbol{y}_{k-1}) = \boldsymbol{f}\left(t_{k-1/2}, \frac{\boldsymbol{y}_k - \boldsymbol{y}_{k-1}}{2}\right) \tag{4}$$

Or equivalently, $\boldsymbol{y}_k$ and $\boldsymbol{y}_{k-1}$ are constrained by the equation

$$\boldsymbol{E}_k(\boldsymbol{y}_k, \boldsymbol{y}_{k-1}) \triangleq \boldsymbol{y}_k - \boldsymbol{y}_{k-1} - h\boldsymbol{f}\left(t_{k-1/2}, \frac{\boldsymbol{y}_k - \boldsymbol{y}_{k-1}}{2}\right) = 0, k = 1, \ldots, M - 1. \tag{5}$$

In addition, the boundary conditions are denoted by

$$\boldsymbol{E}_0(\boldsymbol{y}_0) = \boldsymbol{B}_0(\boldsymbol{y}_0) = 0 \tag{6}$$

$$\boldsymbol{E}_M(\boldsymbol{y}_M) = \boldsymbol{B}_f(\boldsymbol{y}_f) = 0 \tag{7}$$

Treat $\boldsymbol{Y} = (\boldsymbol{y}_0^T \ \boldsymbol{y}_1^T \ldots \boldsymbol{y}_M^T)^T \in R^{2n(M+1)}$ as the unknowns. The same number of equations are

$$\boldsymbol{E}(\boldsymbol{Y}) = 0 \tag{8}$$

where $\boldsymbol{E} = (\boldsymbol{E}_0^T \ \boldsymbol{E}_1^T \ldots \boldsymbol{E}_M^T)^T$. Now the problem becomes a root-finding problem for a system of $2n(M+1)$ nonlinear algebraic equations (8). It has been rigorously established that under certain conditions on smoothness and the boundary conditions, the following holds true[20]

1. Each of the original TPBVP and the finite difference problem has a unique solution;

2. The solution of the above finite difference problem $\boldsymbol{y}_k$ is a second-order approximation to the solution of the TPBVP $\boldsymbol{y}^*(t)$ at each t_k, i.e.,

$$\|\boldsymbol{y}^*(t_k) - \boldsymbol{y}_k\| = \mathcal{O}(h^2), \ \ k = 1, 2, \ldots, M \tag{9}$$

where $\lim_{h \to 0} \mathcal{O}(h^2)/h^2 < \infty$.

For ascent guidance applications, since the time-to-go $t_f - t_0$ is decreasing, the accuracy of the finite difference solution will be higher and higher as h becomes smaller even for a small to moderate number of nodes.

For problems with free final time t_f, see Section 5.1 for a treatment.

5.2 Modified Newton Algorithm

A modified Newton method[21] is chosen as the algorithm for solving the problem (8) for its balance between complexity and effectiveness. Starting from an initial guess $\boldsymbol{Y}_0$ (which may be reliably and quickly generated from vacuum solution using the algorithm to be described in Section 6), the search direction $\boldsymbol{d}_j$ in the j-th iteration is determined by solving the linear algebraic equations

$$\left[\frac{\partial \boldsymbol{E}(\boldsymbol{Y}_{j-1})}{\partial \boldsymbol{Y}} \right] \boldsymbol{d}_j = -\boldsymbol{E}(\boldsymbol{Y}_{j-1}), \ j = 1, 2, \ldots \tag{10}$$

Next, determine the step size parameter σ_j by the following criterion

$$\sigma_j = \max_{0 \le i} \left\{ \frac{1}{2^i} \ \Big| \ \boldsymbol{E}^T(\boldsymbol{Y}_{j-1} + \frac{1}{2^i}\boldsymbol{d}_j)\boldsymbol{E}(\boldsymbol{Y}_{j-1} + \frac{1}{2^i}\boldsymbol{d}_j) < \boldsymbol{E}^T(Y_{j-1})\boldsymbol{E}(Y_{j-1}) \right\} \tag{11}$$

In other words, starting from $\sigma_j = 1$, σ_j is halved repeatedly if necessary until the above condition is satisfied. Then the update is given by

$$\boldsymbol{Y}_j = \boldsymbol{Y}_{j-1} + \sigma_j\boldsymbol{d}_j, \quad 0 < \sigma_j \le 1, \tag{12}$$

This choice of the search step size ensures that the sequence $\{\|\boldsymbol{E}(\boldsymbol{Y}_j)\|\}$ is monotonically decreasing. Convergence is achieved when $\|\boldsymbol{E}(\boldsymbol{Y}_j)\|$ is no greater than a preselected tolerance. The possible additional function evaluations required in checking the above step size condition pose negligible computational burden because function evaluations are not expensive in this setting. The result on the other hand is a much more robust algorithm, especially

when the initial guesses are not close to the final solution. The step size selection (11) is a deciding factor for the success of the finite difference approach in solving the optimal ascent problem.

The evaluation of the Jacobian $\partial \boldsymbol{E}/\partial \boldsymbol{Y}$ can certainly be done analytically. But we believe that simple numerical finite differencing is more advantageous in this case. This is because again unlike in the cases where integrations of differential equations are involved for each function evaluation, the function evaluations here are purely algebraic and fast. Using analytical Jacobian offers no clear computational speed benefits. In our comparison study we have seen that the numerical Jacobians and analytical Jacobians match between the 6th to 8th digit. With the scalings described in this report, this type of precision appears to be more than adequate for convergence to occur. On the other hand, analytical Jacobian will make the computer code significantly more complicated because second-order partial derivatives of the right hand sides of the state equations are needed. Also, when some of the path constraints in Eq. (19) become active, the associated Lagrange multipliers such as the one in Eq. (39) will be functions of state and costate, adding more complexity to the analytical Jacobian. When the launch vehicle design is evolving in the developmental stage, or if the same ascent guidance code is desired to be applied to different launch vehicle configurations, fewer labor-intensive changes to the code would be required with numerical differencing. One exception is for the gradients of the boundary conditions in (7). The gradients for these conditions are evaluated analytically because they are readily available.

At first glance, solving the linear system (10) may seem to be a formidable task in an on-board environment because of the dimension of the problem $(2n(M+1))$ which can easily be over 1000. However, a closer inspection reveals that the Jacobian matrix in (10) has a special sparse pattern due to the dependence of $\boldsymbol{E}_k$ on only $\boldsymbol{y}_k$ and $\boldsymbol{y}_{k-1}$ (cf. Eq. (5)). Therefore a very efficient algorithm, both in speed and storage, based on Gauss eliminations and sequential back substitutions can be devised to solve the system (10). More details in this regard is discussed in the next section.

5.3   Gaussian Elimination and Back Substitution

Expand the algebraic system (8) in first-order Taylor series with respect to small changes $\Delta \boldsymbol{Y}_k$ at the current iterate $\boldsymbol{Y}_k$. At an interior point, $k = 1, 2, ..., M$, this gives

$$\boldsymbol{E}_k(\boldsymbol{Y}_k + \Delta \boldsymbol{Y}_k, \boldsymbol{Y}_{k-1} + \Delta \boldsymbol{Y}_{k-1}) \approx \boldsymbol{E}_k(\boldsymbol{Y}_k, \boldsymbol{Y}_{k-1}) + \frac{\partial \boldsymbol{E}_k}{\partial \boldsymbol{Y}_{k-1}} \Delta \boldsymbol{Y}_{k-1} + \frac{\partial \boldsymbol{E}_k}{\partial \boldsymbol{Y}_k} \Delta \boldsymbol{Y}_k \quad (13)$$

For a solution we want the updated value $\boldsymbol{E}(\boldsymbol{Y} + \Delta \boldsymbol{Y})$ to be zero, so the general set of equations at an interior point can be written as

$$\frac{\partial \boldsymbol{E}_k}{\partial \boldsymbol{Y}_{k-1}} \Delta \boldsymbol{Y}_{k-1} + \frac{\partial \boldsymbol{E}_k}{\partial \boldsymbol{Y}_k} \Delta \boldsymbol{Y}_k = -\boldsymbol{E}_k(\boldsymbol{Y}_k, \boldsymbol{Y}_{k-1}) \quad (14)$$

Similarly, the boundary conditions can be expanded in a first-order Taylor series for increments that improve the solution.

$$\frac{\partial \boldsymbol{E}_0}{\partial \boldsymbol{Y}_0} \Delta \boldsymbol{Y}_0 = -\boldsymbol{E}_0(\boldsymbol{Y}_0) \tag{15}$$

$$\frac{\partial \boldsymbol{E}_M}{\partial \boldsymbol{Y}_M} \Delta \boldsymbol{Y}_M = -\boldsymbol{E}_M(\boldsymbol{Y}_M) \tag{16}$$

We thus have in Eqs (14)-(16) a set of algebraic linear equations to be solved for the corrections $\Delta \boldsymbol{Y}_k$, iterating until the corrections are sufficiently small. The equations have a special structure, because the Jacobians involve only points k and $k-1$. Figure 5 illustrates a typical matrix structure of the complete algebraic equations for the case of 8 variables (two-dimensional ascent problem, $n = 4$) and 4 mesh points, with 4 boundary conditions imposed at each of the endpoints. In the figure, "x" represents a coefficient of the FDEs, "v" represents a component of the unknown solution vector, , "B" is a component of the known right-hand side, and empty spaces represent zeros.
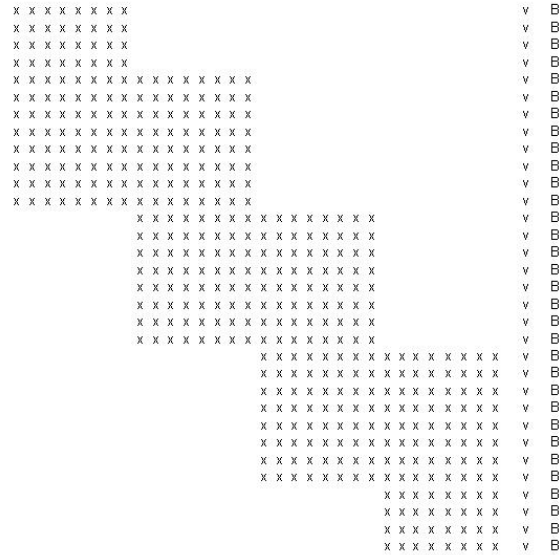
Figure 5: Matrix structure of FDEs with boundary conditions

Because of the special "block diagonal" structure of the matrix, a special form of Gaussian elimination, which can minimize storage requirement of matrix coefficients by packing the elements in a special blocked structure, can be applied to solve the problem.[22] General Gaussian elimination manipulates the algebraic linear equations by elementary operations, such as dividing rows of coefficients by a common factor to produce unity in diagonal elements, and adding appropriate multiples of other rows to produce zeros below the diagonal. In this special Gaussian elimination, we take advantage of the block structure by performing a bit more reduction than in pure Gaussian elimination, so that the storage of coefficients is minimized. Only a small subset of the $2n(M+1) \times 2n(M+1)$ matrix elements needs to be stored as the elimination progresses. Once the matrix elements reach the stage in Fig. 6, the solution can follow quickly by a back substitution procedure.

```
1        x x x x                                          v   B
  1      x x x x                                          v   B
    1    x x x x                                          v   B
      1 x x x x                                           v   B
        1        x x x x                                  v   B
          1      x x x x                                  v   B
            1    x x x x                                  v   B
              1  x x x x                                  v   B
                1 x x x x                                 v   B
                  1 x x x x                               v   B
                    1 x x x x                             v   B
                      1 x x x x                           v   B
                        1        x x x x                  v   B
                          1      x x x x                  v   B
                            1    x x x x                  v   B
                              1  x x x x                  v   B
                                1 x x x x                 v   B
                                  1 x x x x               v   B
                                    1 x x x x             v   B
                                      1 x x x x           v   B
                                        1        x x x x  v   B
                                          1      x x x x  v   B
                                            1    x x x x  v   B
                                              1  x x x x  v   B
                                                1 x x x x v   B
                                                  1 x x x x v  B
                                                    1 x x x x  v  B
                                                      1 x x x x v  B
                                                        1        v   B
                                                          1      v   B
                                                            1    v   B
                                                              1  v   B
```
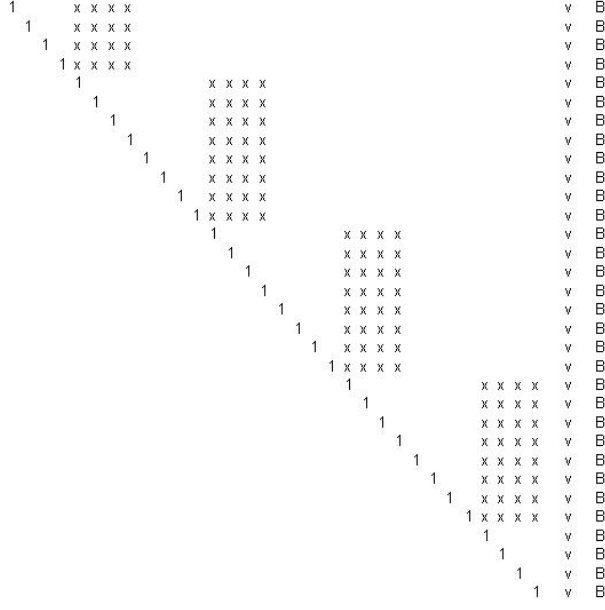
Figure 6: Target structure of the Gaussian elimination

The entire procedure except the back substitution step, operates only on one block of the matrix at a time. The procedure contains 4 types of operations:

- partial reduction to zero of certain elements of a block using results from a previous step;

- elimination of the square structure of the remaining block elements such that the square section contains unity along the diagonal, and zero in off-diagonal elements;

- storage of the remaining nonzero coefficients for use in later steps;

- back substitution.

For more detail, please refer to Reference 22.

Once the correction $\Delta \boldsymbol{Y}$ is solved from the algebraic linear equations, we update the solution by

$$\boldsymbol{Y}_j = \boldsymbol{Y}_{j-1} + \sigma_j \Delta \boldsymbol{Y}_j \tag{17}$$

Where, the subscript "j" denotes the j-th iteration. The step size parameter σ_j is determined by the following criterion

$$\sigma_j = \max_{0 \le i} \left\{ \frac{1}{2^i} \,\middle|\, \boldsymbol{E}^T(\boldsymbol{Y}_{j-1} + \frac{\Delta \boldsymbol{Y}_j}{2^i})\boldsymbol{E}(\boldsymbol{Y}_{j-1} + \frac{\Delta \boldsymbol{Y}_j}{2^i}) < \boldsymbol{E}^T(\boldsymbol{Y}_{j-1})\boldsymbol{E}(\boldsymbol{Y}_{j-1}) \right\} \tag{18}$$

27

Starting from $\sigma_j = 1$, σ_j is halved repeatedly if necessary, till the above condition is satisfied. This choice of the step size ensures that the sequence $\{\|\boldsymbol{E}(\boldsymbol{Y}_j)\|\}$ is monotonically decreasing. Convergence is achieved when $\|\boldsymbol{E}(\boldsymbol{Y}_j)\|$ is no greater than a preselected tolerance. This step size selection in Eq. (18) is a deciding factor for the success of the finite difference approach in solving the optimal ascent problem. The possible additional function evaluations required in checking the step size condition pose negligible computational burden since function evaluations are not expensive in this setting. The result on the other hand is a much more robust algorithm, especially when the initial guess is not close to the final solution.

5.4 Continuation on Atmospheric Density

It is well known in ascent trajectory optimization that the strong coupling of the aerodynamic forces with the orientation of the body-axis and the inequality path constraints make the convergence of any algorithm from a completely "cold" initial start difficult to achieve. That is the reason why homotopic filters,[6] sometimes up to 4 levels of homotopy,[7] are used to gradually distort the solution from the vacuum solution to the final solution. A similar approach is taken here, except that the finite difference approach described in the preceding section appears to need only one level of homotopy. The form of the continuation used here is simpler and is only on the atmospheric density

$$\hat{\rho} = \varepsilon\rho, \quad 0 \leq \varepsilon \leq 1 \tag{19}$$

For each fixed ε, $\hat{\rho}$ is used in place of the atmospheric density everywhere ρ appears in the state-, costate-equations, and path constraints. Note that all the development in this part of the report, although aimed at atmospheric ascent, applies without any modifications to vacuum flight when $\rho = 0$. The homotopic parameter ε is initiated at 0 for the vacuum solution, and gradually increased to unity for full atmospheric solution. The converged solution for the current value of ε serves as the starting point for the solution with the next value of ε till $\varepsilon = 1$. We have been using an increment of 0.1 on ε, which seems to be adequate in our cases. In on-board applications, no continuation is usually necessary when the solution in the previous guidance cycle is used as the starting point (that, $\varepsilon = 1$).

For the vacuum solution, in many cases linear interpolations between the initial values and targeted final values of the state and constant guesses for $\boldsymbol{p}(t)$ suffice to be an initial guess $\boldsymbol{Y}_0$ that will lead to convergence. An analytical method to generate optimal vacuum ascent trajectories is presented in Appendix B. This method is based on a succinct summary by Calise *et al*[6] of a number of elegant results on optimal vacuum guidance developed in the last 3 decades. Some modifications have been made in the version in Appendix B. With this type of algorithm, an optimal vacuum solution can be found very quickly and reliably. This solution can in turn be used as the starting solution in the above continuation process.

6

Verification, Validation and Testing

A number of test cases are presented in this section. The purpose is to demonstrate the working of the endo-atmospheric algorithm developed above. More extensive testing results are contained in Part IV of this report. All the cases use the vehicle parameters, mass property, propulsion system Modeling, and aerodynamic Modeling of the X-33 vehicle. The X-33 is a single-stage suborbital vehicle with a lifting-body configuration (see Fig. 3). To make the vehicle orbit-capable, the specific impulse is doubled in the simulations. All the missions are launched from the Kennedy Space Center (KSC). The open-loop solutions obtained using the method described in this report are compared with those obtained by using other methods. Closed-loop simulations are performed to assess the feasibility of on-board ascent guidance with the approach proposed in this report. Unless stated otherwise, all the vectors are expressed in the inertial launch plumbline coordinate system introduced in Section 2.2.

6.1   Terminal Conditions and Final Time Adjustment

The finite difference approach described in Section 4.1 is most convenient for fixed final-time problems. Similar to what is done in Ref. [7], the optimal ascent problem is solved as a series of fixed final-time problems to maximize the orbital energy, i.e., to minimize

$$J = \frac{1}{r_f} - \frac{V_f^2}{2} \tag{1}$$

The final time is adjusted sequentially until the optimal value of J is equal to the specified (negative) orbital energy.

Four-Constraint Problem

The orbital insertion conditions are given by the radius r_f^*, velocity V_f^*, orbital inclination i^*, and flight path angle γ_f^*. Note that γ_f^* need not necessarily be zero in this case. These conditions are equivalent to specified semi-major axis, eccentricity, orbital inclination, and true anomaly at insertion point. Let $\mathbf{1}_N$ be a unit vector parallel to the polar axis of the Earth and pointing to the North. For each fixed t_f the 3 orbital insertion conditions (15) in

this case can be expressed as

$$\frac{1}{2}\mathbf{r}_f^T\mathbf{r}_f - \frac{1}{2}r_f^{*2} = 0 \tag{2}$$

$$\mathbf{1}_N^T(\mathbf{r}_f \times \mathbf{V}_f) - \|\mathbf{r}_f \times \mathbf{V}_f\| \cos i^* = 0 \tag{3}$$

$$\mathbf{r}_f^T\mathbf{V}_f - r_f V_f \sin \gamma_f^* = 0 \tag{4}$$

For simplicity, we replace r_f in (1) with r_f^*. Taking dot products of the transversality condition Eq. (25) with $\mathbf{r}_f$, Eq. (26) with $\mathbf{r}_f$, Eq. (25) with $\mathbf{V}_f$, and both Eqs. (25) and (26) with $\mathbf{h}_f = \mathbf{r}_f \times \mathbf{V}_f$, we can eliminate the multiplier vector ν and obtain

$$(\mathbf{V}_f^T\mathbf{p}_{r_f})r_f^2 - (\mathbf{r}_f^T\mathbf{p}_{V_f})V_f^2 + (\mathbf{r}_f^T\mathbf{V}_f)(V_f^2 - \mathbf{r}_f^T\mathbf{p}_{r_f}) = 0 \tag{5}$$

$$\mathbf{V}_f^T\mathbf{p}_{V_f} - V_f^2 = 0 \tag{6}$$

$$(\mathbf{h}_f^T\mathbf{p}_{r_f})[\mathbf{h}_f^T(\mathbf{r}_f \times \mathbf{1}_N)] + (\mathbf{h}_f^T\mathbf{p}_{V_f})[\mathbf{h}_f^T(\mathbf{V}_f \times \mathbf{1}_N)] = 0 \tag{7}$$

The above 6 equations (2-7) constitute the terminal boundary conditions (3) for this case.

To adjust the final time, we have found that the secant method works very well for this purpose. Let $t_f^{(k-1)}$ and $t_f^{(k)}$ be two consecutive estimates of t_f used to solve the above problem, and $J^{(k)}$ and $J^{(k-1)}$ be the values of J when $t_f^{(k)}$ and $t^{(k-1)}$ are used to solve the optimal ascent problem. Then the next choice of t_f is given by

$$t_f^{(k+1)} = t_f^{(k)} - \left(\frac{t_f^{(k)} - t_f^{(k-1)}}{J^{(k)} - J^{(k-1)}}\right)(J^{(k)} - J^*), \ k = 1, 2, ... \tag{8}$$

The correct t_f is found when $|J^{(k)} - J^*|$ is within a preset tolerance, and the final velocity V_f will be within a small neighborhood of V_f^*. To use the secant search (8), two starting values of $t_f^{(0)}$ and $t_f^{(1)}$ are needed. For on-board guidance, the converged value of t_f in the previous guidance cycle is the logical choice of $t_f^{(0)}$. Since the guidance solution in the current cycle will be very close to the previous one, the variational relationship of $\delta J = H(t_f)\delta t_f$ in optimal control problems can be used to generate $t_f^{(1)}$

$$t_f^{(1)} = t_f^{(0)} + \frac{J^{(0)} - J^*}{H(t_f^{(0)})} \tag{9}$$

where $H(t_f^{(0)})$ is the final value of the Hamiltonian. It is possible to simply use (9) to search for all $t_f^{(k)}$, $k \geq 1$, as in Refs. [7-8]. But we have found the secant method (8) to be much more robust and efficient than the exclusive use of Eq. (9).

Five-Constraint Problem

The orbital insertion conditions are given by the radius r_f^*, velocity V_f^*, orbital inclination i^*, flight path angle $\gamma_f^* = 0$ (insertion at perigee/apogee, or into a circular orbit), and longitude of ascending node Ω^*. A mission to rendezvous with an orbiting spacecraft would call for the 5th constraint on Ω^*. With i^* and Ω^* specified, the direction of the angular

momentum vector of the orbit is fixed, given in an Earth centered inertial (ECI) system by the unit vector $\mathbf{1}_h^{ECI} = (\sin \Omega^* \sin i^*, \ -\cos \Omega^* \sin i^*, \ \cos i^*)^T$. Let $\mathbf{1}_h$ be the representation of $\mathbf{1}_h^{ECI}$ in the inertial launch plumbline system. The 4 orbital insertion conditions for a fixed final time are

$$\frac{1}{2}\boldsymbol{r}_f^T\boldsymbol{r}_f - \frac{1}{2}r_f^{*2} \ = \ 0 \tag{10}$$

$$\boldsymbol{r}_f^T\boldsymbol{V}_f \ = \ 0 \tag{11}$$

$$\boldsymbol{r}_f^T\mathbf{1}_h \ = \ 0 \tag{12}$$

$$\boldsymbol{V}_f^T\mathbf{1}_h \ = \ 0 \tag{13}$$

By taking dot products of the transversality condition Eq. (25) with $\boldsymbol{V}_f$, Eq. (26) with $\boldsymbol{V}_f$, then with $\boldsymbol{r}_f$, and making use of the above conditions, we again eliminate the multiplier vector ν and obtain

$$(\boldsymbol{V}_f^T\boldsymbol{p}_{r_f})r_f^2 - (\boldsymbol{r}_f^T\boldsymbol{p}_{V_f})V_f^2 \ = \ 0 \tag{14}$$

$$\boldsymbol{V}_f^T\boldsymbol{p}_{V_f} - V_f^2 \ = \ 0 \tag{15}$$

The final time t_f is adjusted the same way by Eq. (8) so that $V_f = V_f^*$.

For staged launch vehicles where all the stages except for the last one burn to the depletion of the fuel, the burn time of each stage is known for given throttle. The approach in this report is still applicable with minor modifications. Note that the break points in the finite difference discretization do not have to be equally spaced. In the case of a N-stage vehicle, N different values for the step parameter h may be selected, each for a stage, such that the staging times are located exactly at the last nodes of the stages. The changes of mass and thrust due to staging can then be accommodated easily. The burn time of the last stage is adjusted to meet the final velocity condition.

A number of other orbital insertion conditions were also examined and implemented. But the principle is the same, thus we will not repeat them in this report.

6.2   Open-loop Solutions

The open-loop solutions are generated using the finite-difference (FD) method. For verification and validation of the approach, the trajectories are compared to the ones obtained with other established trajectory optimization tools. The wind velocity $\boldsymbol{V}_w$ is set to be zero in the solutions. The target orbit is a circular orbit at the altitude of 185.2 km (100 nm). Two orbital inclinations are used: $i^* = 51.6$ deg (the orbital inclination of the International Space Station), and $i^* = 28.5$ deg (the minimum orbital inclination from KSC). A third case is the same circular orbit with $i^* = 51.6$ deg and $\Omega^* = -104$ deg (a 5-constraint problem). The initial conditions correspond to those after 5 seconds of vertical ascent (to clear the tower)

with a given launch mass of the X-33. The following path constraints are imposed

$$|q\alpha| \leq 626.74 \text{ N-rad/m}^2 \text{ (750 psf-deg)} \tag{16}$$
$$T \leq 4.0 \ (g) \tag{17}$$

The engine throttle is set at unity before the thrust acceleration constraint is active. The constraint on dynamic pressure will be added later in closed-loop simulations using the technique presented in Section 3.7. In the following results, 100 nodes were used in FD solutions. For comparison, the solutions for the same missions were also obtained by a collocation software, *Sparse Optimal Control Software* (SOCS),[17] and by a trajectory optimization software based on a pseudo-spectral method, *Direct and Indirect Dynamic Optimization (DIDO)*.[18] The SOCS solutions had the same 100 nodes, and the DIDO solutions had 20 nodes. The performance index for both SOCS and DIDO was the final time.

Table 1 summarizes the flight times t_f and final mass m_f of the solutions. The results for all the missions under different methods are very close. The slight differences among the solutions were mostly due to the discretization errors of the different schemes used in the 3 methods. This comparison clearly supports the validity of the FD approach. The difference, however, is in computation time. Depending on initial guesses, SOCS and DIDO could use tens of minutes to find the solution, whereas the FD method takes only a small fraction of one second to find the solution.

Figure 7 shows the 3-D ascent trajectories and ground tracks for the cases of $i^* = 51.6$ deg and $\Omega = -104$ deg in the inertial launch plumbline coordinate frame. As expected, the trajectory with ascending node constraint had larger out-of-plane motion. Figure 8 depicts the angle of attack, pitch angle and yaw angle along all the 3 trajectories by the FD approach. The constraint on the ascending node usually is one that requires larger yaw and roll maneuvers and thus is a demanding constraint. Indeed larger yaw angle is observed in Fig. 8 for that case. The variations of $q\alpha$ and axial thrust acceleration are plotted in Fig. 9 Both path constraints were accurately enforced.

6.3   Closed-loop Simulations

In closed-loop simulations, the point-mass vehicle dynamics, atmospheric Modeling, propulsive and aerodynamic forces, and winds were simulated by a FORTRAN program. The FD algorithm, which is also implemented in FORTRAN, was called once every second to recalculate the optimal solution based on the current condition. The trajectory simulations used the first data in the optimal body-axes attitude and engine throttle solutions (corresponding to current time) as the guidance commands. No delays or actuator dynamics were simulated. The missions and initial conditions were the same as in the open-loop solutions. In addition to path constraints (16) and (17), a dynamic pressure constraint is also imposed

$$q \leq 18194.4 \text{ N/m}^2 \text{ (380 psf)} \tag{18}$$

Closed-loop Simulations without Winds

The previous 3 missions were repeated in closed-loop simulations with the wind velocity $\boldsymbol{V}_w$ set to be zero. The dynamic pressure constraint was handled using the technique described in this report. Thirty nodes were used in the FD guidance solution. For on-board guidance, fewer nodes can be used than in an open-loop solution because the time-to-go is decreasing, thus the accuracy of the solution is increasing while the computation demands would not be unnecessarily high. A converged solution was loaded before "launch" as the starting point. On a desktop computer with a 1 GHz processor, the CPU time that each guidance solution call took ranged from 0.07 to 0.25 second, without any optimization or streamlining of the code. All the orbital insertion conditions were met accurately (See Table 3 in the following). Table 2 lists the flight times and final masses for all the 3 missions. Also in the table are open-loop solutions by SOCS with the addition of the dynamic pressure constraint (18). In all 3 cases the closed-loop guided trajectories and the SOCS open-loop solutions have differences in the final mass of about 120 kg or less. These small discrepancies are largely attributed to the differences between closed-loop simulations and open-loop trajectories.

Figure 10 shows the altitude versus inertial velocity along the three trajectories. The variations of dynamic pressure, throttle, and axial thrust acceleration are plotted in Fig. 11. The effectiveness of the feedback approach described in Section 3.7 for enforcing the dynamic pressure constraint is clearly seen: the dynamic pressure constraint (18) is accurately met in all cases and the feedback throttle modulations are smooth. This is much similar to the "throttle bucket" the Shuttle employs for the same purpose, except that the Shuttle throttle bucket is pre-programmed (open loop) prior to launch. In comparison, the SOCS solutions all have considerable zigzags in the throttle when the constraint (18) is active (not shown in the figure). From Table 2, the performance (in terms of final mass) of the closed-loop trajectory with the feedback adjustment of the throttle is apparently about the same as that of the open-loop optimal solution. The variations of $q\alpha$ and α are in Fig. 12. Figure 13 contains the histories of pitch, yaw and roll angles along the 3 trajectories. As expected, the mission with ascending node constraint called for more yaw and roll maneuvers than the other two missions.

Closed-loop Simulations with Winds

So far in the simulations the wind velocity has been assumed to be zero. To test the ascent guidance algorithm in a more realistic setting, winds were added in the simulations. The wind profiles were based on the measured wind velocities at different altitudes at KSC, and then smoothed for guidance purposes. In each simulated trajectory, the same smoothed wind profile was used in both the guidance solution and simulation of the launch vehicle dynamics. We realize that the actual wind the launch vehicle experiences will likely be different from the measured wind because of the time delay between the launch and the time when the measurement was taken. But the purpose here is to demonstrate how the ascent guidance algorithm would perform in the presence of winds should perfect wind information be available. We have also tested the cases when the wind profiles used in guidance algorithm were correlated but not exactly the same as the wind profiles in simulations. In those cases the enforcement of path constraints is affected by how well the measured wind profiles match the actual wind profiles. With the volatile winds, some of which are quite strong (up to 75

33

m/s), the limit of $q\alpha$ needs to be higher in order to fly through the winds. Thus the constraint (16) is changed to

$$|q\alpha| \leq 1671.32 \text{ N-rad/m}^2 \text{ (2000 psf-deg)} \qquad (19)$$

Ten trajectories were simulated for each of the above three missions, with a different wind profile applied in each trajectory. Unlike open-loop ascent guidance, no "pre-launch" adjustments or updates were required for the guidance algorithm for each simulation. The only update for each flight was the wind profile. The closed-loop ascent guidance algorithm automatically incorporates the wind data in the guidance solution. The starting point was still the same zero-wind solution used before. The CPU time for each guidance cycle did not differ from the previously recorded value by any noticeable margin.

The simulation results are summarized in Table 3. The first 6 quantities with Δ are the orbital insertion condition errors. The minimum, average, and maximum values of these errors among the 10 trajectories for each mission are listed. The altitude errors were all within 0.2 meter and velocity errors within 0.4 m/s. The quantity Δa is the error in semi-major axis of the final orbit, which is a parameter combining the effects of Δr_f and ΔV_f. The maximum of Δa was no greater than 0.6 km. All other errors were very small as well. The peak values of $|q\alpha|$ were essentially all within the specified range. The product of $q\beta$, where β is the sideslip angle, was not listed for it remained practically zero because of the roll maneuvers by the launch vehicle to "fly into the wind". Even when the wind profiles used in simulations were different from but correlated to the wind profiles used in the guidance solution, such as in actual launch, the peak values of $|q\beta|$ in general were still significantly smaller than those of $|q\alpha|$ (not shown here). The average final masses for all the 3 missions were quite close to those in Table 2 for the trajectories without winds. It should be mentioned that whether or not the wind data is included in the optimal guidance solutions can make a sizable difference in the performance. If the wind profiles are merely used outside the guidance solution to limit the attitude guidance commands for observing the $q\alpha$-constraint, the results using the X-33 vehicle Model can mean up to 500 kg less payload delivered into the same orbit.

Table 1: Open-loop performance comparison

Mission	FD		SOCS		DIDO	
	t_f (sec)	m_f (kg)	t_f (sec)	m_f (kg)	t_f (sec)	m_f (kg)
$i = 51.6°$	320.48	38627.5	321.00	38476.2	321.12	38471.8
$i = 28.5°$	317.73	39135.7	318.05	39011.0	318.18	39007.2
$\Omega = $ -104°	322.71	38220.1	322.33	38236.5	322.81	38166.9

Table 2: Closed-loop simulations **without** winds

Mission	FD		SOCS (open-loop)	
	t_f (sec)	m_f (kg)	t_f (sec)	m_f (kg)
$i = 51.6°$	326.57	38182.4	323.23	38293.6
$i = 28.5°$	323.59	38706.7	320.24	38828.6
$\Omega = $ -104°	327.33	38023.9	324.5	38054.6

Table 3: Closed-loop simulations **with** winds (10 wind profiles for each mission)

	$i = 51.6°$			$i = 28.5°$			$\Omega = -104°$		
	Min	**Mean**	**Max**	**Min**	**Mean**	**Max**	**Min**	**Mean**	**Max**
Δr_f (m)	-0.0165	0.0128	0.107	-0.0115	0.0152	0.112	-0.0145	0.0484	0.117
ΔV_f (m/s)	0.1531	0.2290	0.3007	0.1625	0.2352	0.3327	0.1583	0.1909	0.25388
Δa (km)	0.2581	0.3856	0.5063	0.2735	0.3961	0.5602	0.2665	0.3215	0.4275
Δi (deg)	2.4E-5	4.6E-5	5.9E-5	-1.9E-06	-4.2E-07	5.7E-07	-5.8E-4	-2.4E-4	7.9E-05
$\Delta \Omega$ (deg)	N/A	N/A	N/A	N/A	N/A	N/A	-7.2E-4	-2.9E-4	9.8E-05
$\Delta \gamma$ (deg)	-3.3E-4	1.2E-4	1.7E-3	-2.6E-4	1.3E-4	1.5E-3	-3.0E-4	6.4E-4	1.7E-3
max $|q\alpha|*$	919.4	1268.3	1608.3	694.2	1157.8	1641.8	1085.3	1255.8	1690.3
m_f (kg)	38010.4	38131.1	38238.5	38507.2	38626.3	38785.4	37789.4	37948.9	38065.3
t_f (sec)	326.51	328.66	331.21	322.68	326.77	329.51	327.29	329.66	333.19

* unit in N-rad/m^2

inclination = 516.deg
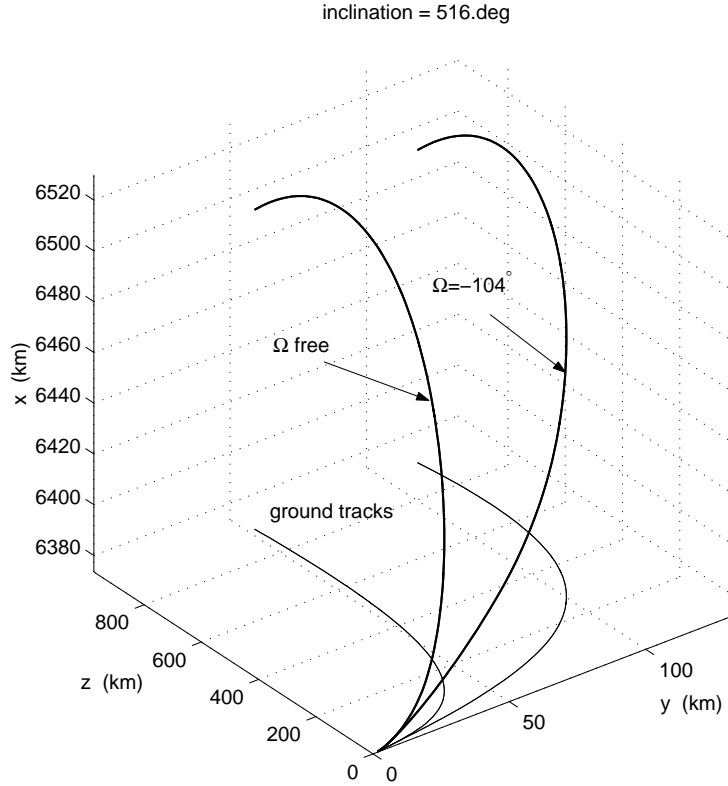
Figure 7: Three-dimensional ascent trajectories in launch plumbline system
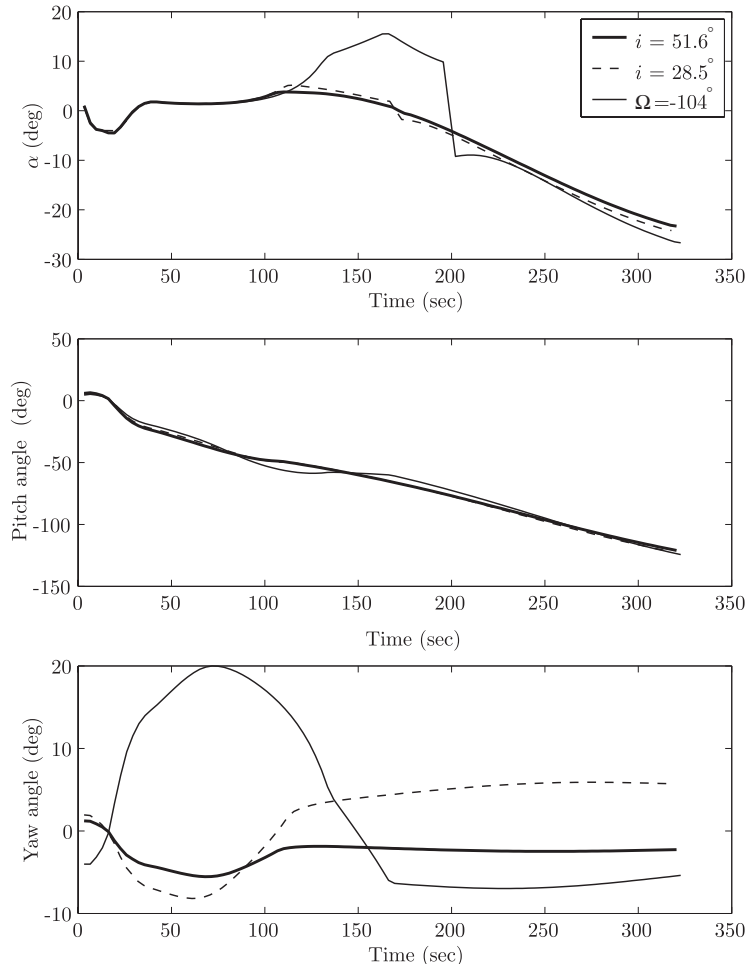
Figure 8: Angle of attack, pitch and yaw angles in open-loop solutions
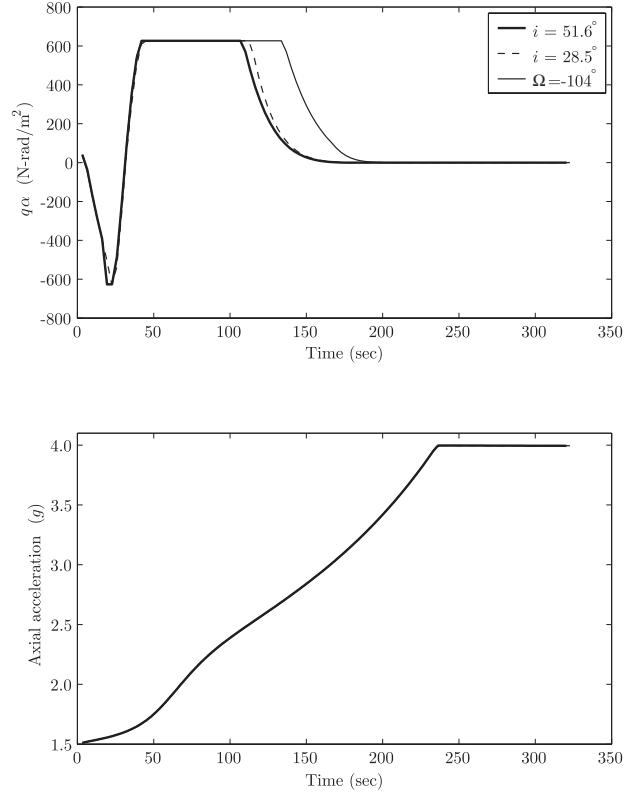
Figure 9: Variations of $q\alpha$ and axial thrust acceleration in open-loop solutions
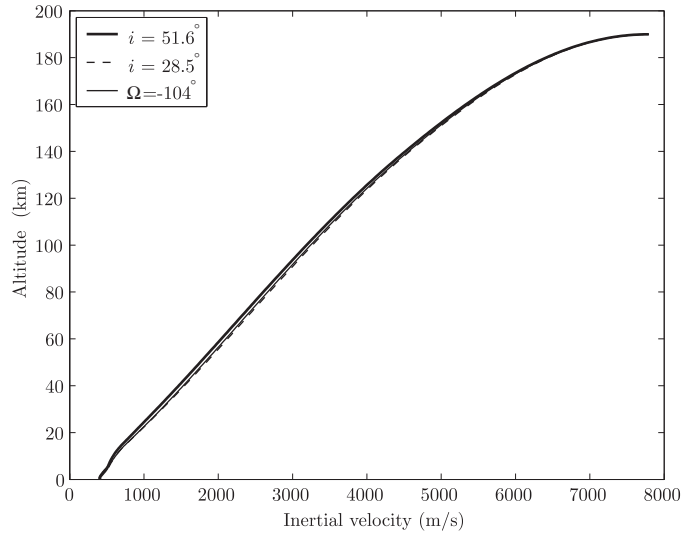
Figure 10: Altitude versus inertial velocity along closed-loop trajectories
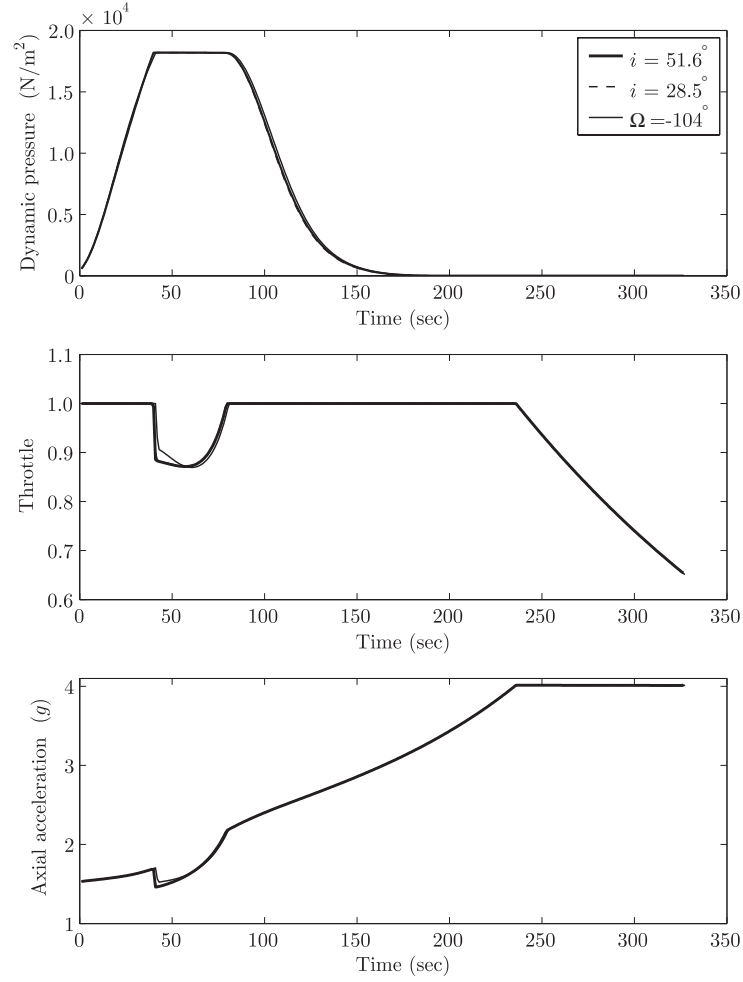
Figure 11: Dynamic pressure, throttle and axial acceleration along closed-loop trajectories
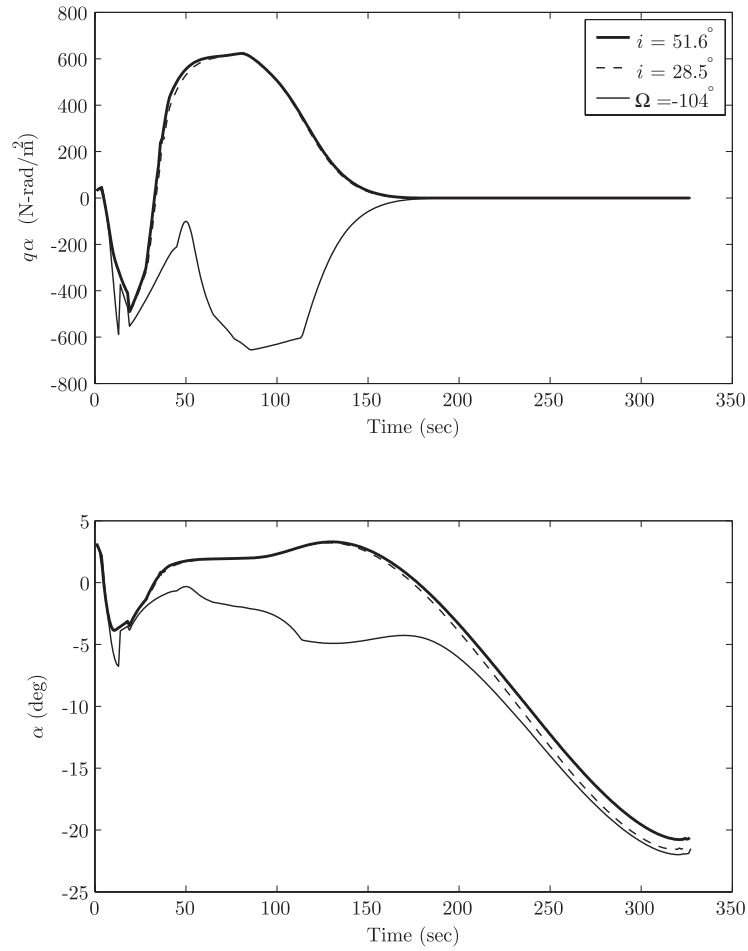
Figure 12: Variations of $q\alpha$ and α along closed-loop trajectories (no winds)
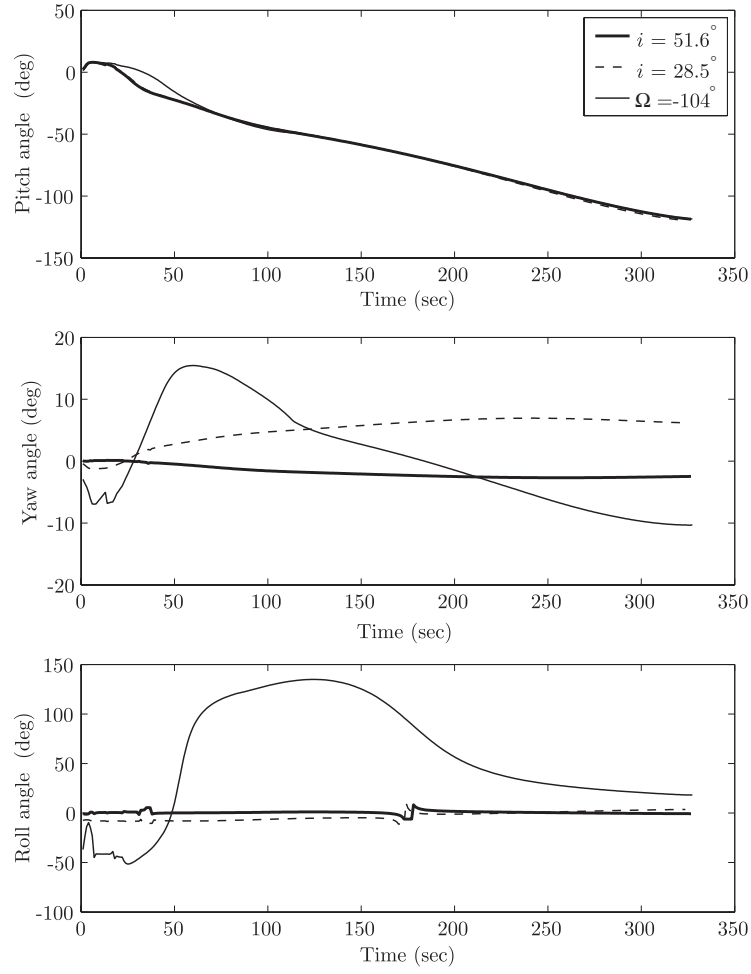
Figure 13: Variations of Euler angles along closed-loop trajectories (no winds)

7

Exo-Atmospheric Closed-Loop Ascent Guidance

7.1 Introduction

Launch ascent mission planning and guidance is an engineering area where routine applications of optimization tools and optimal control theory are a necessity rather than nicety. Indeed, on-board algorithms for solving the optimal ascent problem are the foundation of closed-loop ascent guidance for upper stages of launch vehicles since the 1960s. The examples of classical exo-atmospheric optimal ascent guidance algorithms include the Iterative Guidance Mode (IGM) guidance employed for the Saturn V rockets[1] and the Powered Explicit Guidance (PEG) for the Space Shuttle.[2] When the optimal ascent problem is solved on-line repeatedly with the current condition as the initial condition, the guidance solution is in effect closed loop.

For multiple-stage launch vehicles, it is well known that allowing a coast arc of optimal duration between two upper stages can reduce propellant consumption (or increase orbital insertion mass), in some cases quite appreciably. In other scenarios a long coast is necessary between two burns, such as insertion into high-altitude orbits, or orbital transfers. However, there are additional challenges resulting from the presence of coast arcs and multiple burns. Multiple burns and coast arcs typically render the optimal control problem much more sensitive and increase the difficulty in achieving convergence of the algorithm. This heightened sensitivity is largely due to two reasons: (a) long coast arcs tend to amplify any variations in the condition at the beginning of the coast; (b) the final stage/burn usually has a much smaller thrust acceleration, and it would be incapable of making large flight path corrections (indeed, the last burn in many orbital insertion cases is almost tangential, mainly responsible for pushing the velocity to the required value). The fact that even today, missions with multiple-burns and coast arcs are planned and executed by the ground control is probably attributable in no small part to these challenges. The recent on-going efforts in striving to achieve the capabilities of responsive space launch mission planning and operations and autonomous space operations have brought renewed strong interest in this subject.

To overcome the aforementioned difficulties, researchers have continued to seek more

robust and reliable methods to handle the optimal ascent problem with multiple burns and coast arcs. References[6,10,11,23–26] represent only a small sampling of the literature. With the exception of the work by Dukeman,[10,11] most existing work treats the problem essentially in a single-shoot formulation, i.e., the missing initial costate is iterated on to satisfy the terminal constraints and transversality conditions. References[10] and[11] employ a numerical multiple-shooting approach to the problem including the endo-atmospheric ascent portion.

In this report we present an analytical multiple-shooting method for exo-atmospheric multi-burn optimal ascent. The overarching theme in this effort is to strive for enhanced robustness and reliability of the algorithm. In this approach the optimal trajectory is treated in segments of burn and coast arcs. The costate in each segment is expressed in closed-form solution and the state in analytical solution involving thrust quadratures. Such a multiple-shooting formulation reduces the sensitivity of the problem with respect to the parameters to be found, especially beneficial to the cases with long coast arcs. The orbital insertion conditions, transversality conditions, and matching continuity conditions at the break points constitute a system of nonlinear algebraic equations with an analytical Jacobian. For numerical solutions, the existing work almost invariably uses the classical or some modified version of the Newton method. Here we adopt the highly-regarded Powell's dog-leg method[28] for improved robustness and reliability of the overall algorithm in more difficult and even possibly singular cases (where the optimal coast time reduces to zero). Another major component of this report is a detailed analysis of the class of optimal ascent problems under discussion. This analysis reveals several properties previously unknown to the community, to the best of our knowledge. The results allow us to resolve satisfactorily a numerical scaling mismatch issue in the optimal ascent problem that could otherwise severely hinder convergence reliability of the algorithm. All these measures contribute to a robust and fast algorithm for optimal multi-burn ascent planning and closed-loop guidance. The algorithm is verified with an industry standard software, Optimal Trajectories by Implicit Simulation (OTIS).[29]

7.2 Multi-Stage Optimal Ascent Problem with Coast

Instead of seeking maximum generality, we choose tacitly to present the development in a burn-coast-burn pattern for readability of the presentation. There is no methodological difficulty to extend the development here to any combinations of other numbers of burn and coast arcs. Borrowing the Shuttle terminology, we will refer the burnout of the first vacuum burn/stage as Main Engine Cut-Off (MECO), and the second burn/stage after a coast as the Orbital Maneuver System (OMS) burn. For on-orbit maneuvers it is understood that both burns can be made by the same engine, and there is no staging at the end of the first burn.

7.3 Problem Formulation

After the launch vehicle clears the dense atmosphere, the three-dimensional point-mass equations of motion in vacuum are

$$\dot{\boldsymbol{r}} = \boldsymbol{V} \tag{1}$$

$$\dot{\boldsymbol{V}} = \mathbf{g}(\boldsymbol{r}) + \frac{T\mathbf{1}_T}{m(t)} \tag{2}$$

$$\dot{m} = -\frac{T}{g_0 I_{sp}} \tag{3}$$

where $\boldsymbol{r} \in R^3$ and $\boldsymbol{V} \in R^3$ are the position and inertial velocity vector in an inertial frame. The gravitational acceleration $\boldsymbol{g}$ is a function of $\boldsymbol{r}$, and g_0 is the magnitude of $\boldsymbol{g}$ at a reference radius R_0. The engine thrust magnitude is T, and the unit vector $\mathbf{1}_T$ defines the direction of the thrust vector. The vehicle mass rate $\dot{m}$ is determined by the last equation above where I_{sp} is the specific impulse of the engine. An ingenious approximation to the gravitational acceleration is the so-called linear gravity approximation[30]

$$\boldsymbol{g} = -\frac{\mu}{\bar{r}^2}\frac{\boldsymbol{r}}{\bar{r}} = -\bar{\omega}^2 \boldsymbol{r} \tag{4}$$

where μ is the gravitational parameter of the Earth, $\bar{r}$ is another reference radius (e.g., an average value of r along the ascent trajectory), and $\bar{\omega} = \sqrt{\mu/\bar{r}^3}$ is the Schuler frequency at $\bar{r}$. This approximation preserves the more important characteristic of the gravity in ascent flight, the direction, and enables analytical solution to the co-state equation in optimal exoatmospheric flight as shall be seen later. The minor gravity magnitude difference caused by this approximation in ascent typically has little influence on the validity of the solution. For multiple-burn trajectory, different value of the $\bar{\omega}$ may be used for each burn arc so that any approximation effect on gravity magnitude is minimized.

An assumption on the class of problems treated is that the initial condition $(\boldsymbol{r}_0, \boldsymbol{V}_0)$ is known. Another practical assumption on the methodology developed in this report is that the burn times of all the powered stages except for the last are all determined by their propellant loading and mass flow rate. The burn time of the last powered stage and the coast times are optimized. Therefore the final time for the complete trajectory is free. For two-burn orbital transfers, the burn time of the first burn may also need be optimized. In such a case, all the developments and equations in the rest of this report remain valid, and one additional interior switching condition will be added (cf. Ref.[10]).

For better numerical conditioning, the distances are normalized by R_0, the velocities by $\sqrt{R_0 g_0}$, and the time by $\sqrt{R_0/g_0}$. With some abuse of notation, we will still use $\boldsymbol{r}$ and $\boldsymbol{V}$ to denote the dimensionless position and velocity vector, respectively. With the above linear gravity approximation, the dimensionless equations of motion are

$$\boldsymbol{r}' = \boldsymbol{V} \tag{5}$$

$$\boldsymbol{V}' = -\omega^2 \boldsymbol{r} + A_T \mathbf{1}_T \tag{6}$$

where in above equations the differentiation is with respect to the nondimensional time $\tau = t/\sqrt{R_0/g_0}$, $\omega = \sqrt{(R_0/\bar{r})^3}$ is the nondimensional Schuler frequency, and $A_T = T/mg_0$ is the instantaneous thrust acceleration in g. The mass rate equation becomes

$$m' = -\frac{T}{c} \tag{7}$$

where $c = I_{sp}/\sqrt{R_0/g_0^3}$ is a constant for each powered stage. The orbital insertion conditions are generally in terms of k equality constraints ($k \leq 6$) on the final state

$$\phi(\boldsymbol{r}_f, \boldsymbol{V}_f) = 0 \tag{8}$$

The optimal thrust direction vector $\boldsymbol{1}_T$ is determined by the solution of the optimal control problem that minimizes the performance index

$$J = -\int_{\tau_0}^{\tau_f} m' d\tau = \int_{\tau_0}^{\tau_f} \frac{T}{c} \, d\tau \tag{9}$$

It is clear that this performance index amounts to minimization of propellant-consumption for a given initial mass. The standard optimal control theory[14] calls for the use of the Hamiltonian

$$
\begin{aligned}
H &= \boldsymbol{p}_r^T\boldsymbol{V} - \omega^2\boldsymbol{p}_V^T\boldsymbol{r} + \boldsymbol{p}_V^T\boldsymbol{1}_T A_T - p_m\frac{T}{c} - \frac{T}{c} \\
&= \boldsymbol{p}_r^T\boldsymbol{V} - \omega^2\boldsymbol{p}_V^T\boldsymbol{r} + T\left(\frac{\boldsymbol{p}_V^T\boldsymbol{1}_T}{mg_0} - \frac{p_m}{c} - \frac{1}{c}\right) := H_0 + TS
\end{aligned} \tag{10}
$$

In above Hamiltonian $\boldsymbol{p}_r$ and $\boldsymbol{p}_V$ constitute the costate vector, satisfying the differential equation

$$\begin{pmatrix} \boldsymbol{p}_r' \\ \boldsymbol{p}_V' \end{pmatrix} = -\begin{pmatrix} \partial H/\partial \boldsymbol{r} \\ \partial H/\partial \boldsymbol{V} \end{pmatrix} = \begin{pmatrix} \omega^2\boldsymbol{p}_V \\ -\boldsymbol{p}_r \end{pmatrix} \tag{11}$$

In particular, $\boldsymbol{p}_V$ is called the primer vector because the optimal thrust direction $\boldsymbol{1}_T = \boldsymbol{p}_V/||\boldsymbol{p}_V||$.[31] The switching function S, defined as

$$S = \frac{\boldsymbol{p}_V^T\boldsymbol{1}_T}{mg_0} - \frac{p_m}{c} - \frac{1}{c} \tag{12}$$

determines when to use full thrust and when to coast ($T = 0$). Specifically,

$$T = \begin{cases} T_{max} & \text{if } S > 0, \\ 0 & \text{if } S < 0. \end{cases} \tag{13}$$

The case of singular thrust arcs (when $S \equiv 0$ in a finite period of time and the thrust takes some intermediate values $0 < T < T_{max}$) is not considered because it is well known that, except for a few pathological cases, the singular solutions are not optimal in exo-atmospheric flight.[32] Suppose in our discussion that the coast between the first and second stage ends at a to-be-determined time τ_{OMS}. It is then necessary that $S(\tau_{OMS}) = 0$ (and $S(\tau) > 0$

for $\tau \in (\tau_{OMS}, \tau_f)$). Since the total final time τ_f is free for this optimal ascent problem, the Hamiltonian H defined in Eq. (10) is equal to zero along the optimal trajectory.[14] As a result, the condition $S(\tau_{OMS}) = 0$ is equivalent to

$$H_0(\tau_{OMS}) = 0 \tag{14}$$

This equation avoids the computation of the mass costate p_m thus is preferred to the condition $S(\tau_{OMS}) = 0$. For multiple coast arcs, refer to Ref.[10] for additional interior point conditions. In light of this observation and other necessary conditions discussed above, we conclude that the mass costate p_m need not be explicitly computed.

7.4   Analytical Solution for Burn Arcs

The analytical solutions to the costate equation (11) and analytical solution to state equations (5-6), first presented in Ref.[30] and later also applied in Refs.[5] and,[12] are given below for completeness. Suppose that the starting time for the ascent trajectory is τ_0. Let $\boldsymbol{p}_{V_0}$ and $\boldsymbol{p}_{r_0}$ are the (to-be-determined) initial conditions for the costate at τ_0. Define

$$\boldsymbol{\lambda}(\tau) = \begin{pmatrix} \boldsymbol{p}_V(\tau) \\ -\boldsymbol{p}_r(\tau)/\omega \end{pmatrix}, \quad \boldsymbol{\lambda}_0 = \begin{pmatrix} \boldsymbol{p}_{V_0} \\ -\boldsymbol{p}_{r_0}/\omega \end{pmatrix}$$

For $\tau \geq \tau_0$ the costate equation Eq. (11) has closed-form solution

$$\boldsymbol{\lambda}(\tau) = \begin{bmatrix} \cos[\omega(\tau-\tau_0)]I_3 & \sin[\omega(\tau-\tau_0)]I_3 \\ -\sin[\omega(\tau-\tau_0)]I_3 & \cos[\omega(\tau-\tau_0)]I_3 \end{bmatrix} \boldsymbol{\lambda}_0 := \Phi(\tau-\tau_0)\boldsymbol{\lambda}_0 \tag{15}$$

where I_3 is a 3×3 unit matrix. Define

$$\boldsymbol{I}_c(\tau, \tau_0) = \int_{\tau_0}^{\tau} \mathbf{1}_{p_V}(\zeta)\cos(\omega\zeta)A_T(\zeta)d\zeta := \int_{\tau_0}^{\tau} \boldsymbol{i}_c(\zeta)d\zeta \in R^3 \tag{16}$$

$$\boldsymbol{I}_s(\tau, \tau_0) = \int_{\tau_0}^{\tau} \mathbf{1}_{p_V}(\zeta)\sin(\omega\zeta)A_T(\zeta)d\zeta := \int_{\tau_0}^{\tau} \boldsymbol{i}_s(\zeta)d\zeta \in R^3 \tag{17}$$

where $\mathbf{1}_{p_V} = \boldsymbol{p}_V/\|\boldsymbol{p}_V\|$. Note that thrust acceleration $A_T(\cdot)$ is time-varying, because the mass is changing. Also pay attention to the the meaning of the time arguments in $\Phi(\tau-\tau_0)$, $\boldsymbol{I}_c(\cdot,\cdot)$ and $\boldsymbol{I}_s(\cdot,\cdot)$ because they will be important in multi-burn cases. Let

$$\boldsymbol{x}(\tau) = \begin{pmatrix} \boldsymbol{r}(\tau) \\ \boldsymbol{V}(\tau)/\omega \end{pmatrix}, \quad \boldsymbol{x}_0 = \begin{pmatrix} \boldsymbol{r}_0 \\ \boldsymbol{V}_0/\omega \end{pmatrix}, \quad \boldsymbol{I}(\tau, \tau_0) = \begin{bmatrix} \boldsymbol{I}_c(\tau, \tau_0) \\ \boldsymbol{I}_s(\tau, \tau_0) \end{bmatrix} \tag{18}$$

It can be easily verified that the state equations Eqs. (5) and (6) have the following solution[26]

$$\boldsymbol{x}(\tau) = \Phi(\tau-\tau_0)\boldsymbol{x}_0 + \Gamma(\tau)\boldsymbol{I}(\tau, \tau_0) \tag{19}$$

where

$$\Gamma(\tau) = \frac{1}{\omega} \begin{bmatrix} \sin(\omega\tau)I_3 & -\cos(\omega\tau)I_3 \\ \cos(\omega\tau)I_3 & \sin(\omega\tau)I_3 \end{bmatrix} \tag{20}$$

The thrust integrals I_c and I_s can be evaluated by a quadrature formula. For example, with $\delta = (\tau - \tau_0)/4$, the Milne's rule leads to[12]

$$
\begin{aligned}
I_j(\tau, \tau_0) &= \frac{(\tau - \tau_0)}{90} \left[7i_j(\tau_0) + 32i_j(\tau_0 + \delta) + 12i_j(\tau_0 + 2\delta) \right. \\
&+ \left. 32i_j(\tau_0 + 3\delta) + 7i_j(\tau_0 + 4\delta) \right], \ j = c, s
\end{aligned}
\tag{21}
$$

The values of the primer vector p_V at $\tau_0 + i\delta$ are needed in evaluating the thrust integrals, and they are given by Eq. (15) as functions of λ_0. Our experiences show that with the non-dimensionalization described in this report, the above quadratures are sufficiently accurate for powered flight up to several hundred seconds. Additional segments in time grid may be used for longer powered flight if necessary.

7.5   Solution for Coast Arcs

For coast flight where $A_T = 0$, Ref.[26] propagates the state by continuing to use Eq. (19) which has only the initial response term now. We believe that it is more advantageous to use a more accurate solution approach to the Keplerian motion in a coast arc. The f and g series in orbital mechanics[33] are an option. These series are Taylor series expansions of r and V in time, with all the coefficients expressed as functions of r_0 and V_0. The inverse-square gravity Model is used, and the accuracy of the solution is not compromised by the linear gravity approximation even with relatively large radial distance changes. A possible drawback of using the f and g series is that for a fixed number of terms in the software for the truncated Taylor series, the accuracy deteriorates as the time of coast increases. Yet another choice is to use the well established method by Goodyear[34] to solve the Kepler initial value problem as done in Ref.[11] This approach gives complete Keplerian motion solution to the problem within the machine accuracy that includes the state at a specified future time as the functions of the current state (r_0 V_0), and the gradients of the future state with respect to r_0 and V_0. This is the method we have adopted in this work.

The costate, on the other hand, may continue to be propagated by Eq. (15) during the coast. A second option is to employ the analytical solution to the costate in Keplerian motion developed by Lawden.[31] This approach preserves the Model of inverse-square gravity field, but the solution is given in a rotating frame related to the orbital motion. Once the Kepler initial value problem is solved, the corresponding costate can be readily transformed back to the original inertial frame. In this work we choose to propagate the costate by Eq. (15) for its simplicity. In any approach, the state and costate at the end of the coast are uniquely defined by their values at the beginning of the coast and the coast time.

7.6   Multiple-Shooting Formulation

In principle, the optimal exo-atmospheric ascent problem from a given initial condition $\{r_0, V_0\}$ with a coast arc is determined by 8 unknowns: $p_{r_0} \in R^3$, $p_{V_0} \in R^3$, τ_{OMS} (the time when coast stops and the second stage burn begins), and the free final time τ_f. The corresponding 8 conditions are the k-terminal conditions in Eq. (8), switching condition Eq.

(14), transversality condition $H(\tau_f) = 0$, and the other $6 - k$ transversality conditions (see Refs.[5] and[12] for more detail on how to obtain the remaining $6 - k$ transversality conditions). Directly solving for the 8 unknowns to satisfy the 8 conditions is in essence a single-shooting approach. Difficulties in convergence arise when the coast time is just Moderately long and/or the thrust acceleration of the last stage is relatively small, because in these cases the sensitivity of the problem increases and the ability for the final burn to steer the trajectory onto the terminal condition manifold weakens.

To enhance the robustness of convergence of the algorithm, two additional nodes are added to the formulation of the numerical problem. One node is placed at the end of the first powered stage. Let $\tau_{MECO} > \tau_0$ denote the instant when the engine of the first powered stage shuts down, and recall that τ_{MECO} is considered specified. The other node is naturally placed at τ_{OMS} when the coast ends and the second powered stage begins, where τ_{OMS} is to be determined. Figure 14 gives an illustration of this multiple-shooting formulation. Define the problem solution vector $\boldsymbol{y} = col(\boldsymbol{x} \ \boldsymbol{\lambda}) \in R^{12}$. In the interval (τ_0, τ_{MECO}), the solution of $\boldsymbol{y}$ is determined by the condition $\boldsymbol{y}_0$ at τ_0 by Eqs. (15) and (19). We will use $\boldsymbol{y}_{MECO}^-$ to signify the value of $\boldsymbol{y}$ at τ_{MECO} as $\tau \to \tau_{MECO}$ from the left. Introduce two additional to-be-determined vectors

$$\boldsymbol{y}_{MECO}^+ = \begin{pmatrix} \boldsymbol{x}_{MECO}^+ \\ \boldsymbol{\lambda}_{MECO}^+ \end{pmatrix}, \quad \boldsymbol{y}_{OMS}^+ = \begin{pmatrix} \boldsymbol{x}_{OMS}^+ \\ \boldsymbol{\lambda}_{OMS}^+ \end{pmatrix}$$

The propagation of $\boldsymbol{y}$ along the coast arc in the interval $(\tau_{MECO}, \ \tau_{OMS})$ is computed by using $\boldsymbol{y}_{MECO}^+$ as the starting condition. In particular we will denote such propagated value of $\boldsymbol{y}$ at τ_{OMS} by $\boldsymbol{y}_{OMS}^-$. The state and costate along the last powered trajectory in $(\tau_{OMS}, \ \tau_f)$ are propagated from $\boldsymbol{y}_{OMS}^+$. The continuity of the state and costate at τ_{MECO} and τ_{OMS} requires the following two conditions to be met

$$\boldsymbol{y}_{MECO}^- \ - \ \boldsymbol{y}_{MECO}^+ = 0 \tag{22}$$

$$\boldsymbol{y}_{OMS}^- \ - \ \boldsymbol{y}_{OMS}^+ = 0 \tag{23}$$

The above multiple-shooting formulation increases the numbers of unknowns by 24 (the number of scalars included in $\boldsymbol{y}_{MECO}^+$ and $\boldsymbol{y}_{OMS}^+$). The continuity conditions Eqs. (22) and (23) provide the same number of additional equations. Thus the dimension of the zero-finding problem is now 8+24=32. Note that the solutions for the state and costate make the problem completely analytical, from function evaluations to Jacobian computation. The evaluation of the Jacobian requires some care because of the multiple segments of the trajectory. The Appendix provides several useful equations for the part of the Jacobian involving the thrust integrals in Eqs. (16) and (17). The Modest dimension of the problem does not constitute a heavy computational requirement that cannot be met more than adequately by a desktop computer (see Section 10 for some data on CPU time).

In addition to the benefit of enhanced robustness of the algorithm, another advantage of this multiple-shooting formulation of practical significance is the simplicity of the switching condition in Eq. (14) under this setting (see Eq. (29) later for example). This feature further contributes to improve the convergence on this condition. And the complexity of the gradient of the switching condition is also reduced notably, particularly so in the case of multiple coast arcs, where the switching condition will be more complicated.[10]

47
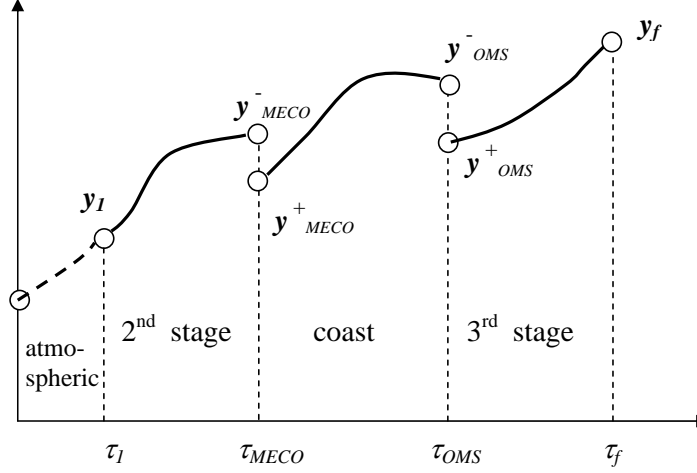
Figure 14: Multiple-shooting formulation for optimal exo-atmospheric ascent with coast

7.7   Equality Constraints

The unknowns in the problem defined in Section 6.6 are

$$\boldsymbol{z} = (\boldsymbol{\lambda}_0,\ \boldsymbol{\lambda}_{MECO}^+,\ \boldsymbol{x}_{MECO}^+,\ \tau_{OMS},\ \boldsymbol{\lambda}_{OMS}^+,\ \boldsymbol{x}_{OMS}^+,\ \tau_f) \in R^{32} \tag{24}$$

In this section we list all the 32 equality constraints that $\boldsymbol{z}$ must satisfies in order to meet the necessary condition of optimal solution and the continuity conditions. The continuity constraints in Eqs. (22) and (23) take the explicit forms of

$$\begin{align}
\boldsymbol{s}_1(\boldsymbol{z}) &= \Phi(\tau_{MECO} - \tau_0)\boldsymbol{\lambda}_0 - \boldsymbol{\lambda}_{MECO}^+ = 0 \tag{25}\\
\boldsymbol{s}_2(\boldsymbol{z}) &= \Phi(\tau_{MECO} - \tau_0)\boldsymbol{x}_0 + \Gamma(\tau_{MECO})\boldsymbol{I}^0(\tau_{MECO}, \tau_0) - \boldsymbol{x}_{MECO}^+ = 0 \tag{26}\\
\boldsymbol{s}_3(\boldsymbol{z}) &= \Phi(\tau_{OMS} - \tau_{MECO})\boldsymbol{\lambda}_{MECO}^+ - \boldsymbol{\lambda}_{OMS}^+ = 0 \tag{27}\\
\boldsymbol{s}_4(\boldsymbol{z}) &= \boldsymbol{x}_{coast}(\tau_{OMS} - \tau_{MECO}, \boldsymbol{x}_{MECO}^+) - \boldsymbol{x}_{OMS}^+ = 0 \tag{28}
\end{align}$$

where the thrust integral $\boldsymbol{I}^0(\tau_{MECO}, \tau_0) = (\boldsymbol{I}_c, \boldsymbol{I}_s)^T$ has its components defined as in Eqs. (16-17) with $\boldsymbol{\lambda}_0$ used in the computation of the primer vector $\boldsymbol{p}_V(\cdot)$. The state vector $\boldsymbol{x}_{coast}(\tau_{OMS} - \tau_{MECO}, \boldsymbol{x}_{MECO}^+)$ is the state at τ_{OMS} (the end of coast arc), propagated by the solution of the Kepler's initial value problem from τ_{MECO} with the initial condition $\boldsymbol{x}_{MECO}^+$. The scalar switching condition in Eq. (14) is conveniently expressed as

$$s_5(\boldsymbol{z}) = \boldsymbol{\lambda}_{OMS}^{+T}\boldsymbol{x}_{OMS}^+ = 0 \tag{29}$$

Let $\boldsymbol{\lambda}_f$ and $\boldsymbol{x}_f$ be the final costate and state, determined in $[\tau_{OMS}, \tau_f]$ through Eqs. (15) and (19) with the initial conditions and $\boldsymbol{\lambda}_{OMS}^+$ and $\boldsymbol{x}_{OMS}^+$, i.e.,

$$\begin{align}
\boldsymbol{\lambda}_f &= \boldsymbol{\lambda}(\tau_f, \boldsymbol{\lambda}_{OMS}^+) = \Phi(\tau_f - \tau_{OMS})\boldsymbol{\lambda}_{OMS}^+ \tag{30}\\
\boldsymbol{x}_f &= \boldsymbol{x}(\tau_f, \boldsymbol{\lambda}_{OMS}^+, \boldsymbol{x}_{OMS}^+) = \Phi(\tau_f - \tau_{OMS})\boldsymbol{x}_{OMS}^+ + \Gamma(\tau_f)\boldsymbol{I}^{oms+}(\tau_f, \tau_{OMS}) \tag{31}
\end{align}$$

where $\boldsymbol{I}^{oms+}(\tau_f, \tau_{OMS})$ is the thrust integral defined in Eq. (18) by $\boldsymbol{p}_V(\cdot)$ computed in the interval $[\tau_{OMS}, \tau_f]$ with $\boldsymbol{\lambda}_{OMS}^+$ as the initial condition.

The k orbital insertion conditions plus the $6-k$ equations derivable from the transversality conditions (cf. Refs.[11] ,,[5] and[12]) constitute another 6 constraints in the form of

$$\boldsymbol{s}_6(\boldsymbol{z}) = \boldsymbol{s}_6(\boldsymbol{x}_f, \boldsymbol{\lambda}_f) = 0 \tag{32}$$

The specifics of constraints in Eq. (32) depends on the particular set of orbital insertion conditions. References[5] and[12] provide some examples in this regard. The last constraint is the transversality condition on the Hamiltonian $H(\tau_f) = 0$ for the final time τ_f is free. This condition can be simplified by taking into consideration of the transversality condition on $p_m(\tau_f)$. Since $m(\tau_f)$ is free, we should have the transversality condition[14]

$$p_m(\tau_f) = 0$$

Use of this condition and the optimality condition of $\boldsymbol{1}_T = \boldsymbol{p}_V/\|\boldsymbol{p}_V\|$ in $H(\tau_f) = 0$ based on Eq. (10) leads to the last constraint

$$s_7(\boldsymbol{z}) = -\omega^2 \boldsymbol{\lambda}_f^T \boldsymbol{x}_f + A_T(\tau_f)\|\boldsymbol{p}_V(\tau_f)\| - \frac{T}{c} = 0 \tag{33}$$

where $\boldsymbol{p}_V(\tau_f)$ is the primer vector at τ_f, propagated by Eq. (15) from τ_{OMS} with the initial condition of $\boldsymbol{\lambda}_{OMS}^+$.

7.8   Numerical Method for Exo-Atmospheric Ascent

The optimal ascent problem in the preceding section eventually boils down to a multivariate zero-finding problem in which a system of nonlinear algebraic equations is to be solved

$$\boldsymbol{s}(\boldsymbol{z}) = 0, \quad \boldsymbol{z} \in R^{32} \tag{34}$$

where $\boldsymbol{s}(\cdot) = (\boldsymbol{s}_1, \boldsymbol{s}_2, \boldsymbol{s}_3, \boldsymbol{s}_4, s_5, \boldsymbol{s}_6, s_7) : R^{32} \to R^{32}$ is the smooth vector function defined in Section 6.7. The classical Newton-Raphson method is a common algorithm used for such a purpose. While simple and effective in many cases, the Newton-Raphson method can suffer from convergence problems when the initial guess is far from the solution, and when the Jacobian of the system (34) is singular or nearly singular. These problems are handled much better by the renowned Powell's dog-leg trust-region method.[28] This method solves the above nonlinear equations by minimizing the scalar function F

$$F(\boldsymbol{z}) = \boldsymbol{s}^T(\boldsymbol{z})\boldsymbol{s}(\boldsymbol{z}) \tag{35}$$

Obviously the solution to Eq. (34) is the solution to the minimum F. A solution of local minimum for F can exist that is not the solution of Eq. (34) if $F_{min} \neq 0$. But often times this is a case where the solution to Eq. (34) does not exist or the initial guess is very poor. In such a case one would probably be receptive to taking a solution that minimizes F.

Powell's dog-leg method is in essence a combination of the Newton and steepest-descent approach. At each iterate $\boldsymbol{z}_k$ the update is constructed as

$$\delta\boldsymbol{z} = \alpha_1 \left(\frac{\partial \boldsymbol{s}}{\partial \boldsymbol{z}}\right)^{-1} \boldsymbol{s}(\boldsymbol{z}_k) + \beta_1 \frac{\partial F}{\partial \boldsymbol{z}}$$

The coefficients α_1 and β_1 are determined in the algorithm. When $\alpha_1 = -1$ and $\beta_1 = 0$, the above update reduces to the standard Newton update. This is exactly what the algorithm does whenever the standard Newton update has a size within the trust region. Therefore the nice quadratic convergence property of the Newton method is preserved when possible. For detail of the algorithm, the reader is referred to Ref.[28] In addition to the well-documented superior performance and robustness, other attractive features of this algorithm include that (i) exact Jacobian of the system Eq. (34) is not required. In fact, the Jacobian can even be singular (in such a case $\alpha_1 = 0$ in above update), a case where the Newton method will fail; (ii) the algorithm will satisfy one of the two stopping criteria in a finite number of iterations. All these characteristics are appealing to our applications. We have encountered a number of cases with relatively challenging orbital insertion conditions for which the Newton method cannot converge. The code with Powell's method on the other hand finds the solution readily.

A singularity problem arises in the case where the optimal coast time turns out to be zero. In such a case the problem loses one parameter ($\tau_{OMS} = \tau_{MECO}$) and the switching condition in Eq. (14), hence Eq. (29), will not be needed. With the Powell's method, a simple modification of the formulation can automatically adjust the problem to such a case, so the same code can be used for both cases with and without coast arc. Define the parameterization

$$\tau_{OMS} = \frac{\tau_{coast_{max}}}{2} \sin \tilde{z}_{19} + \frac{\tau_{coast_{max}} + 2\tau_{MECO}}{2} \qquad (36)$$

where $\tau_{coast_{max}}$ is an upper bound of the coast time. Clearly when $\tilde{z}_{19} = -\pi/2$, the above $\tau_{OMS} = \tau_{MECO}$, and the coast time is zero. Now let $\tilde{z}_{19}$ replace τ_{OMS} as a parameter to be found. The constraint in Eq. (29) is modified to be

$$s_5 = (1 + \sin \tilde{z}_{19}) \boldsymbol{\lambda}_{OMS}^{+T} \boldsymbol{x}_{OMS}^{+} = 0 \qquad (37)$$

When the optimal coast time= 0, we have $\sin \tilde{z}_{19} = -1$, and $s_5 = 0$ automatically. The problem reduces to a two-burn problem, and the Powell's method has no difficulty to proceed to find the solution without the need to make any changes to the same burn-coast-burn code. In contrast, this simple approach will cause difficulty to Newton method, because when $\sin \tilde{z}_{19} = -1$ (thus $\cos \tilde{z}_{19} = 0$), the gradient of $\partial s_5 / \partial z$ is zero and the Jacobian of the problem, $\partial \boldsymbol{s} / \partial \boldsymbol{z} \in R^{32 \times 32}$, is singular. As a result, a separate code is required to handle the case where the optimal coast is close or equal to zero.

8

Analysis of the Condition $H(\tau_f) = 0$

The condition $H(\tau_f) = 0$ in Eq. (33) turns out to be a very numerically difficult constraint. This difficulty arises from the fact that, unlike other constraints in Section 6.7, Eq. (33) can have a great mismatch in numerical scaling. Specifically, the term $T(\tau_f)/c$ is about 5 orders of magnitude larger than the rest of the terms in Eq. (33) when the state and costate vectors are dimensionless and the costate vector $(\boldsymbol{p}_r^T \ \boldsymbol{p}_V^T)^T$ is chosen to have a magnitude on the order of unity, as usually done in practice. This difficulty, however, can be alleviated by proper scaling of the problem. The governing equations for the costates are

$$
\boldsymbol{p}_r' = -\frac{\partial H}{\partial \boldsymbol{r}} = -\frac{\partial \boldsymbol{g}^T(\boldsymbol{r})}{g_0 \partial \boldsymbol{r}} \boldsymbol{p}_V \tag{1}
$$

$$
\boldsymbol{p}_V' = -\frac{\partial H}{\partial \boldsymbol{V}} = -\boldsymbol{p}_r \tag{2}
$$

$$
p_m' = -\frac{\partial H}{\partial m} = \frac{T \|\boldsymbol{p}_V(\tau)\|}{m^2(\tau) g_0} \tag{3}
$$

where the optimality condition $\boldsymbol{1}_T^* = \boldsymbol{p}_V / \|\boldsymbol{p}_V\|$ has been used in Eq. (3). Clearly when the vector $(\boldsymbol{p}_r^T \ \boldsymbol{p}_V^T \ p_m)^T$ is scaled by any positive constant, the solutions to above costate equations remain unchanged. If the performance index (9) is also scaled by the same constant, the switching function S in (12) will stay the same, hence the optimal solution to the problem will be the same. Thus, if we choose to scale the performance index and $(\boldsymbol{p}_r^T \ \boldsymbol{p}_V^T \ p_m)^T$ by the value of c/T of the second stage, and, with some abuse of notation (again), still use $\boldsymbol{p}_r$ and $\boldsymbol{p}_V$ to denote the corresponding vectors after the scaling, transversality condition (33) now becomes

$$
H(\tau_f) = \boldsymbol{p}_{r_f}^T \boldsymbol{V}_f + \boldsymbol{p}_{V_f}^T \boldsymbol{g}(\boldsymbol{r}_f)/g_0 + A_T(\tau_f)\|\boldsymbol{p}_{V_f}\| - 1 = 0 \tag{4}
$$

This version of the condition $H(\tau_f) = 0$ now admits costate vector $(\boldsymbol{p}_r^T(\tau_f) \ \boldsymbol{p}_V^T(\tau_f))^T$ of magnitude comparable to those of dimensionless $\boldsymbol{V}_f$ and $\boldsymbol{r}_f$ (on the order of unity).

We shall take the scaling analysis further. In fact, the above discussion also shows that the transversality condition $H(\tau_f) = 0$ is equivalent to the following condition for any constant $\kappa_0 > 0$

$$
\boldsymbol{p}_{r_f}^T \boldsymbol{V}_f + \boldsymbol{p}_{V_f}^T \boldsymbol{g}(\boldsymbol{r}_f)/g_0 + A_T(\tau_f)\|\boldsymbol{p}_{V_f}\| - \kappa_0 = 0 \tag{5}
$$

Suppose for the moment that the burn-coast-burn problem formulated in Section 6 is solved without explicitly using the condition $H(\tau_f) = 0$. Rather, constraint (33) is replaced by the following condition

$$\boldsymbol{p}_{r_f}^T \boldsymbol{V}_f + \boldsymbol{p}_{V_f}^T \boldsymbol{g}(\boldsymbol{r}_f)/g_0 + A_T(\tau_f)||\boldsymbol{p}_{V_f}|| := H_0(\tau_f) + A_T(\tau_f)||\boldsymbol{p}_{V_f}|| > 0 \tag{6}$$

Once the problem is solved, let $\kappa_0 = H_0(\tau_f) + A_T(\tau_f)||\boldsymbol{p}_{V_f}|| > 0$. Then, the state and costate solutions so obtained and the positive constant κ_0 satisfy condition (5). In other words, the costate vector $(\boldsymbol{p}_r^T \; \boldsymbol{p}_V^T \; p_m)^T$ and the performance index can be scaled by a positive constant

$$\kappa_1 = \frac{T(\tau_f)}{\kappa_0 c}$$

so that the scaled variables will meet precisely the condition $H(\tau_f) = 0$ as in the original form in Eq. (33). This way, *all* the necessary conditions of optimality for the problem are now met. Let us formalize this finding:

Property 1:

   In a free final-time, minimum propellant-consumption, exo-atmospheric rocket flight problem, the transversality condition $H(\tau_f) = 0$ is equivalent to the condition in Eq. (6), reproduced below for the convenience of reference

$$\boldsymbol{p}_{r_f}^T \boldsymbol{V}_f + \boldsymbol{p}_{V_f}^T \boldsymbol{g}(\boldsymbol{r}_f)/g_0 + A_T(\tau_f)||\boldsymbol{p}_{V_f}|| > 0$$

   This property may be of limited practical usefulness by itself. However, we shall show next that under two very reasonable assumptions, condition (6) will be met automatically by the optimal solution without explicit enforcement. Consequently, the condition $H(\tau_f) = 0$ will be satisfied automatically. The two assumptions that we will use to establish our result are:

Assumption 1: The gravity field is a Newtonian inverse-square force field.

Assumption 2: The orbital insertion conditions in Eq. (8) are such that they satisfy the following condition in the absence of thrust $(T = 0)$

$$\frac{d\boldsymbol{\phi}(\boldsymbol{r}_f, \boldsymbol{V}_f)}{d\tau} = \boldsymbol{\phi}'(\tau_f) = 0 \tag{7}$$

   Assumption 1 means that the unpowered motion is a Keplerian orbit. Assumption 2 above is satisfied when the constraints in $\boldsymbol{\phi}(\boldsymbol{r}_f, \boldsymbol{V}_f)$ are expressed in terms of any of the Keplerian orbital elements such as $a - a_{ref} = 0$ or $e - e_{ref} = 0$, where a and e are the semi-major axis and eccentricity, respectively, and a_{ref} and e_{ref} are the specified values for them. In fact, for such a constraint $\phi_i'(\tau) \equiv 0$, $1 \le i \le k$, for $\tau \ge \tau_f$ because of the constancy of the orbital elements. Other cases where Assumption 2 is met include constraints on the radius and the magnitude of velocity for insertion into a circular orbit, or a non-circular (elliptic, parabolic or hyperbolic) orbit at the periapsis, or insertion into an elliptic orbit at the apoapsis. In the case of non-circular orbits, such a constraint meets the condition $\phi_i'(\tau_f) = 0$ only at the orbital insertion point τ_f. But this is all we need. In other words, most of typical orbital insertion conditions can be formed to satisfy Assumption 2.

With this preparation, we are ready to formally make the following claim:

Property 2:

Under Assumptions 1 and 2, the condition

$$H_0(\tau_f) = \boldsymbol{p}_{r_f}^T \boldsymbol{V}_f + \boldsymbol{p}_{V_f}^T \boldsymbol{g}(\boldsymbol{r}_f)/g_0 = 0 \tag{8}$$

is always automatically satisfied by the solution to an exo-atmospheric optimal ascent problem.

Let us justify the claim. The transversality conditions on the costate are[14]

$$\begin{pmatrix} \boldsymbol{p}_{r_f} \\ \boldsymbol{p}_{V_f} \end{pmatrix} = \begin{pmatrix} \partial \boldsymbol{\phi}^T(\boldsymbol{r}_f, \boldsymbol{V}_f)/\partial \boldsymbol{r}_f \\ \partial \boldsymbol{\phi}^T(\boldsymbol{r}_f, \boldsymbol{V}_f)/\partial \boldsymbol{V}_f \end{pmatrix} \boldsymbol{\nu} \tag{9}$$

where $\boldsymbol{\nu} \in R^k$ is a constant multiplier vector. Using the expressions of $\boldsymbol{p}_{r_f}$ and $\boldsymbol{p}_{V_f}$ from Eq. (9) in $H_0(\tau_f)$, we have

$$H_0(\tau_f) = \boldsymbol{\nu}^T \left[\frac{\partial \boldsymbol{\phi}(\boldsymbol{r}_f, \boldsymbol{V}_f)}{\partial \boldsymbol{r}_f} \boldsymbol{V}_f + \frac{\partial \boldsymbol{\phi}(\boldsymbol{r}_f, \boldsymbol{V}_f)}{\partial \boldsymbol{V}_f} \boldsymbol{g}(\boldsymbol{r}_f)/g_0 \right] \tag{10}$$

Note that $\boldsymbol{r}'_f = \boldsymbol{V}_f$ and $\boldsymbol{V}'_f = \boldsymbol{g}(\boldsymbol{r}_f)/g_0$ when $T = 0$. So in the absence of thrust, the sum in the above equation is equivalent to

$$H_0(\tau_f) = \boldsymbol{\nu}^T \left[\frac{\partial \boldsymbol{\phi}(\boldsymbol{r}_f, \boldsymbol{V}_f)}{\partial \boldsymbol{r}_f} \boldsymbol{r}'_f + \frac{\partial \boldsymbol{\phi}(\boldsymbol{r}_f, \boldsymbol{V}_f)}{\partial \boldsymbol{V}_f} \boldsymbol{V}'_f \right] = \boldsymbol{\nu}^T \boldsymbol{\phi}'(\tau_f) = 0 \tag{11}$$

where Assumption 2 has been used in arriving this condition. This conclusion is first arrived in Ref.[11] based on an analysis of orthogonality of the final costate vector with respect to the manifold of the admissible variations of the final state vector. Since $H(\tau_f) = H_0(\tau_f) + T(\tau_f)S(\tau_f)$ and $H(\tau_f) = 0$ is a transversality condition for the optimal solution, an immediate corollary of $H_0(\tau_f) = 0$ is that under Assumptions 1 and 2, the switching function satisfies $S(\tau_f) = 0$ along the optimal solution. Note that $S(\tau_f) = 0$ is not always true because τ_f is not an interior switching point.

Because $A_T(\tau_f)\|\boldsymbol{p}_V(\tau_f)\| > 0$, condition (6) is always met if $H_0(\tau_f) = 0$. Combining Property 1 and 2, we see that the enforcement of the transversality condition $H(\tau_f) = 0$ is not necessary in finding the solution to the problem of present interest to us, hence the conclusion

Property 3:

In a free final-time, minimum propellant-consumption, exo-atmospheric ascent problem in which Assumptions 1 and 2 are satisfied, the transversality condition $H(\tau_f) = 0$ need not be enforced in the solution process.

Based on the above conclusion, one of the to-be-determined unknowns in Eq. (24) for the burn-coast-burn problem may be eliminated in correspondence with the removal of the condition $H(\tau_f) = 0$. Instead of doing so, which has no clear and convenient choice, we choose

to keep the same unknowns as in Eq. (24). But we pick a simpler and easier replacement to the condition $H(\tau_f) = 0$. Numerous such choices exist. For instance, one could be

$$s_7 = \boldsymbol{p}_V^T(\tau_f)\boldsymbol{p}_V(\tau_f) - c_7 = 0 \tag{12}$$

where $c_7 > 0$ is a constant. The only function of this last constraint is to maintain the same number of equations as the number of unknowns in Eq. (24), and keep the Jacobian of the constraints nonsingular. Therefore, in the numerical code, we do not even need to actually evaluate s_7 and attempt to enforce $s_7 = 0$. Rather, we can always set $s_7 \equiv 0$ every time when the value of s_7 is required (in the case of Eq. (12), this would be equivalent to choosing c_7 to be exactly equal to $\boldsymbol{p}_V^T(\tau_f)\boldsymbol{p}_V(\tau_f)$ each time s_7 is evaluated). When the linear gravity approximation is used, another alternative is to use the constraint

$$s_7 = \boldsymbol{p}_r^T(\tau_f)\boldsymbol{p}_r(\tau_f) + \omega^2\boldsymbol{p}_V^T(\tau_f)\boldsymbol{p}_V(\tau_f) - 1 = 0 \tag{13}$$

It can be easily shown that the magnitude of the vector $\boldsymbol{\lambda}(\tau) = (\boldsymbol{p}_r^T\ \omega\boldsymbol{p}_V^T)^T$ is constant under the linear gravity Model. Therefore if the initial value of $\boldsymbol{\lambda}(\tau_0)$ is scaled to have unit length, the constraint in Eq. (13) is trivially met. Such a normalizing constraint is found to be beneficial to convergence when the exo-atmospheric algorithm interacts with the endo-atmospheric algorithm in certain way as described in Ref.[27]

In the end, we still have the same number of unknowns in Eq. (24) as the number of constraints $\boldsymbol{s} = (\boldsymbol{s}_1, \boldsymbol{s}_2, \boldsymbol{s}_3, \boldsymbol{s}_4, s_5, \boldsymbol{s}_6, s_7)$, where s_7 is a trivial constraint, and the rest are defined in the preceding section.

Finally, as a general interest, it is worthwhile to point out that a similar claim can be made for the minimum-time optimal ascent problem for insertion into a Keplerian orbit. In such a problem, the transversality condition on the Hamiltonian is[14]

$$H(\tau_f) = \boldsymbol{p}_{r_f}^T\boldsymbol{V}_f + \boldsymbol{p}_{V_f}^T\boldsymbol{g}(\boldsymbol{r}_f)/g_0 + T(\tau_f)\frac{\boldsymbol{p}_V^T(\tau_f)\boldsymbol{1}_T(\tau_f)}{m(\tau_f)g_0} = 1$$

Suppose that the problem is solved without explicitly enforcing the above condition. Property 2 above still holds, which together with $\boldsymbol{1}_T(\tau_f) = \boldsymbol{p}_V(\tau_f)/\|\boldsymbol{p}_V(\tau_f)\|$ leads to

$$H(\tau_f) = T(\tau_f)\frac{\|\boldsymbol{p}_V(\tau_f)\|}{m(\tau_f)g_0} > 0 \tag{14}$$

We now make note of two observations of invariance pertinent to the problem:

1. The costate vector $(\boldsymbol{p}_r^T\ \boldsymbol{p}_V^T)^T$ can be scaled by any constant and the costate equations (1–2) are still satisfied;

2. When the costate vector $(\boldsymbol{p}_r^T\ \boldsymbol{p}_V^T)^T$ is scaled by any *positive* constant, the resultant optimal control from the optimality condition and the state trajectory will remain the same.

Hence if we scale the costate by a positive constant

$$\kappa_2 = \frac{m(\tau_f)g_0}{T(\tau_f)\|\boldsymbol{p}_{V_f}\|} > 0$$

54

the optimal solution will remain unchanged, and we will now have $H(\tau_f) = 1$ without explicitly enforcing it. Indeed, the maximum principle by Pontryagin *et al*[35] only requires $H(\tau_f) > 0$ for the minimum-time problem, which is already met by Eq. (14).

9

Orbital Insertion Modes

As noted a few times earlier in the report, the orbital insertion conditions are specified in terms of k equality constraints on the final state; More specifically, typical inertial insertion conditions are defined by a subset of the six target orbital elements. This section will describe several terminal Modes that specify various commonly seen launch missions. Another component of this section is to show how the Lagrange multipliers in the transversality conditions of the costate may be eliminated by manipulating the transversality conditions and orbital insertion conditions cleverly. The elimination of these unknown multipliers has two major advantages: first it reduces the number of unknowns needed to be found; more importantly, it increases the algorithm convergence reliability significantly. The second point arises from the fact that these multipliers have no physical meaning, and they may differ in magnitude with that of the rest of variables considerably. Having to solve for these multipliers would make the solution process more difficult in general.

In this section the final state and costate are denoted by

$$\boldsymbol{x}_f = \left(\begin{array}{c} \boldsymbol{r}_f \\ \boldsymbol{V}_f \end{array} \right) \tag{1}$$

$$\boldsymbol{p}_f = \left(\begin{array}{c} \boldsymbol{p}_{V_f} \\ \boldsymbol{p}_{r_f} \end{array} \right) \tag{2}$$

9.1 Mode 31

This Mode consists of three orbital insertion conditions defined by the desired target orbital element values for the semi-major axis a^*, eccentricity e^*, and inclination i^*. The ascending node, true anomaly, and argument periapsis are considered free. Since the point of insertion into the target orbit is not specified, this is a so-called free attachment Mode, and the final flight path angle γ_f is unconstrained. When the insertion flight path angle is specified such as $\gamma_f = 0$, thereby requiring the insertion point be at either the perigee or apogee of an elliptic orbit, one additional constraint will be needed. (See Mode 43/44 below).

It should be noted that naming convention for the orbital insertion Modes is such that the first digit ("3" in this case) indicates the number of orbital insertion constraints in each case.

The second digit simply designate different different variation of orbital insertion conditions while the number of constraints is the same.

A unit vector is constructed that relates the vehicle's final position and velocity to the target orbit inclination. Define a z-axis unit vector in the Earth Centered Inertial (ECI) frame as

$$\mathbf{1}_{NE} = \begin{bmatrix} 0 \\ 0 \\ 1 \end{bmatrix} \tag{3}$$

This vector transformed to the Guidance frame is given by

$$\mathbf{1}_{NG} = T_{EP}\,\mathbf{1}_{NE} \tag{4}$$

where T_{EP} is the transformation matrix as defined in section 2.4.

From orbital mechanics, the magnitude of the required final angular momentum vector of the vehicle at the orbital insertion point is given by

$$h^* = \sqrt{a^*(1 - e^{*2})} \tag{5}$$

Using the above expressions, the three orbital insertion conditions $\mathbf{\Psi} \in R^3$ can be written as

$$\frac{1}{2}\left(\mathbf{r}_f \times \mathbf{V}_f\right)^T \left(\mathbf{r}_f \times \mathbf{V}_f\right) - \frac{1}{2}h^{*2} = 0 \tag{6}$$

$$\frac{1}{2}\mathbf{V}_f{}^T\mathbf{V}_f - \frac{1}{r_f} + \frac{1}{2a^*} = 0 \tag{7}$$

$$\mathbf{1}_{NG}{}^T\left(\mathbf{r}_f \times \mathbf{V}_f\right) - h^* \cos i^* = 0 \tag{8}$$

where $r_f = \|\mathbf{r}_f\|$.

Additional Terminal Conditions After Elimination of Lagrange Multipliers

The 6 transversality equations in Eqs. (25-26) in this contain 3 Lagrange multipliers ($\boldsymbol{\nu} \in R^3$):

$$\mathbf{p}_{r_f} - \left(\mathbf{V}_f \times \mathbf{h}_f\right)\nu_1 - \frac{1}{r_f{}^3}\mathbf{r}_f\nu_2 - \left(\mathbf{V}_f \times \mathbf{1}_{NG}\right)\nu_3 = 0 \tag{9}$$

$$\mathbf{p}_{V_f} + \left(\mathbf{r}_f \times \mathbf{h}_f\right)\nu_1 - \mathbf{V}_f\nu_2 + \left(\mathbf{r}_f \times \mathbf{1}_{NG}\right)\nu_3 = 0 \tag{10}$$

After using the conditions (6–8) and the transversality equations to eliminate the $\boldsymbol{\nu}$ (the algebraic manipulations are lengthy and thus not shown here), three additional terminal conditions are resulted in:

$$\left(\mathbf{h}_f{}^T\mathbf{p}_{r_f}\right)\left[\mathbf{h}_f{}^T\left(\mathbf{r}_f \times \mathbf{1}_{NG}\right)\right] + \left(\mathbf{h}_f{}^T\mathbf{p}_{V_f}\right)\left[\mathbf{h}_f{}^T\left(\mathbf{V}_f \times \mathbf{1}_{NG}\right)\right] = 0 \tag{11}$$

$$r_f{}^3\mathbf{V}_f{}^T\mathbf{p}_{r_f} - \mathbf{r}_f{}^T\mathbf{p}_{V_f} = 0 \tag{12}$$

$$\mathbf{p}_{r_f}{}^T\left(\mathbf{r}_f \times \mathbf{V}_N\right)\left(\mathbf{r}_f \times \mathbf{h}_f\right)^T\left(\mathbf{V}_f \times \mathbf{r}_N\right) + \mathbf{p}_{V_f}{}^T\left(\mathbf{V}_f \times \mathbf{r}_N\right)\left(\mathbf{V}_f \times \mathbf{h}_f\right)^T\left(\mathbf{r}_f \times \mathbf{V}_N\right) = 0 \tag{13}$$

where $\mathbf{h}_f = \mathbf{r}_f \times \mathbf{V}_f$ is the angular momentum vector, $\mathbf{r}_N = \mathbf{r}_f \times \mathbf{1}_{NG}$, and $\mathbf{V}_N = \mathbf{V}_f \times \mathbf{1}_{NG}$.

9.2 Mode 41

Mode 41 consists of four orbital insertion conditions defined by the desired target orbital element values for the semi-major axis a^*, eccentricity e^*, inclination i^*, and ascending node Ω^*. The true anomaly and argument periapsis are considered free. This is also a free attachment Mode in that the final flight path angle γ_f is unconstrained allowing the insertion point to be located at any point on the target orbit.

A unit angular momentum vector of the desired target orbital plane is constructed from the target inclination and ascending node. This vector, defined in the ECI frame is given as

$$\mathbf{1}_{HE} = \begin{bmatrix} \sin \Omega^* \sin i^* \\ -\cos \Omega^* \sin i^* \\ \cos i^* \end{bmatrix} \tag{14}$$

This vector transformed to the Guidance frame is given by

$$\mathbf{1}_{HG} = T_{EP}\,\mathbf{1}_{HE} \tag{15}$$

Again, the magnitude of the required final angular momentum vector of the vehicle at the orbital insertion point is given by

$$h^* = \sqrt{a^*(1 - e^{*2})} \tag{16}$$

Using the above expressions, the four orbital insertion conditions $\mathbf{\Psi} \in R^4$ can be written as

$$\boldsymbol{r}_f \times \boldsymbol{V}_f - \boldsymbol{h}_f{}^* = 0 \quad \in R^3 \tag{17}$$

$$\frac{1}{2}\boldsymbol{V}_f{}^T\boldsymbol{V}_f - \frac{1}{r_f} + \frac{1}{2a^*} = 0 \tag{18}$$

where $r_f = \|\boldsymbol{r}_f\|$ and $\boldsymbol{h}_f{}^* = h^*\mathbf{1}_{HG}$

Additional Terminal Conditions After Elimination of Lagrange Multipliers

The 6 transversality conditions involving the Lagrange multiplier vector $\boldsymbol{\nu} \in R^4$ are now given by

$$\boldsymbol{p}_{r_f} + \text{skew}\,(\boldsymbol{V}_f) \begin{bmatrix} \nu_1 \\ \nu_2 \\ \nu_3 \end{bmatrix} - \frac{1}{r_f{}^3}\boldsymbol{r}_f\nu_4 = 0 \tag{19}$$

$$\boldsymbol{p}_{V_f} - \text{skew}\,(\boldsymbol{r}_f) \begin{bmatrix} \nu_1 \\ \nu_2 \\ \nu_3 \end{bmatrix} - \boldsymbol{V}_f\nu_4 = 0 \tag{20}$$

where $\text{skew}(\boldsymbol{V}_f)$ and $\text{skew}(\boldsymbol{r}_f)$ are the 3×3 skew matrices formed by the elements of $\boldsymbol{V}_f$ and $\boldsymbol{r}_f$, respectively. After much algebraic operation to eliminate $\boldsymbol{\nu}$ from the above equations,

we can have two additional terminal conditions free of $\boldsymbol{\nu}$:

$$\boldsymbol{p}_{r_f}{}^T \boldsymbol{V}_f - \frac{1}{r_f{}^3}\boldsymbol{p}_{V_f}{}^T \boldsymbol{r}_f = 0 \tag{21}$$

$$\boldsymbol{p}_{r_f}{}^T \left(\boldsymbol{r}_f \times \boldsymbol{h}_f{}^*\right) + \boldsymbol{p}_{V_f}{}^T \left(\boldsymbol{V}_f \times \boldsymbol{h}_f{}^*\right) = 0 \tag{22}$$

9.3   Mode 43/44

This Mode involves four orbital insertion constraints defined by the desired target orbital element values for the semi-major axis a^*, eccentricity e^* inclination, i^*, and a final flight path angle γ_f, which is set to zero. Therefore the insertion point is either at the perigee (Mode 43) or apogee of the target orbit (Mode 44) and the final dimensionless position and velocity are given by

$$r_f^* = a^*(1 - e^*) \tag{23}$$

$$V_f^* = \sqrt{\frac{1 + e^*}{a^*(1 - e^*)}} \tag{24}$$

for the perigee and

$$r_f^* = a^*(1 + e^*) \tag{25}$$

$$V_f^* = \sqrt{\frac{1 - e^*}{a^*(1 + e^*)}} \tag{26}$$

for the apogee.

A unit vector is constructed that relates the vehicle's final position and velocity to the target orbit inclination. Define a z-axis unit vector in the ECI frame as

$$\mathbf{1}_{NE} = \begin{bmatrix} 0 \\ 0 \\ 1 \end{bmatrix} \tag{27}$$

This vector transformed to the Guidance frame is given by

$$\mathbf{1}_{NG} = T_{EP}\,\mathbf{1}_{NE} \tag{28}$$

Using the above expressions, the four orbital insertion conditions $\boldsymbol{\Psi} \in R^4$ can be written as

$$\frac{1}{2}\boldsymbol{r}_f{}^T \boldsymbol{r}_f - \frac{1}{2}r_f^{*\,2} = 0 \tag{29}$$

$$\frac{1}{2}\boldsymbol{V}_f{}^T \boldsymbol{V}_f - \frac{1}{2}V_f^{*\,2} = 0 \tag{30}$$

$$\mathbf{1}_{NG}{}^T \left(\boldsymbol{r}_f \times \boldsymbol{V}_f\right) - r_f^* V_f^* \cos i^* = 0 \tag{31}$$

$$\boldsymbol{r}_f{}^T \boldsymbol{V}_f = 0 \tag{32}$$

The 6 transversality conditions involving the Lagrange multiplier vector $\boldsymbol{\nu} \in R^4$ are now given by

$$\boldsymbol{p}_{r_f} - \boldsymbol{r}_f \nu_1 - (\boldsymbol{V}_f \times \mathbf{1}_{NG}) \nu_3 - \boldsymbol{V}_f \nu_4 = 0 \tag{33}$$

$$\boldsymbol{p}_{V_f} - \boldsymbol{V}_f \nu_2 + (\boldsymbol{r}_f \times \mathbf{1}_{NG}) \nu_3 - \boldsymbol{r}_f \nu_4 = 0 \tag{34}$$

Performing strategic dot and cross product operations on these conditions enables the elimination of the multiplier vector $\boldsymbol{\nu} \in R^4$. This results in 2 additional independent terminal constraint equations free of the multipliers given by

$$\boldsymbol{V}_f{}^T \boldsymbol{p}_{r_f} r_f^{*2} - \boldsymbol{r}_f{}^T \boldsymbol{p}_{V_f} V_f^{*2} = 0 \tag{35}$$

$$\left[(\boldsymbol{r}_f \times \boldsymbol{V}_f)^T \boldsymbol{p}_{r_f} \right] \left[(\boldsymbol{r}_f \times \boldsymbol{V}_f)^T (\boldsymbol{r}_f \times \mathbf{1}_{NG}) \right]$$
$$+ \left[(\boldsymbol{r}_f \times \boldsymbol{V}_f)^T \boldsymbol{p}_{V_f} \right] \left[(\boldsymbol{r}_f \times \boldsymbol{V}_f)^T (\boldsymbol{V}_f \times \mathbf{1}_{NG}) \right] = 0 \tag{36}$$

9.4   Mode 46

This Mode involves four insertion conditions defined by the desired final position magnitude r_f^*, velocity magnitude V_f^*, inclination i^*, and flight path angle γ_f^* which is not necessarily zero. If values of r_f^*, V_f^*, and γ_f^* are chosen properly, the orbital insertion point can be placed anywhere in the orbit using this Mode. So Mode 43/44 is a special case to Mode 46.

Again, a unit vector is constructed that relates the vehicle's final position and velocity to the desired inclination. Define a z-axis unit vector in the ECI frame as

$$\mathbf{1}_{NE} = \begin{bmatrix} 0 \\ 0 \\ 1 \end{bmatrix} \tag{37}$$

This vector transformed to the Guidance frame is given by

$$\mathbf{1}_{NG} = T_{EP} \, \mathbf{1}_{NE} \tag{38}$$

The four resulting insertion conditions can be written as

$$\frac{1}{2} \boldsymbol{r}_f{}^T \boldsymbol{r}_f - \frac{1}{2} r_f^{*2} = 0 \tag{39}$$

$$\frac{1}{2} \boldsymbol{V}_f{}^T \boldsymbol{V}_f - \frac{1}{2} V_f^{*2} = 0 \tag{40}$$

$$\mathbf{1}_{NG}{}^T (\boldsymbol{r}_f \times \boldsymbol{V}_f) - r_f^* V_f^* \cos \gamma_f^* \cos i^* = 0 \tag{41}$$

$$\boldsymbol{r}_f{}^T \boldsymbol{V}_f - r_f^* V_f^* \sin \gamma_f^* = 0 \tag{42}$$

<u>Additional Terminal Conditions After Elimination of Lagrange Multipliers</u>

The 6 transversality cantons involving the Lagrange multiplier vector $\boldsymbol{\nu} \in R^4$ are now given by

$$\boldsymbol{p}_{r_f} - \boldsymbol{r}_f \nu_1 - \left(\boldsymbol{V}_f \times \mathbf{1}_{NG}\right) \nu_3 - \boldsymbol{V}_f \nu_4 = 0 \tag{43}$$

$$\boldsymbol{p}_{V_f} - \boldsymbol{V}_f \nu_2 + \left(\boldsymbol{r}_f \times \mathbf{1}_{NG}\right) \nu_3 - \boldsymbol{r}_f \nu_4 = 0 \tag{44}$$

The 2 final manipulated additional terminal conditions free of the Lagrange multipliers are

$$\left(\boldsymbol{V}_f{}^T \boldsymbol{p}_{r_f}\right) r_f^* - \left(\boldsymbol{r}_f{}^T \boldsymbol{p}_{V_f}\right) V_f^* + r_f^* V_f^* \sin \gamma_f^* \left[\boldsymbol{V}_f{}^T \boldsymbol{p}_{V_f} - \boldsymbol{r}_f{}^T \boldsymbol{p}_{r_f}\right] = 0 \tag{45}$$

$$\left(\boldsymbol{h}_f{}^T \boldsymbol{p}_{r_f}\right) \left(\boldsymbol{h}_f{}^T \boldsymbol{r}_N\right) + \left(\boldsymbol{h}_f{}^T \boldsymbol{p}_{V_f}\right) \left(\boldsymbol{h}_f{}^T \boldsymbol{V}_N\right) = 0 \tag{46}$$

where $\boldsymbol{h}_f = \boldsymbol{r}_f \times \boldsymbol{V}_f$ is the angular momentum vector, $\boldsymbol{r}_N = \boldsymbol{r}_f \times \mathbf{1}_{NG}$, and $\boldsymbol{V}_N = \boldsymbol{V}_f \times \mathbf{1}_{NG}$.

9.5   Mode 51

Mode 51 consists of five orbital insertion conditions defined by the desired target orbital element values for the semi-major axis a^*, eccentricity e^*, inclination i^*, ascending node Ω^*, and and a final flight path angle $\gamma_f = 0$. This is the Mode to be used for a launch-to-rendezvous mission. The insertion point is at the perigee or apogee of the target orbit and the final position and velocity are given again as

$$r_f^* = a^*(1 - e^*) \tag{47}$$

$$V_f^* = \sqrt{\frac{1 + e^*}{a^*(1 - e^*)}} \tag{48}$$

for the perigee and

$$r_f^* = a^*(1 + e^*) \tag{49}$$

$$V_f^* = \sqrt{\frac{1 - e^*}{a^*(1 + e^*)}} \tag{50}$$

for the apogee. As was done for Mode 41, a unit angular momentum vector of the desired target orbital plane is constructed from the target inclination and ascending node and is given as

$$\mathbf{1}_{HE} = \begin{bmatrix} \sin \Omega^* \sin i^* \\ -\cos \Omega^* \sin i^* \\ \cos i^* \end{bmatrix} \tag{51}$$

This vector transformed to the Guidance frame is given by

$$\mathbf{1}_{HG} = T_{EP}\, \mathbf{1}_{HE} \tag{52}$$

Again, the magnitude of the required final angular momentum vector of the vehicle at the orbital insertion point is given by

$$h^* = \sqrt{a^*(1 - e^{*2})} \tag{53}$$

Using the above expressions, the five orbital insertion conditions $\mathbf{\Psi} \in R^5$ can be written as

$$\frac{1}{2}\boldsymbol{r}_f{}^T\boldsymbol{r}_f - \frac{1}{2}r_f^{*2} = 0 \tag{54}$$

$$\frac{1}{2}\boldsymbol{V}_f{}^T\boldsymbol{V}_f - \frac{1}{2}V_f^{*2} = 0 \tag{55}$$

$$\boldsymbol{r}_f{}^T\boldsymbol{V}_f = 0 \tag{56}$$

$$\boldsymbol{r}_f{}^T\boldsymbol{1}_{HG} = 0 \tag{57}$$

$$\boldsymbol{V}_f{}^T\boldsymbol{1}_{HG} = 0 \tag{58}$$

Additional Terminal Conditions After Elimination of Lagrange Multipliers

The 6 transversality conditions involving the Lagrange multiplier vector $\boldsymbol{\nu} \in R^5$ are now given by

$$\boldsymbol{p}_{r_f} - \boldsymbol{r}_f\nu_1 - \boldsymbol{V}_f\nu_3 - \boldsymbol{1}_{HG}\nu_4 = 0 \tag{59}$$

$$\boldsymbol{p}_{V_f} - \boldsymbol{V}_f\nu_2 - \boldsymbol{r}_f\nu_3 - \boldsymbol{1}_{HG}\nu_5 = 0 \tag{60}$$

The final manipulated additional terminal condition free of the Lagrange multipliers is

$$\left(\boldsymbol{V}_f{}^T\boldsymbol{p}_{r_f}\right) r_f^{*2} - \left(\boldsymbol{r}_f{}^T\boldsymbol{p}_{V_f}\right) V_f^{*2} = 0 \tag{61}$$

10

Combining Atmospheric and Vacuum Algorithms

The endo-atmospheric and exo-atmospheric ascent guidance algorithms developed in the preceding parts of this report must work together to produce a complete optimal ascent trajectory from liftoff to orbital insertion. The challenge in this approach of combining the atmospheric ascent algorithm with the vacuum ascent algorithm lies in the integration, since the vacuum algorithm is not just a special case of the atmospheric algorithm with zero atmospheric density. Instead of solving the entire problem with one algorithm, each of the algorithms solves one part of an optimal control problem and the trajectories in each part are then pieced together. This division, however, poses a unique problem for the atmospheric ascent algorithm because the end conditions for the atmospheric portion of the ascent are not defined a priori. Rather, they are a result of the final solution. For instance, the usual multiple-shooting formulation at the junction point will have difficulty since two different algorithms are at work, each covering only one part of the entire trajectory.

Our approach is to integrate the algorithms through the iteration on the state at the end point τ_1 of the first stage where the atmospheric algorithm stops and the vacuum algorithm begins. Figure 15 illustrates the point. From a starting estimate of the state at τ_1, the vacuum algorithm generates an optimal trajectory to the target orbit and returns the corresponding costate at τ_1. The atmospheric algorithm in turn solves a TPBVP in which the initial state is that at the lift-off and the final costate is the one just found by the vacuum algorithm at τ_1. This atmospheric ascent solution will provide a new state at τ_1. The above process then repeats until the states found at τ_1 in two consecutive cycles are practically the same.

The algorithmic implementation of the above approach is given below. Starting from an initial guess of the state at τ_1, denoted by $\boldsymbol{x}_{\tau_1}^{(0)}$, our integration algorithm proceeds with the iterations as follows:

1. Set $k = 0$.

2. With the known $\boldsymbol{x}_{\tau_1}^{(k)}$, the vacuum algorithm finds the optimal ascent trajectory in $(\tau_1,\ \tau_f)$, possibly including the coast, from $\boldsymbol{x}_{\tau_1}^{(k)}$ to the targeting condition Eq. (8). As
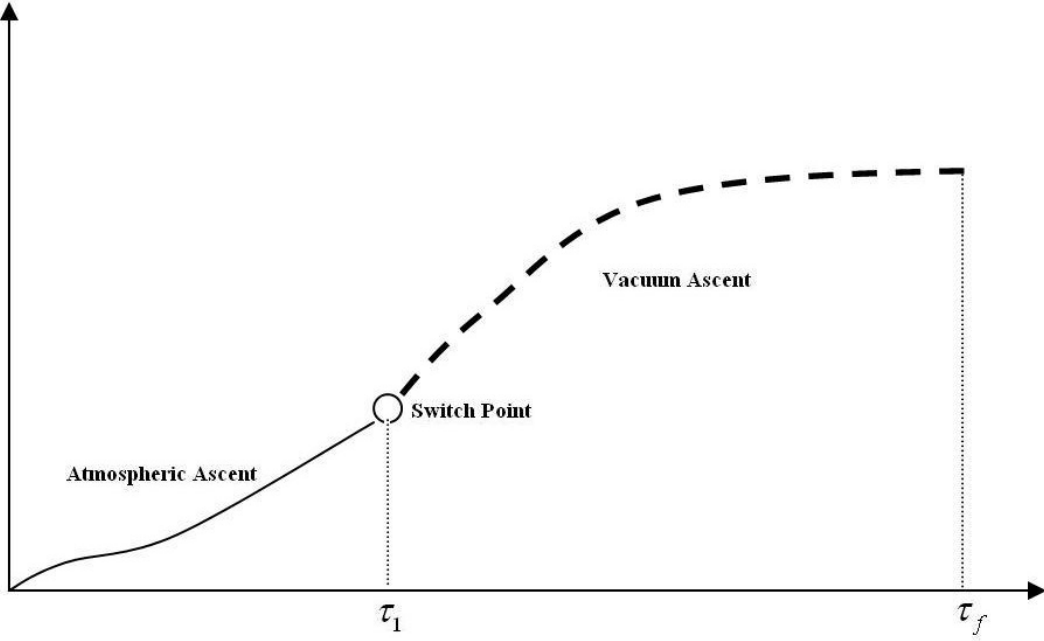
Figure 15: Integration of endo- and exo-atmospheric optimal trajectories

a part of the solution the vacuum algorithm returns the corresponding costate $\boldsymbol{p}_{\tau_1}^{(k)}$ at τ_1.

3. The just obtained $\boldsymbol{p}_{\tau_1}^{(k)}$ is used as the required boundary condition at τ_1 for the costate in the interval $(0, \ \tau_1)$ for the atmospheric algorithm. The initial state at $\tau = 0$ is known. The TPBVP for the atmospheric algorithm is then well defined. Upon the convergence of the algorithm, a new state at τ_1 is found as a result, and this new state is denoted as $\tilde{\boldsymbol{x}}_{\tau_1}^{(k+1)}$.

4. If $||\tilde{\boldsymbol{x}}_{\tau_1}^{(k+1)} - \boldsymbol{x}_{\tau_1}^{(k)}|| \leq \delta$ for some pre-selected small constant $\delta > 0$, set $\boldsymbol{x}_{\tau_1} = \tilde{\boldsymbol{x}}_{\tau_1}^{(k+1)}$, and stop. Otherwise, let

$$\boldsymbol{x}_{\tau_1}^{(k+1)} = \varepsilon \tilde{\boldsymbol{x}}_{\tau_1}^{(k+1)} + (1 - \varepsilon)\boldsymbol{x}_{\tau_1}^{(k)} \tag{1}$$

where $0 < \varepsilon \leq 1$ is a constant. Set $k = k + 1$ and return to Step 2 above.

At the conclusion of the above process, both the state $\boldsymbol{x}$ and costate $\boldsymbol{p}$ are continuous at τ_1. All the necessary conditions for the optimal ascent problem are satisfied in $[0, \ \tau_f]$. In other words, the solutions obtained for $\boldsymbol{x}(\cdot)$ and $\boldsymbol{p}(\cdot)$ in the two algorithms form a continuous extremal for the complete optimal ascent problem.

The above search for the correct state $\boldsymbol{x}_{\tau_1}$ essentially constitutes a fixed-point problem. Consider the case when $\varepsilon = 1$ in Eq. (1). We may represent the process of obtaining $\tilde{\boldsymbol{x}}_{\tau_1}^{(k+1)}$ based on $\boldsymbol{x}_{\tau_1}^{(k)}$ by the mapping $\tilde{\boldsymbol{x}}_{\tau_1}^{(k+1)} = \mathcal{M}(\boldsymbol{x}_{\tau_1}^{(k)})$. The above procedure therefore amounts to

finding the solution to the fixed-point equation

$$\boldsymbol{x}_{\tau_1} = \mathcal{M}(\boldsymbol{x}_{\tau_1}) \tag{2}$$

In this context, Eq. (1) with $\varepsilon \neq 1$ simply is a modified fixed-point iteration in the form of

$$\boldsymbol{x}_{\tau_1}^{(k+1)} = \varepsilon \mathcal{M}(\boldsymbol{x}_{\tau_1}^{(k)}) + (1 - \varepsilon)\boldsymbol{x}_{\tau_1}^{(k)} \tag{3}$$

Evidently the fixed-point solution to Eq. (3) for any $\varepsilon \neq 0$ is the solution to Eq. (2) as well. The introduction of an appropriate ε in Eq. (3) can aid the convergence of the fixed-point iteration which may not always happen with $\varepsilon = 1$. A similar technique is discussed in Ref.[37] In our application this technique has a geometric interpretation: an $\varepsilon < 1$ in the early cycles of the iterations can prevent $\boldsymbol{x}_{\tau_1}^{(k+1)}$ from departing too far from $\boldsymbol{x}_{\tau_1}^{(k)}$, an concurrence which in some cases may result in the trajectory going through the Earth. Once $\tilde{\boldsymbol{x}}_{\tau_1}^{(k+1)}$ and $\boldsymbol{x}_{\tau_1}^{(k)}$ are sufficiently close, an $\varepsilon = 1$ can be used to further speed up the convergence.

In fact, the need to solve the special endo-atmospheric TPBVP in Step 2 above inspires another fixed-point formulation of this sub-problem, and consequently a fixed-point iteration algorithm may be used to solve this particular problem. Appendix III provides some further exposition on this aspect.

11

V&V of Exo-Atmospheric Ascent Guidance Algorithm

The objective in this section is to verify and validate the analytical multiple shooting (AMS) exo-atmospheric ascent guidance algorithm developed here by comparing the solutions from the algorithm to those obtained by using an industry standard trajectory optimization software. Toward this purpose, 41 different mission scenarios are designed and tested with a two-stage launch vehicle Model. All the orbital insertion Modes in Section 9 are tested. To verify the results found by the AMS algorithm, an industry standard aerospace trajectory optimization software, called Optimal Trajectories by Implicit Simulation[29] (OTIS), is employed to compute the burn-coast-burn trajectory under the identical condition. Further comparison is done with closed-loop simulated trajectories. In the closed-loop simulations, the AMS algorithm serves as the guidance algorithm, generating the optimal exo-atmospheric trajectory from the current state to the orbital insertion point at a guidance cycle of 1 Hz. The actual trajectory is simulated by integrating Eqs. (1–3) with an inverse-square gravity field. The optimal thrust direction and throttle command (full thrust or coast) are determined by the AMS algorithm. The closed-loop simulations are an ultimate check for the validity of the open-loop solution found. If the closed-loop trajectory matches the open-loop one closely, the approximations adopted in obtaining the open-loop solution are well justified.

11.1   Two-Stage Launch Vehicle

A two-stage vehicle configuration is used for the verification and validation of the analytical multiple shooting (AMS) algorithm for burn-coast-burn vacuum ascent trajectory optimization problem. The vehicle's first stage is the so-called "Super X-33". This is a vehicle Model with all the data identical to those of the X-33, except that the specific impulse of the engine is doubled. The second stage is the X-37 piggy-backed on the Super X-33. The launch site for all test cases shown below is at Kennedy Space Center (KSC), (longitude=$-80.85°$, latitude=$28.29°$). This information is necessary in establishing the Guidance inertial frame for the launch as well as the required Guidance to ECI coordinate transformation. The computation of the optimal first stage ascent trajectory through the atmosphere is divided into two segments: the endo-atmospheric portion and the exo-atmospheric portion, separated at

a given altitude around 90 km. The exo-atmospheric portion of the Super X-33 is regarded as the first upper (vacuum) stage. After the burn-out of the X-33, the X-37 continues the optimal ascent trajectory by first coasting for an optimal duration and then starting burn of the X-37 until orbital insertion. Data used in the AMS algorithm for the Super X-33 and X-37 are given below.

Table 4: Vehicle data of the first vacuum) stage of "Super X-33"

Thrust (vac)	2,303,000 N
I_{sp} (vac)	711.395 sec
Empty weight	37,557 kg
Propellant weight	27,000 kg

Table 5: X-37 Data

Thrust (vac)	29,269 N
I_{sp} (vac)	330 sec
Empty Weight	1,270 kg
Propellant Weight	3,628.74 kg
Payload Weight	544.31 kg

11.2   Mode 31 / 43 Comparisons

As mentioned previously, Mode 31 consists of three orbital insertion conditions defined by the desired target orbital element values for the semi-major axis a^*, eccentricity e^*, and inclination i^*. This is a free attachment Mode in that the final flight path angle γ_f is not constrained. Mode 43 requires the same orbital insertion conditions as Mode 31 in addition to constraining the final flight path angle to zero such that the insertion point is the perigee of the target orbit. A set of test cases with target orbital insertion conditions as well as an identical set for Mode 43 including the final $\gamma_f = 0$ constraint is given below in Table 6 . In addition, three circular target orbits for Mode 43 are listed.

Results for Mode 31 and 43 test cases in Table 6 are listed in Table 7 and 8 respectively. Recalling that the burn time of the first vacuum burn is fixed and determined from propellant availability, the difference in converged second burn time directly translates into the difference in deliverable payload mass, or vehicle performance. Both the second vacuum burn time and mass are listed for convenience. In terms of vehicle performance, all methods match quite closely and is very noteworthy in that OTIS is a direct approach using collocation, a very different method than the indirect AMS method that finds the trajectory based on optimal control necessary conditions. Further, the extent to which the open-loop AMS trajectory matches the full non-linear gravity closed-loop simulation driven by a current condition open-loop AMS solution at each guidance cycle is reassuring. The small differences in the open-loop AMS solution and the converged closed-loop simulation is to be expected

Table 6: Mode 31 & 43 Target Orbits

Case	Mode	perigee alt. (km)	e	i (deg)	γ_f (deg)
1	31	300	0.1	51.6	Free
2	31	500	0.1	51.6	Free
3	31	1000	0.1	51.6	Free
4	31	300	0.3	51.6	Free
5	31	500	0.3	51.6	Free
6	31	1000	0.3	51.6	Free
7	31	500	0.1	28.5	Free
8	31	500	0.3	28.5	Free
9	43	300	0.1	51.6	0.0
10	43	500	0.1	51.6	0.0
11	43	1000	0.1	51.6	0.0
12	43	300	0.3	51.6	0.0
13	43	500	0.3	51.6	0.0
14	43	1000	0.3	51.6	0.0
15	43	500	0.1	28.5	0.0
16	43	500	0.3	28.5	0.0
17	43	1000	0.0	51.6	0.0
18	43	500	0.0	51.6	0.0
19	43	500	0.0	51.6	0.0

and results from approximations made in the Analytical Multiple-Shooting problem formulation such as the linear gravity approximation and thrust quadrature approximations for each burn. During the coast phase the launch vehicle is trading kinetic energy for potential energy. The higher the orbital insertion altitude, the longer the coast arc tends to be, and the more critical is its length to the performance of the vehicle. Figures 16 and 17 show the closed-loop altitude and velocity profiles along with their corresponding body axis pitch and yaw angle time histories with respect to the guidance frame defined with a 2-3-1 rotation sequence. The small yaw angles in figure 17 are due to the fact that the launch azimuth is oriented in the direction defined by the target orbit inclination so as to minimize the yaw maneuvers, a common practice in launch vehicle guidance. Some cases were found where, depending on insertion conditions, higher altitudes did not always translate to a longer coast arc, however, the presence of the optimized coast arc remains very significant to vehicle performance.

The performance index on the final mass in the optimal burn-coast-burn problem appears to be fairly insensitive to the coast time. Indeed, significant differences in the converged coast time between OTIS and the AMS method does not result in significant differences in orbital insertion mass. This disagreement in optimal coast times becomes much more noticeable for higher altitude orbital insertions. The two methods do, however, find similar solutions for the lower altitude orbits. These results are illustrated in Figures 18 and 19, which show the altitude and velocity profiles for both OTIS and the closed-loop AMS simulation for cases 2 and 3. The small changes in insertion mass even for disproportionately large changes in

coast time results in a "flat optimum" and it was found that direct methods such as OTIS tend to converge to different solutions, most notably in the converged coast time, depending on initial guess inputs. The AMS method, an indirect method, did not suffer from this problem and was consistently able to converge to the same solution for the same case for large changes in the initial guess.

An important comparison between all Mode 31 and the respective Mode 43 test cases is seen from the value of the true anomaly at insertion. Mode 43 requires the insertion point be the perigee of the resulting target orbit, which evident from the table is not always the optimal insertion point. This result is consistent with both the AMS method and OTIS. This is exemplified by test case 6 and 14 which results in a difference in second burn time of approximately 5 seconds equating to a deliverable payload difference of 45.25 kg, a substantial difference assuming payload mass of 500 kg. Figures 20 and 21 show the optimized ascent trajectory and insertion target orbit for case 6. This illustrates the non-perigee optimal insertion point and shows the true anomaly at insertion. Figure 21 is viewed in the direction of the target orbit angular momentum vector allowing this to be seen easily.

Table 7: Mode 31 Results

Case	Method	Coast (sec)	2nd Burn (sec)	Final Mass (kg)	True Anomaly (deg)
1	OTIS	24.6240	334.0512	2421.7212	7.43432
	AMS	20.0371	334.3829	2416.8352	0.00000
	AMS closed-loop	26.4927	331.7147	2438.4000	6.21815
2	OTIS	135.2167	345.9007	2314.5505	11.41668
	AMS	126.1379	346.8496	2304.0113	0.00000
	AMS closed-loop	134.5228	343.6698	2329.8000	11.13721
3	OTIS	293.8752	389.6641	1918.7385	10.29114
	AMS	226.0024	390.5117	1908.8694	0.00000
	AMS closed-loop	243.9442	388.0392	1922.5500	12.08240
4	OTIS	54.2115	386.7927	1944.7088	2.38447
	AMS	43.9989	386.6586	1943.7401	0.00000
	AMS closed-loop	53.1648	384.5900	1958.7500	1.29348
5	OTIS	152.4945	395.3354	1867.4451	6.08704
	AMS	132.0432	396.0864	1858.4179	0.00000
	AMS closed-loop	142.8387	393.3418	1877.3000	6.75834
6	OTIS	257.3082	427.3834	1577.5918	11.21645
	AMS	207.8629	429.6897	1554.3082	0.00000
	AMS closed-loop	226.6251	425.4743	1587.7000	12.72862
7	OTIS	129.0704	345.5416	2317.7982	12.07388
	AMS	129.1712	345.9306	2312.3279	0.00000
	AMS closed-loop	137.6387	342.7682	2338.8500	10.95298
8	OTIS	126.4071	394.4810	1875.1728	8.65202
	AMS	135.5817	395.3242	1865.3161	0.00000
	AMS closed-loop	146.4793	392.5993	1886.3500	6.55688

Table 8: Mode 43 Results

| Case	Method	Coast (sec)	2nd Burn (sec)	Final Mass (kg)	True Anomaly (deg)
9	OTIS	34.1034	334.7211	2415.6628	0.00000
	AMS	18.1730	334.3978	2416.6999	0.00001
	AMS closed-loop	26.7410	331.8191	2438.4000	0.00688
10	OTIS	159.6698	346.2189	2311.6721	0.00000
	AMS	120.9575	346.9562	2303.0468	0.00000
	AMS closed-loop	130.6213	344.5979	2320.7500	0.05877
11	OTIS	307.5751	390.7985	1908.4785	0.00000
	AMS	219.6417	390.9169	1905.2019	0.00001
	AMS closed-loop	238.4151	390.0967	1904.4500	0.33734
12	OTIS	36.9882	387.9814	1933.9577	0.00000
	AMS	35.0215	386.7056	1943.3146	0.00000
	AMS closed-loop	50.0246	384.6953	1958.7500	0.01839
13	OTIS	166.2501	396.8354	1853.8786	0.00000
	AMS	112.2931	396.3527	1856.0081	0.00000
	AMS closed-loop	126.6136	394.5985	1868.2500	0.01075
14	OTIS	293.3618	431.1413	1543.6039	0.00000
	AMS	187.5651	430.6763	1545.3795	0.00000
	AMS closed-loop	206.4970	430.4641	1542.4500	0.06999
15	OTIS	170.3501	348.4420	2291.5658	0.00000
	AMS	106.7140	350.5581	2270.4490	0.41001
	AMS closed-loop	128.8965	346.3061	2302.6500	0.11132
16	OTIS	172.6211	397.0370	1852.0556	0.00000
	AMS	115.9672	395.5898	1862.9119	0.00000
	AMS closed-loop	130.4734	393.7107	1877.3000	0.08649
17	OTIS	27.7985	302.1463	2710.2808	N/A
	AMS	21.4543	301.3659	2715.6387	N/A
	AMS closed-loop	26.5988	298.4510	2737.0500	N/A
18	OTIS	174.1365	315.1391	2592.7694	N/A
	AMS	132.5598	315.9119	2583.9970	N/A
	AMS closed-loop	139.9287	313.4425	2601.3000	N/A
19	OTIS	319.0053	366.0883	2131.9660	N/A
	AMS	240.3386	365.9951	2130.7439	N/A
	AMS closed-loop	258.0000	365.2223	2130.7000	N/A
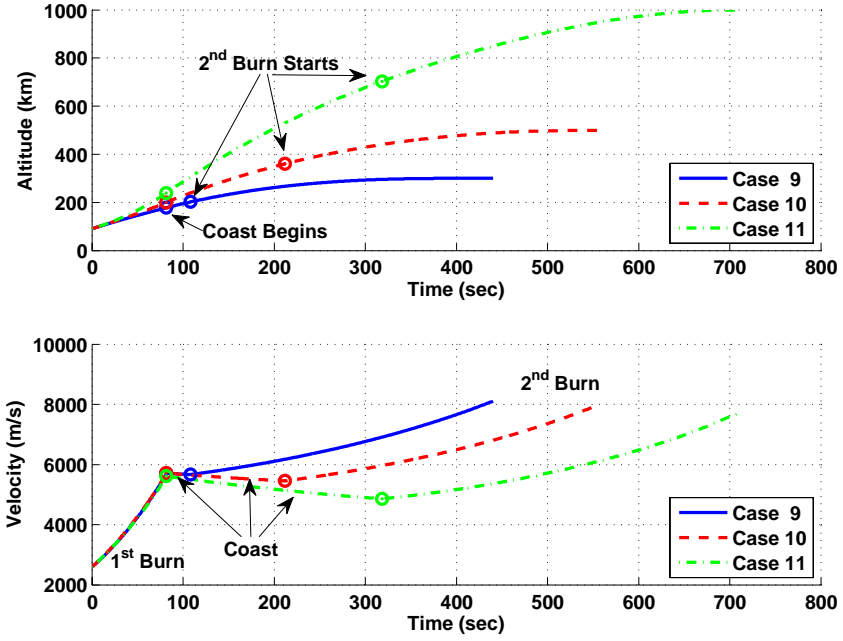
Figure 16: Altitude and velocity profiles of the AMS closed-loop burn-coast-burn ascent trajectories for cases 9-11
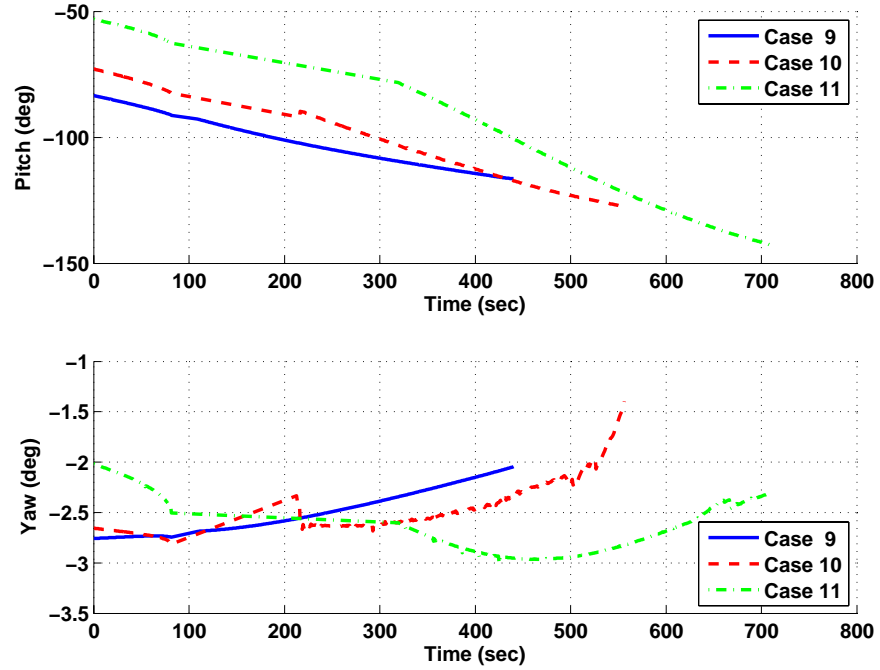

Figure 17: Pitch and yaw angles along the AMS closed-loop burn-coast-burn ascent trajectories with respect to the launch plumbline (guidance) frame for cases 9-11
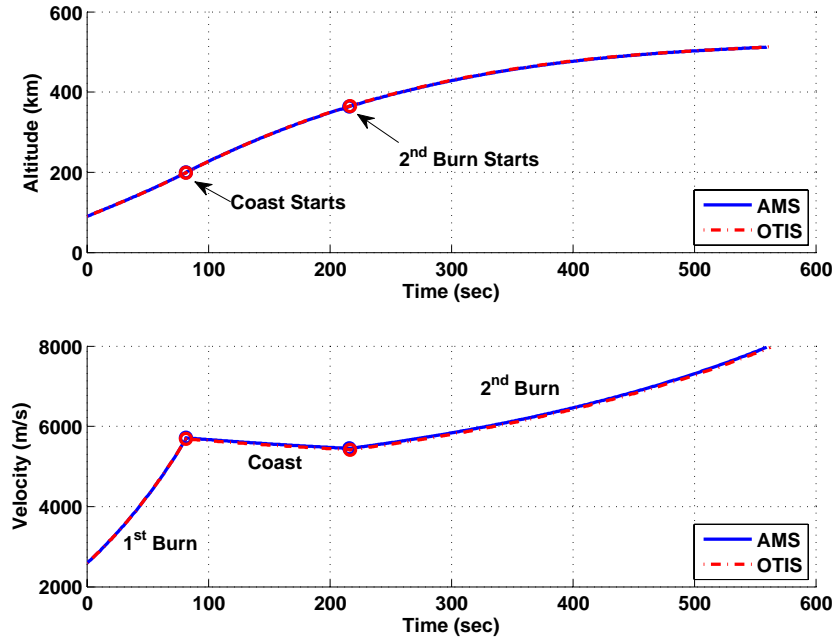
71

Figure 18: AMS and OTIS altitude and velocity comparison for case 2
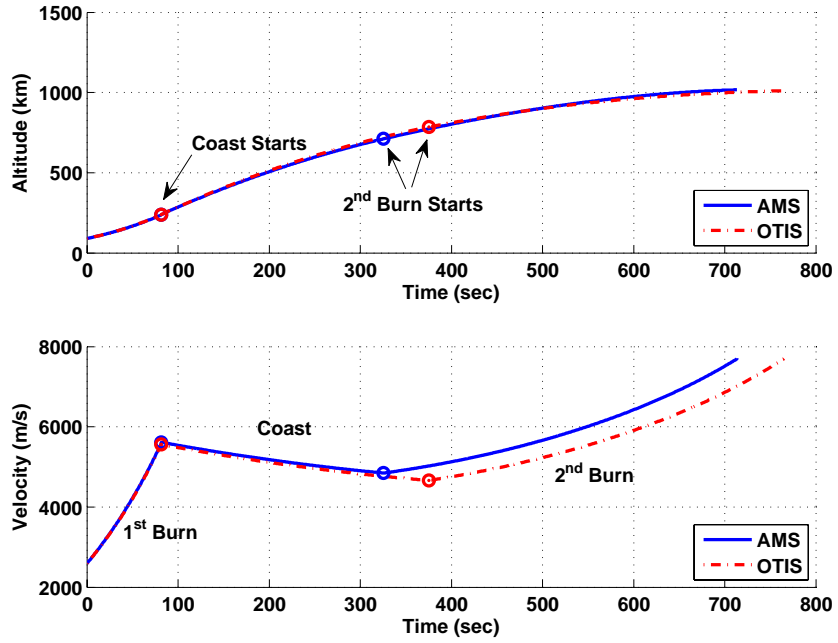

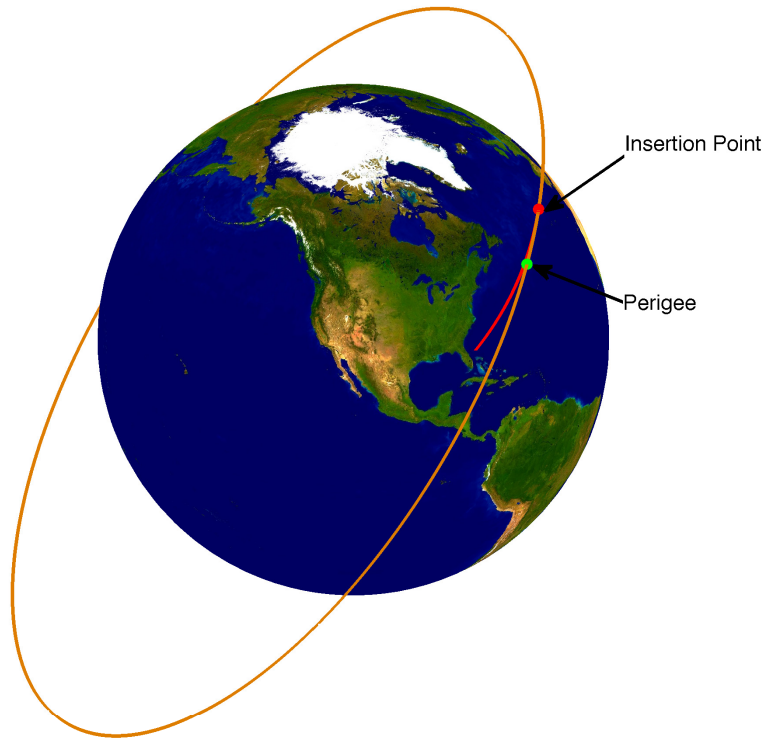Figure 19: AMS and OTIS altitude and velocity comparison for case 3

Figure 20: AMS closed-loop ascent trajectory and target insertion orbit for case 6
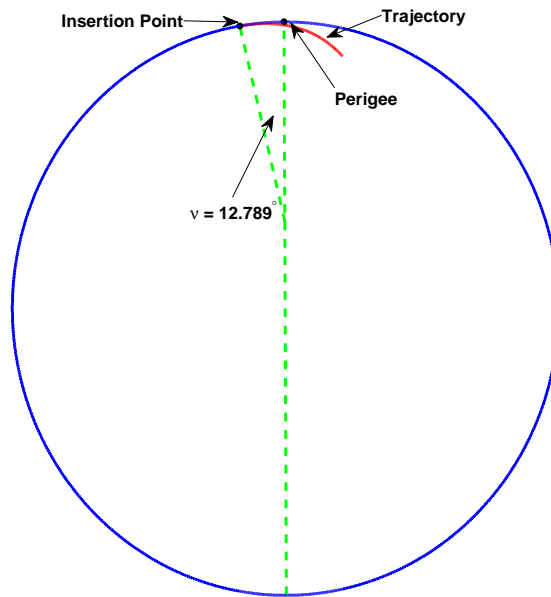

Figure 21: AMS closed-loop ascent trajectory and target insertion orbit illustrating true anomaly at insertion for case 6

11.3 Mode 41 / 51 Comparisons

Mode 41 consists of four orbital insertion conditions defined by the desired target orbital element values for the semi-major axis a^*, eccentricity e^*, inclination i^*, and ascending node Ω^*. This is a free attachment Mode in that the final flight path angle γ_f is not constrained. Mode 51 requires the same orbital insertion conditions as Mode 41 in addition to constraining the final flight path angle to zero such that the insertion point is the perigee of the target orbit. Modes 41 and 51 are similar to Modes 31 and 43 respectively and differ only from the additional constraint on the ascending node. This fixes the target orbital plane leaving the only unknown the location of the perigee on the orbit. A set of test cases with target orbital insertion conditions as well as an identical set for Mode 51 including the final $\gamma_f = 0$ constraint is given below in table 9 . In addition, three circular target orbits for Mode 51 are listed. This set of test cases is identical to those of 31 and 43 with the addition of a fixed ascending node Ω^*. It should be noted that for the initial conditions used for all test cases in this work, target orbits with unconstrained ascending nodes converge to approximately $255°$ for inclinations of $51.6°$ and $185°$ for inclinations of $28.5°$.

Table 9: Mode 41 & 51 Target Orbits

Case	Mode	perigee alt. (km)	e	i (deg)	γ_f (deg)	Ω (deg)
20	41	300	0.1	51.6	Free	250
21	41	500	0.1	51.6	Free	250
22	41	1000	0.1	51.6	Free	250
23	41	300	0.3	51.6	Free	250
24	41	500	0.3	51.6	Free	250
25	41	1000	0.3	51.6	Free	250
26	41	500	0.1	28.5	Free	180
27	41	500	0.3	28.5	Free	180
28	51	300	0.1	51.6	0.0	250
29	51	500	0.1	51.6	0.0	250
30	51	1000	0.1	51.6	0.0	250
31	51	300	0.3	51.6	0.0	250
32	51	500	0.3	51.6	0.0	250
33	51	1000	0.3	51.6	0.0	250
34	51	500	0.1	28.5	0.0	180
35	51	500	0.3	28.5	0.0	180
36	51	1000	0.0	51.6	0.0	250
37	51	500	0.0	51.6	0.0	250
38	51	500	0.0	51.6	0.0	250

Results for Mode 41 and 51 test cases in table 9 are listed in table 10 and 11 respectively. Again, both the second vacuum burn time and mass are listed for convenience. In terms of vehicle performance, all methods match quite closely as was the case for Modes 31 and 43. The open-loop AMS trajectory continues to match the full non-linear gravity AMS closed-loop simulation which is evidence the AMS method has no problem handling the additional constraint on the problem. For Modes 31 and 43 it was seen that for higher orbital insertion

altitudes, the longer the coast arc tends to be, and the more critical is its length to the performance of the vehicle. This trend is again seen for Mode 51 wherein the insertion point must be the perigee of the target orbit. However, from the results in table 10, longer coast arcs for higher insertion altitudes is not the typical outcome for Mode 41. This is explained by the variation of optimal insertion points found in terms of the true anomaly at insertion in addition to the unconstrained target orbit perigee direction which can be much different from the corresponding Mode 51 cases.

The ascending node constraint enforced in Modes 41 and 51 appears to be the dominate constraint. Enforcing the ascending node constraint Ω in addition to the semi-major axis a, eccentricity e, and inclination i fully defines the target orbital plane leaving the only unknown the perigee direction. It can be seen from table 9 that the target orbit ascending node for Modes 41 and 51 are set at approximately a 5° offset from their natural unconstrained converged values for the initial conditions used in this work. Enforcing this constraint has a very noticeable impact on vehicle performance. Every Mode 41 and 51 case results in a significantly lower final mass than the corresponding Mode 31 and 43 case as shown in tables 10 and 11. Constraining the ascending node to the values in table 9 forces the launch vehicle to make substantial out of plane maneuvers during ascent to align itself with the target orbital plane. These out of plane maneuvers require longer second burn times causing a significant decrease in final vehicle mass at insertion. For Modes 31 and 43 it was shown (see Fig. 17) that the yaw angle is generally very small during the ascent due to the initial launch azimuth direction. Expensive out of plane maneuvers result in much larger yaw angles during the ascent as illustrated in Figure 23 with a comparison of case 33 and corresponding case 14. Figure 22 shows the altitude and velocity profiles for these cases. As seen in the figures, both cases have very similar velocity and altitude profiles. In case 33, however, the large yawing motion during the ascent results in a longer second burn time by approximately 7 seconds translating into a final mass reduction of approximately 63 kg. Further verifying these results, Figures 24 and 25 show two views of the optimized trajectory and target insertion orbit for Mode 41 test case 25. Again, easily seen from the figures, the launch vehicle performs substantial yawing maneuvers to align and insert itself into the desired target orbit. These results are consistent for both the AMS method and OTIS.

Similar to Modes 31 and 43, the performance index on the final mass in the optimal burn-coast-burn problem continues to be fairly insensitive to the coast time. Significant differences in the converged coast time between OTIS and the AMS method does not result in significant differences in orbital insertion mass. This disagreement in optimal coast times is again more noticeable for higher altitude orbital insertions. The small changes in insertion mass for disproportionately large changes in coast time is in part due to the "flat optimum" characteristics of the optimal ascent problem as mentioned previously. Further understanding of the terminal Mode constraints can help explain this "flat optimum" most often resulting in optimal coast time disagreement between the AMS and OTIS methods. Is is to be noted and understood that the desired target orbits are not fully defined. Mode 41 and 51 does fix the target orbital plane as mentioned, but does not constrain the perigee location. Given this, for any test case the AMS and OTIS methods may not insert into the same orbit and in general they will not, however, both satisfy the terminal constraints at

insertion. This freedom helps explain why both methods can agree in terms of vehicle performance even with substantial disagreement in optimal coast time. This can be demonstrated by analyzing a Mode 51 case wherein the orbital plane and insertion point on the orbit are fixed. Figure 26 shows the AMS and OTIS trajectories and insertion orbits for Mode 51 case 33. Both insertions must be at the perigee of the target orbit, and from table 11, it is seen that the optimized coast arc for the OTIS trajectory is substantially longer that that found by the AMS method. For this reason, it is expected that the OTIS insertion point be somewhat downrange of the AMS insertion and indeed this is the result. Figure 27 illustrates the "flat optimum" characteristic of the problem, again for case 33, by sweeping the coast time over a 200 second window bracketing the original converged coast times found by both the OTIS and AMS methods. As can be seen from figure, the variation in final burn time is very insensitive to the coast duration in this range. Discussed above, the only remaining unconstrained orbital insertion parameter is the argument of perigee, the variation of which is also shown in the figure. Easily seen from the figure, increasing the coast time simply pushes the perigee direction and insertion point further downrange from the launch site, and visa versa.

In regards to the solutions obtained from OTIS, a few comments should be noted. In many cases, adjusting the guessed final burn time values was required to obtain the optimal solution found. Further change of these values could prevent OTIS from retrieving the same solution, or in some situations even a similar solution. It was observed that adjusting the coast and or final burn time bounds would additionally have a significant impact on the converged solution. This prevented obtaining a sweep solution simply by adjusting the coast time duration while leaving all other parameters unchanged. In addition, scaling of problem parameters highly influenced convergence rates and final solutions. It is recognized that OTIS is a very general trajectory optimization software allowing for much user configuration, hence and a more complete knowledge of its proper use in regards to this specific problem may have relieved some of these issues.

Table 10: Mode 41 Results

Case	Method	Coast (sec)	2nd Burn (sec)	Final Mass (kg)	True Anomaly (deg)
20	OTIS	259.9649	351.9201	2260.1084	28.88764
	AMS	219.0324	352.1562	2255.9867	20.38100
	AMS closed-loop	231.6762	349.9753	2275.5000	19.04381
21	OTIS	270.9058	361.7805	2170.9273	11.64281
	AMS	191.2724	363.3863	2154.3536	0.98688
	AMS closed-loop	204.5619	364.9046	2139.7500	1.61218
22	OTIS	299.9342	398.2460	1841.1204	8.97000
	AMS	211.8645	401.6461	1808.1027	10.88184
	AMS closed-loop	227.6674	400.0388	1813.9500	12.15001
23	OTIS	265.5381	399.2454	1832.0815	10.57011
	AMS	210.3717	397.9093	1841.9211	6.07592
	AMS closed-loop	227.1023	396.1889	1850.1500	5.03092
24	OTIS	222.2749	407.0645	1761.3633	2.34400
	AMS	158.6010	407.3729	1756.2756	3.49641
	AMS closed-loop	174.9292	404.9382	1777.7500	4.93180
25	OTIS	285.9631	442.5412	1440.4989	11.85391
	AMS	149.9988	438.8672	1471.2519	11.49603
	AMS closed-loop	164.2296	436.9191	1488.1500	14.74207
26	OTIS	130.6578	345.4328	2318.7820	12.48016
	AMS	88.9099	346.4386	2307.7307	12.04604
	AMS closed-loop	94.3723	343.9121	2329.8000	15.26107
27	OTIS	219.2165	396.1688	1859.9077	0.00000
	AMS	15.7832	396.0942	1858.3475	12.37148
	AMS closed-loop	21.0860	393.6329	1877.3000	16.89375

Table 11: Mode 51 Results

| Case	Method	Coast (sec)	2nd Burn (sec)	Final Mass (kg)	True Anomaly (deg)
28	OTIS	188.2341	356.1665	2221.7026	0.23231
	AMS	168.6447	356.3202	2218.3019	0.00000
	AMS closed-loop	177.0205	354.2091	2230.2500	0.16114
29	OTIS	228.3949	366.3698	2129.4199	0.22885
	AMS	188.8833	363.5015	2153.3116	0.00001
	AMS closed-loop	198.4591	361.0573	2166.9000	0.01260
30	OTIS	326.8909	398.5508	1838.3637	0.22111
	AMS	230.6249	401.1288	1812.7843	0.00001
	AMS closed-loop	248.3052	399.9408	1823.0000	0.02116
31	OTIS	182.9739	399.9333	1825.8598	0.19379
	AMS	170.6421	399.4623	1827.8661	0.00000
	AMS closed-loop	182.1409	397.6953	1841.1000	0.03067
32	OTIS	235.0993	405.9083	1771.8204	0.14380
	AMS	180.8982	405.2135	1761.5226	0.00000
	AMS closed-loop	193.6338	404.8655	1777.7500	0.00441
33	OTIS	317.0431	438.8030	1474.3089	0.13850
	AMS	201.6559	437.9284	1479.7483	0.00000
	AMS closed-loop	220.8111	437.2554	1479.1000	0.09196
34	OTIS	151.4102	347.6747	2298.5052	0.22882
	AMS	122.5030	346.2990	2308.9943	0.00000
	AMS closed-loop	132.1887	343.9411	2329.8000	0.00545
35	OTIS	158.9689	397.0465	1851.9692	0.14366
	AMS	114.0376	395.8322	1860.7183	0.00000
	AMS closed-loop	128.4066	394.1371	1868.2500	0.00323
36	OTIS	200.4568	330.3483	2455.2113	N/A
	AMS	171.1778	330.8833	2448.5065	N/A
	AMS closed-loop	178.0483	328.7342	2465.5500	N/A
37	OTIS	159.8574	339.3094	2374.1639	N/A
	AMS	196.6761	337.2291	2391.0771	N/A
	AMS closed-loop	204.6825	334.6980	2411.2500	N/A
38	OTIS	337.8690	380.0354	2005.8236	N/A
	AMS	248.9145	378.2907	2019.4688	N/A
	AMS closed-loop	265.7263	377.1271	2022.1000	N/A
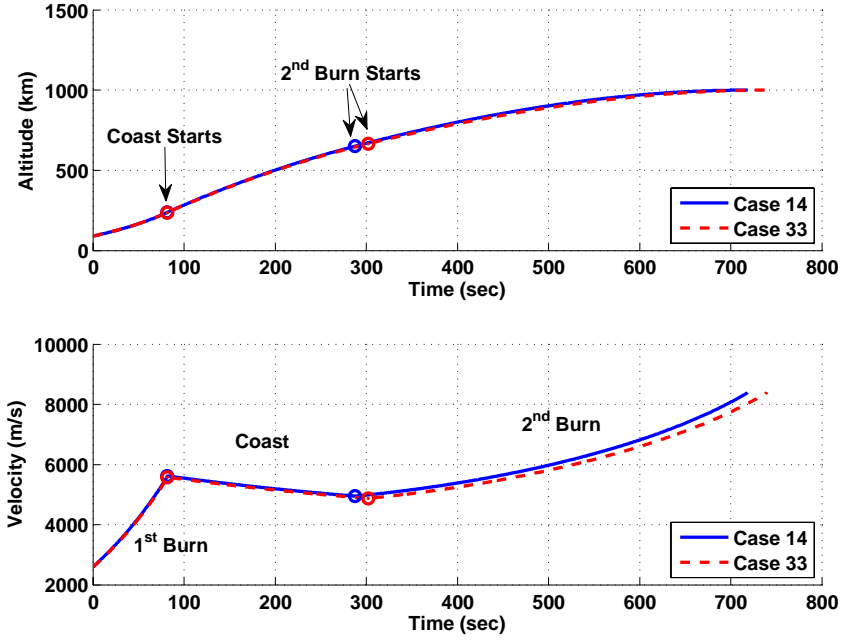
Figure 22: Altitude and velocity profiles of the AMS closed-loop burn-coast-burn ascent trajectories for cases 14 and 33
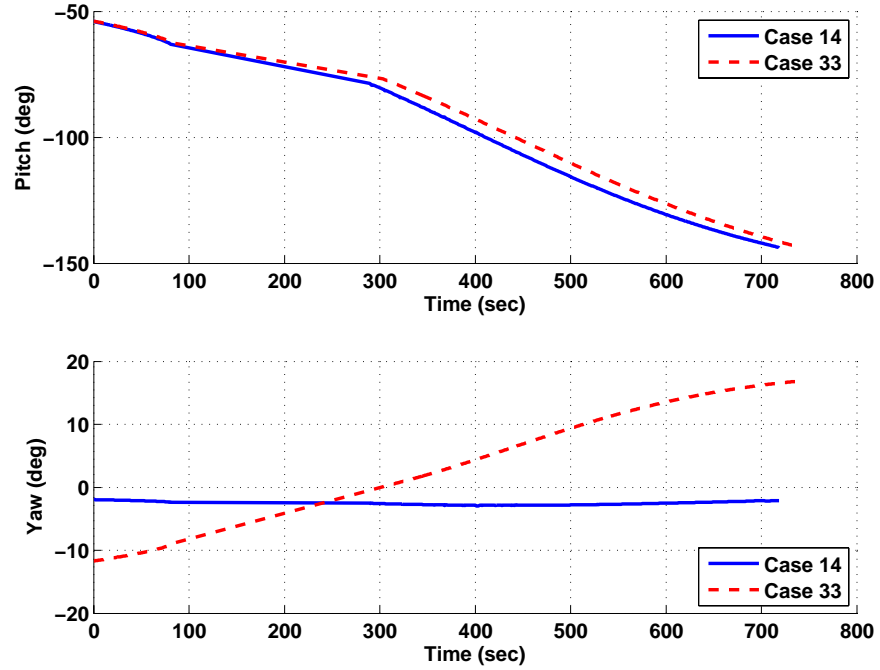

Figure 23: Pitch and yaw angles along the AMS closed-loop burn-coast-burn ascent trajectories with respect to the launch plumbline (guidance) frame for cases 14 and 33
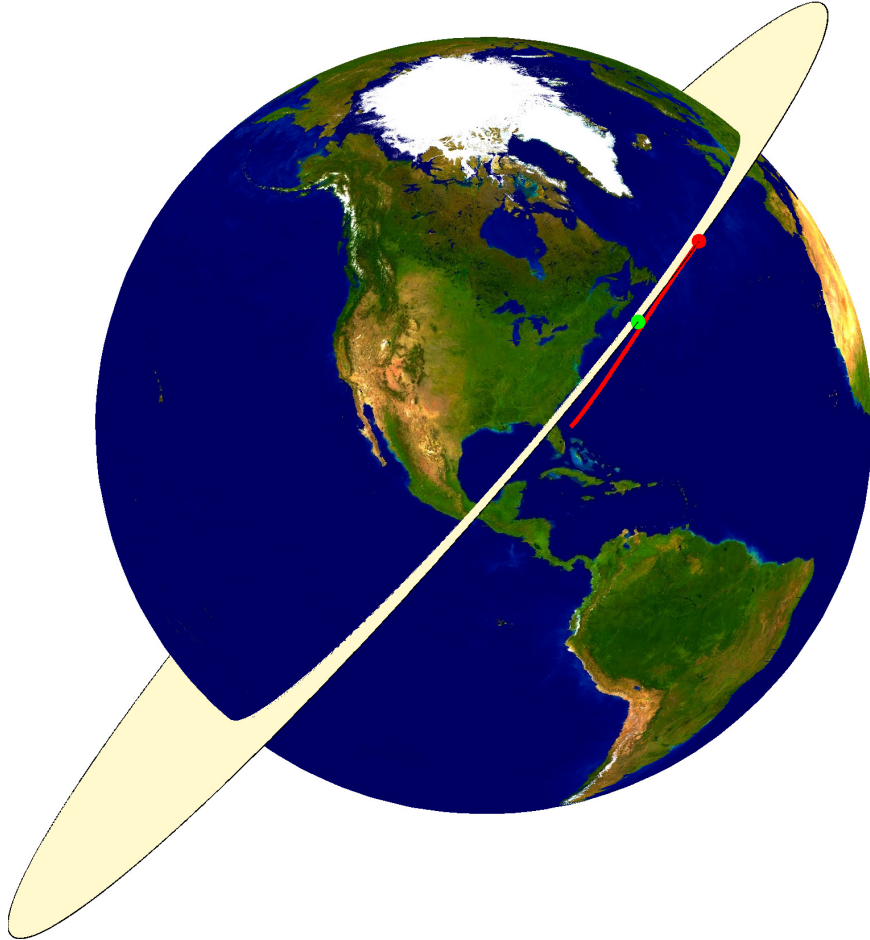
Figure 24: View 1: AMS closed-loop ascent trajectory and target insertion orbit for case 25 illustrating large out of plane motion (orbit shading for visual convenience)
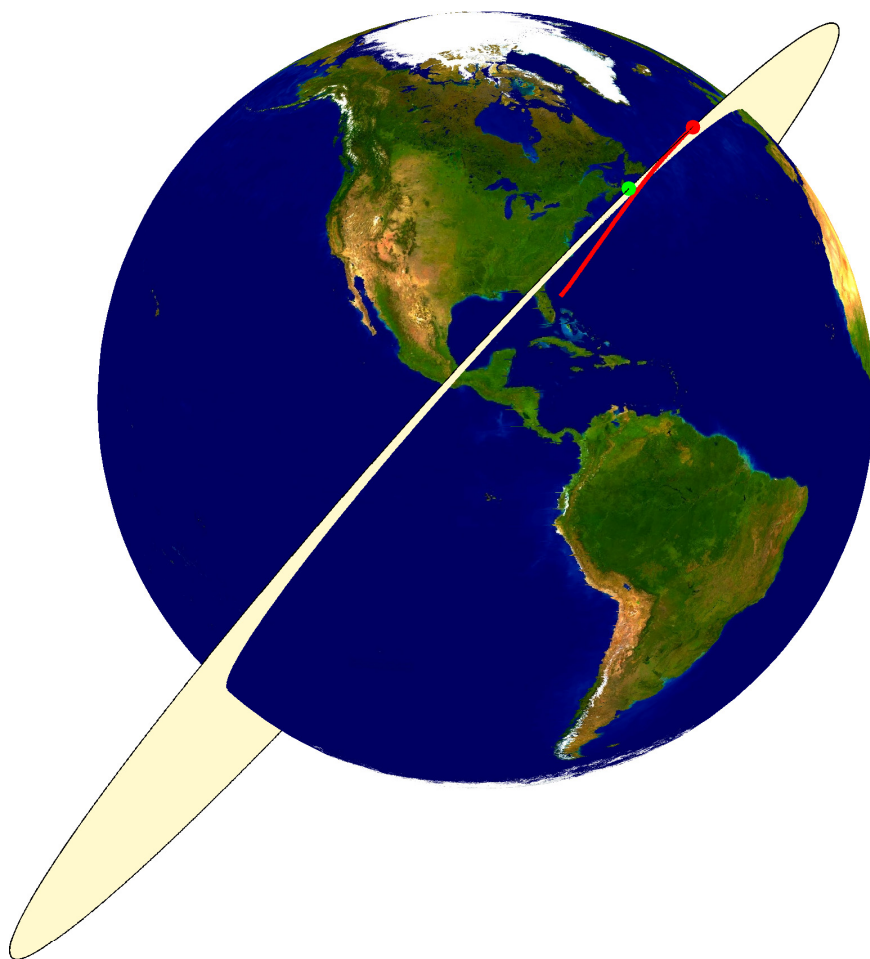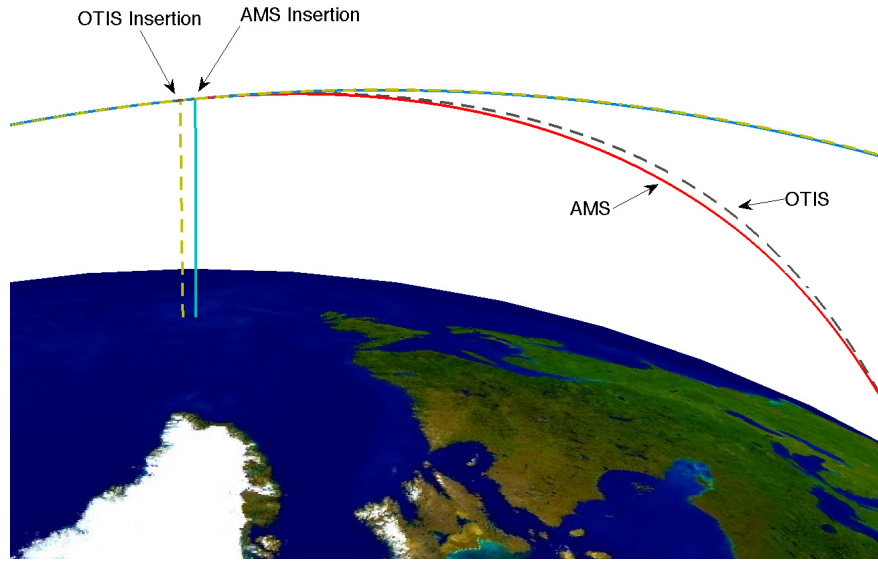
Figure 25: View 2: AMS closed-loop ascent trajectory and target insertion orbit for case 25 illustrating large out of plane motion (orbit shading for visual convenience)

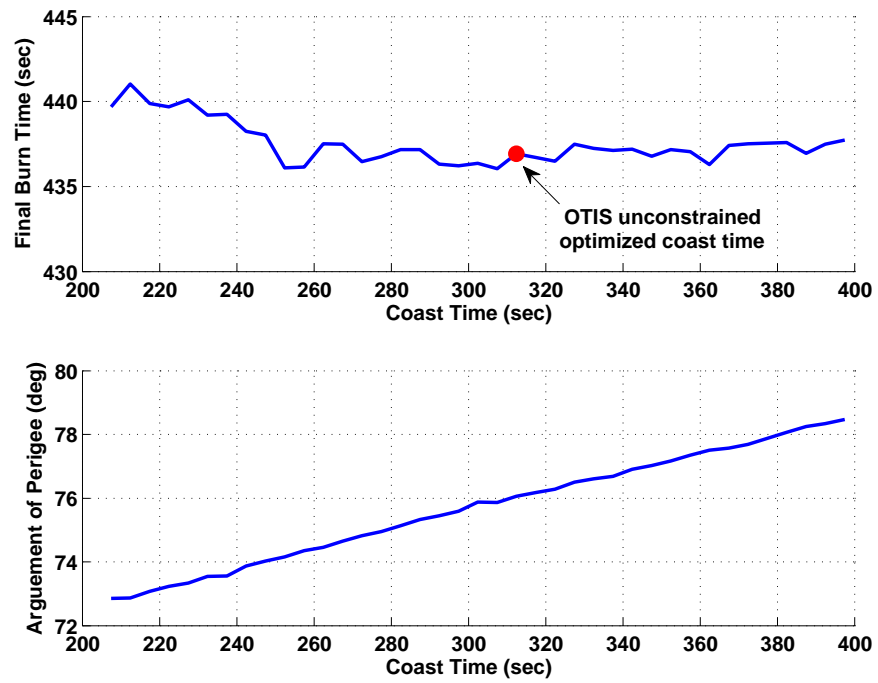Figure 26: AMS closed-loop and OTIS ascent trajectories and orbital insertion perigee direction for case 33

Figure 27: OTIS coast time sweep for case 33

11.4 Mode 46 Results

Mode 46 involves four insertion conditions defined by the desired final position magnitude r_f^*, velocity magnitude V_f^*, inclination i^*, and flight path angle γ_f^*. This Mode is unlike the others in that it is not defined from typical orbital elements and the conditions need not represent values on any target orbit. Rather, this Mode provides the ability to define a desired launch abort energy condition where, if met, the launch vehicle can glide unpowered if necessary to a determined landing site. Conditions for three cases are listed in table 12.

Table 12: Mode 46 Target Orbits

Case	Mode	altitude (km)	velocity (m/s)	i (deg)	γ_f (deg)
39	46	122	7500	51.6	-1
40	46	122	7500	51.6	-2
41	46	100	7000	40	-1

The results for these three cases are listed in table 13. All methods agree closely, both in optimized coast length and final burn time, however the OTIS trajectories have somewhat lager second burn times resulting in reduced final mass. The initial conditions used for these cases are the same as all previous cases and are conditions taken from a typical ascent. This results in a higher initial altitude than would most likely be experienced in an abort scenario, thus increasing the convergence difficulty. Figure 28 shows both the AMS and OTIS altitude and velocity profiles as well as the flight path angle time histories for case 40.

Table 13: Mode 46 Results

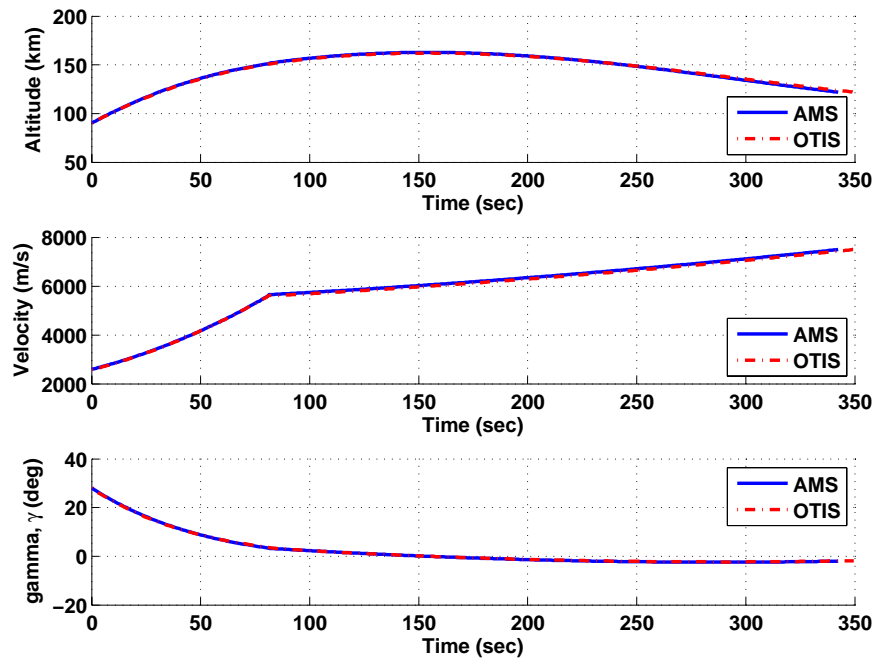| Case	Method	Coast (sec)	2nd Burn (sec)	Final Mass (kg)
39	OTIS	0.9908	272.5345	2978.1001
	AMS	0.0000	267.9072	3018.4401
	AMS closed-loop	0.1315	265.6799	3035.7000
40	OTIS	0.3931	267.7783	3021.1169
	AMS	0.1763	263.2835	3060.2844
	AMS closed-loop	0.0392	260.8845	3080.9500
41	OTIS	0.9037	226.0943	3398.1224
	AMS	0.0007	222.9545	3425.2613
	AMS closed-loop	0.0318	221.4846	3433.9000

Figure 28: AMS and OTIS altitude, velocity, and flight path angle profile comparison for case 40

12

Evaluating the Complete Ascent Guidance Algorithm

In this part the endo-atmospheric and exo-atmospheric ascent guidance algorithms are combined to generate complete optimal ascent trajectories and guide the vehicle from liftoff to orbital insertion. To demonstrate the applicability of the algorithms to both winged launch vehicles and conventional axisymmetric launch vehicles, a two-stage winged fully reusable launch vehicle model and the Ares I Crew Launch Vehicle (CLV) currently under development by NASA are used. The launch site is at KSC. For testing purposes 114 different wind profile pairs are used which are based on measurement data at KSC in February. These wind profiles are generated by the Natural Environments Branch at NASA Marshall Space Flight Center. Each profile provides altitude-dependent wind speed and direction. The first of each pair is a smoothed (filtered) profile of measured wind data; the second is unfiltered and measured on average 2 hours later. The smoothed profile in each pair is used in the guidance solution, and the unfiltered profile is used in simulation of the trajectory. In Monte Carlo simulations the wind pair is uniformly randomly selected for a trajectory to simulate the "day-of-launch wind". In addition, various environmental and vehicle modeling uncertainties are added in the simulations. But no navigation dispersions are considered in the simulations. In each simulation, the guidance is given only the nominal models of the vehicle and atmosphere, and the smoothed (and two-hour earlier) profile of the randomly selected "day-of-launch" wind profile. No additional guidance I-loads are adjusted from one trajectory to another, and no pre-launch guidance computation or update is performed.

12.1 Application to Two-Stage Winged Reusable Launch Vehicle

The vehicle is a two-stage winged fully reusable launch vehicle similar to what is shown in Fig. 29. The first stage has 4 engines, and second stage has one. Some of the basic data for the vehicle are given in Table 14.

The target orbit data are given in Table 15. No other inequality trajectory constraints are enforced. In addition to the randomly selected winds, other dispersions used in the Monte Carlo simulations are summarized in Table 16.

Figure 29: Two-stage winged fully reusable launch vehicle

Table 14: Vehicle data of the two-stage reusable launch vehicle

Parameter	First Stage	Second Stage
Vacuum thrust	$4 \times 2,086,883$ N	990,280.0 N
I_{sp}	335.0 sec	350.0 sec
Initial mass	574,023 kg	93,725kg
Empty mass	96,807.3 kg	17,190.8 kg
Propellant mass	382,671.0 kg	76,534.0 kg

The dispersions listed in Table 16 are some of the representative dispersions commonly used in launch simulations. The main objective in this section is to evaluate the robustness of the ascent guidance algorithm in the inevitable presence of winds and these appreciable dispersions. For the algorithm to qualify to be considered for on-board applications, it must be able to ensure convergence in the face of such dispersions without any knowledge of them. Also to be demonstrated is the potential for automated closed-loop ascent guidance without any case-dependent guidance I-load update, which is a key requirement for responsive launch, by showing that the algorithm can correctly guide the vehicle to the desired orbit in every simulation by simply "pushing the ignition button".

A total of 200 Monte Carlo simulations are shown in Figs. 30–36. Figures 30 and 31

Table 15: Target orbit for the 2-stage RLV (launch from KSC)

Orbit Parameter	i (deg)	e	altitude (km)	ascending node (deg)
Value	49.1	0.0	200.0	-107.5

Table 16: Dispersions used in Monte Carlo simulations for the two-stage RLV (all Gaussian distributions)

Parameter	Dispersion Mean	one-sigma value
Liftoff mass	5,740,234.5 kg	1,912.2 kg
Mass at first stage burnout	202,379.1 kg	674.5 kg
Mass flow rate for first stage	-2,547.6 kg/sec	8.5 kg/sec
Vacuum thrust for first stage	834,711.6 N	2,3803.5 N
Mass flow rate for second stage	-289.2 kg/sec	0.96 kg/sec
Thrust for second stage	990,280.0 N	2,823.8 N
Scaling factor for dispersions in aero coefficient C_A	0.0	0.0333333
Scaling factor for dispersions in aero coefficient C_N	0.0	0.0333333

depict the geodetic altitude and inertial velocity along these dispersed trajectories. From the figures it is evident that all the trajectories reach the specified orbit successfully, even though we will leave the examination of the actual orbital insertion statistics to the next section. The profiles of angle of attack profiles are plotted in Fig. 32. The initial large variations of α are caused by the fact the earth-relative velocity is very small right after liftoff. Any winds will cause large changes in the direction of the relative velocity. The vehicle flies a heads-up configuration so after liftoff α is largely positive in endo-atmospheric ascent portion. The pitch and yaw angle profiles of the vehicle with respect to the NDE frame are illustrated in Figs. 33 and 34. Finally the variations of the dynamic pressure q and the product $\alpha - q$ are shown in Figs. 35 and 36. Note that since neither is constrained, they reached quite large values, especially for αq.
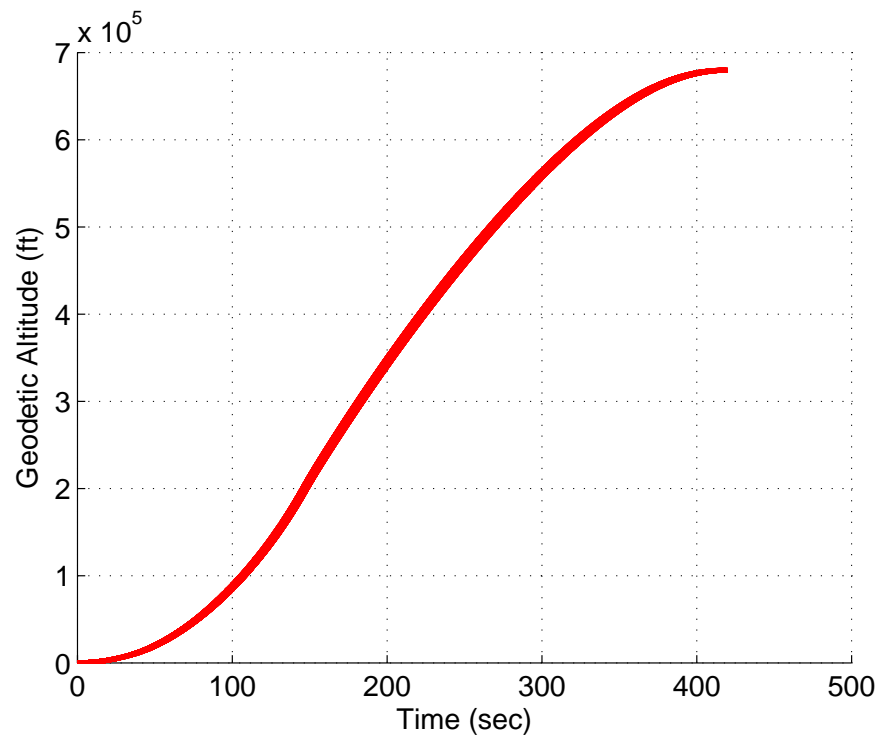
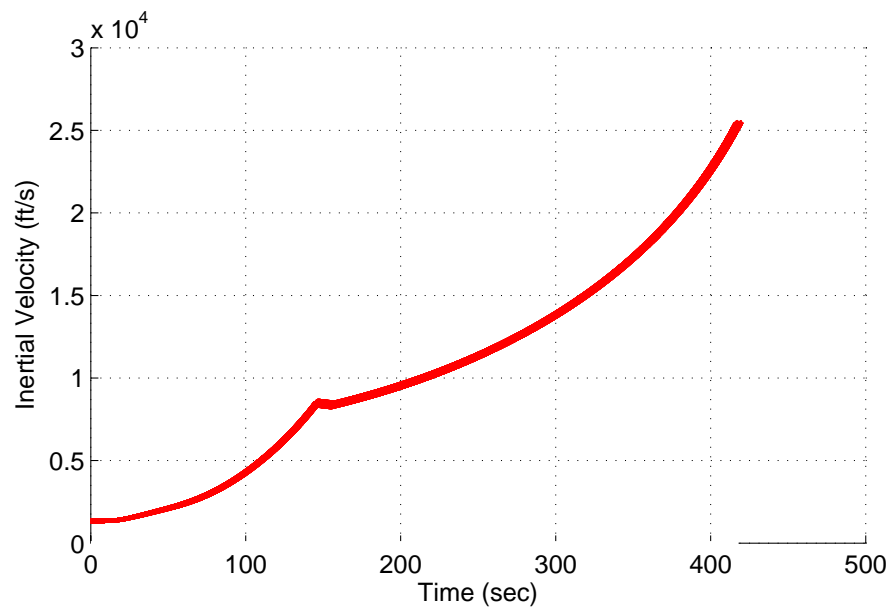Figure 30: Geodetic altitude profiles along 200 dispersed RLV ascent trajectories

Figure 31: Inertial velocity profiles along 200 dispersed RLV ascent trajectories
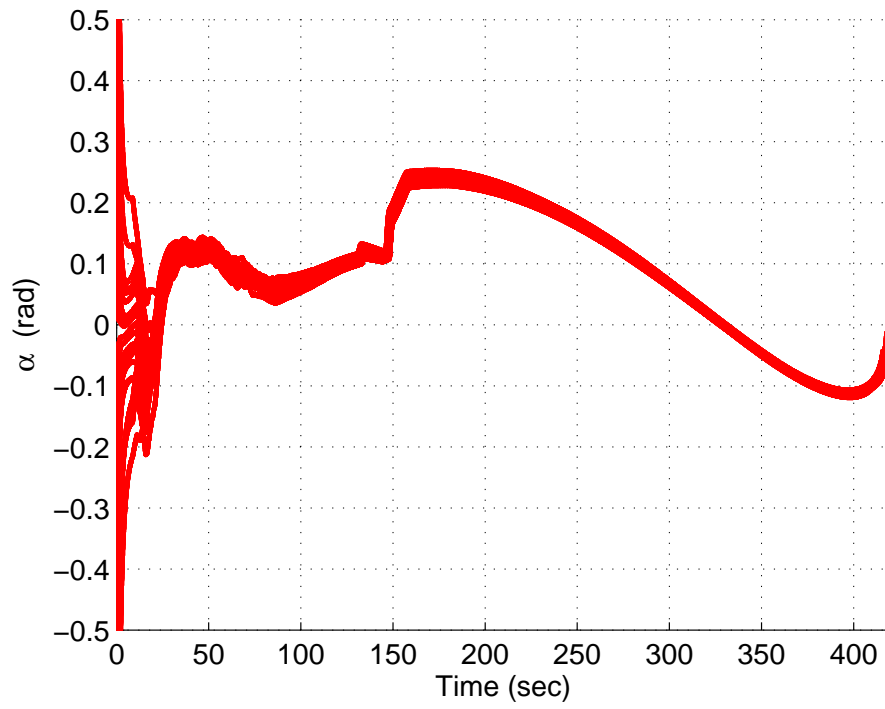
Figure 32: Anlgle of attack profiles along 200 dispersed RLV ascent trajectories
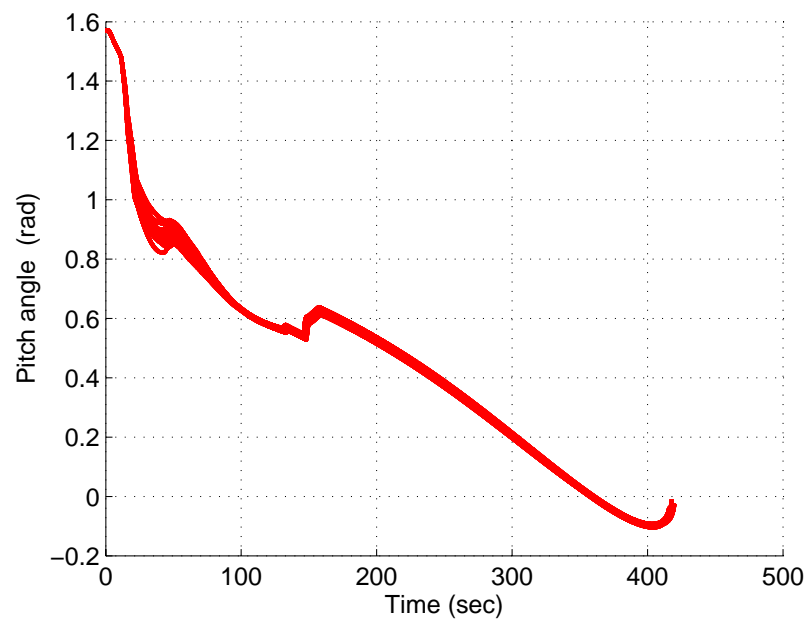

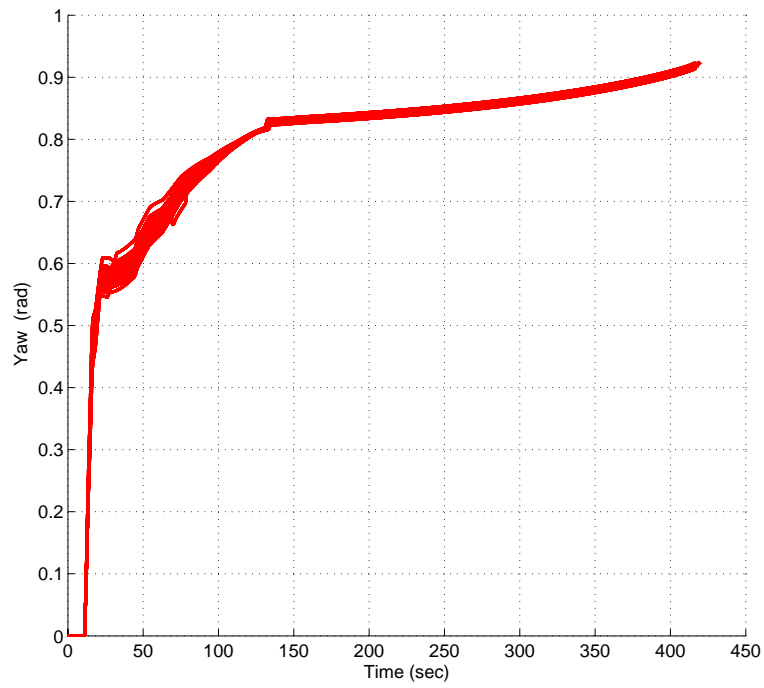Figure 33: Pitch angle profiles along 200 dispersed RLV ascent trajectories

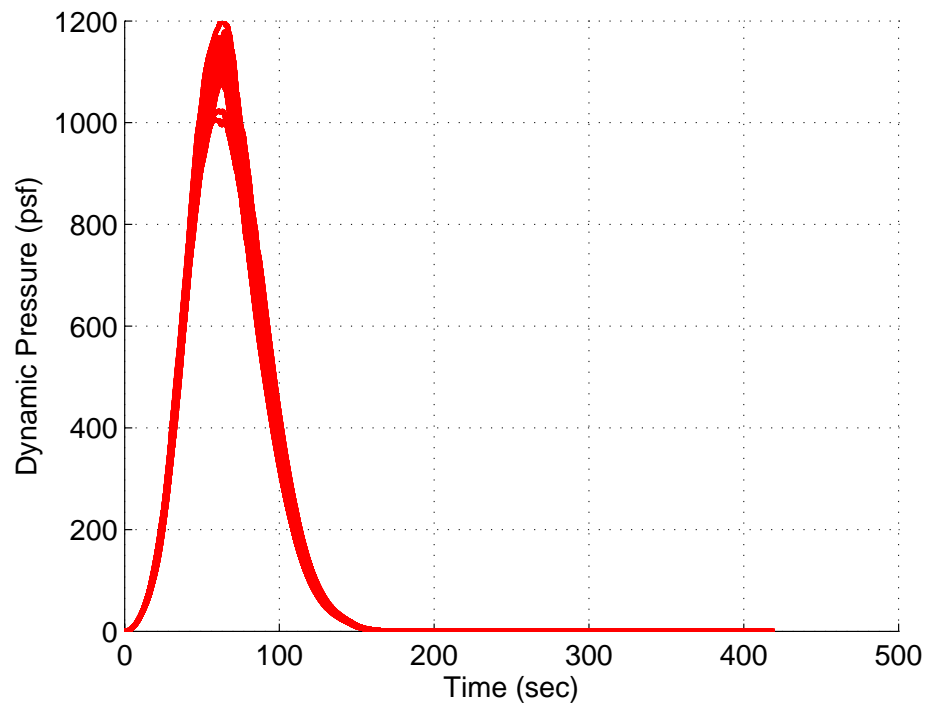Figure 34: Yaw angle profiles along 200 dispersed RLV ascent trajectories

Figure 35: Dynamic pressure profiles along 200 dispersed RLV ascent trajectories
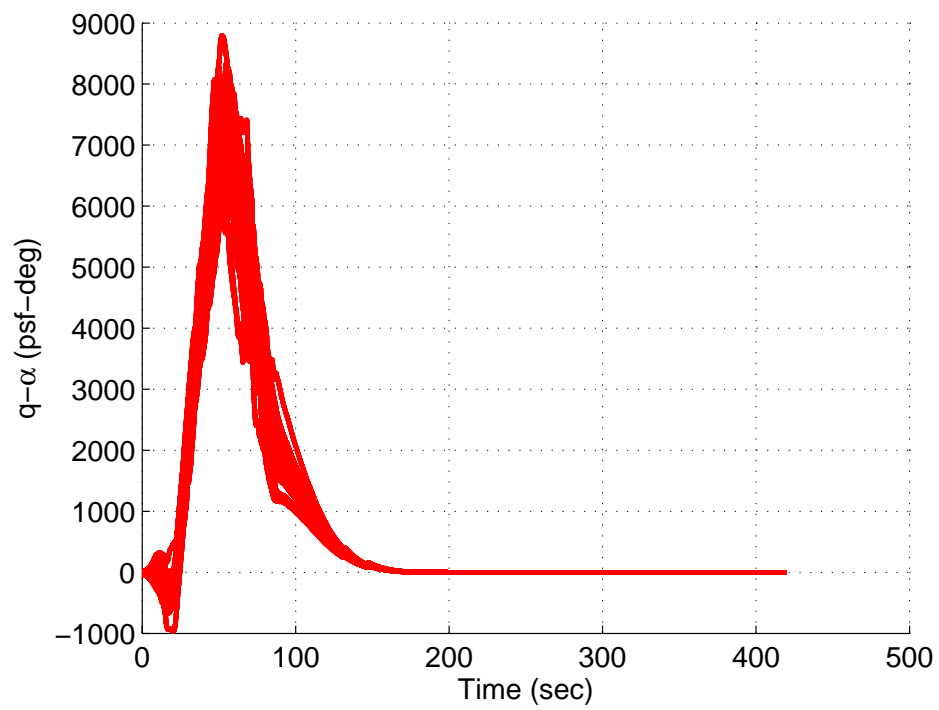
90

Figure 36: Dynamic pressure profiles along 200 dispersed RLV ascent trajectories

12.2 Application to Ares I Crew Launch Vehicle

12.2.1 The Ares I CLV

The Ares I CLV is a two-stage vehicle currently under development that will carry the Orion Crew Exploration Vehicle (CEV) to the International Space Station (ISS). Figure 37 shows its conventional, axisymmetric configuration. The first stage of the Ares I vehicle is a five-segment solid rocket booster (SRB) derived from the Shuttle Solid Rocket Booster (SRB). The vacuum thrust profile and mass flow rate of the SRB have a quite strong dependence on time since ignition, and cannot be approximated by constants, as seen in Figs. 38 and 39. The second stage engine is a Saturn J-2 derived liquid engine, dubbed J-2X. Its thrust and mass flow rate are treated as constants in guidance. Other vehicle parameters are given in Table 17. The aerodynamic coefficients of the vehicle used for guidance solution are smooth curve fittings to tabulated data as functions of Mach number and angle of attack. The vehicle's gross liftoff weight is on the order of 2 million lbs with a payload capacity of 25 metric tons.

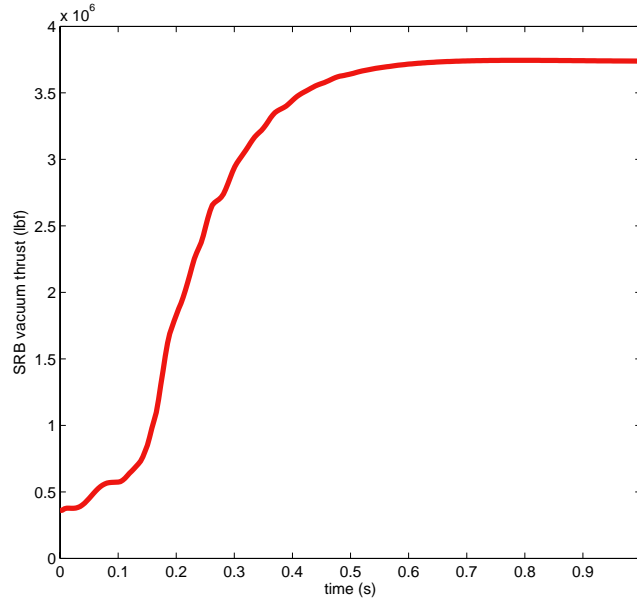Figure 37: The Ares I Crew Launch Vehicle

Figure 38: The vacuum thrust profile of the Solid Rocket Booster

Table 17: Vehicle data for the Ares I CLV

Parameter	First Stage	Second Stage
Vacuum thrust	13,964 kN at 0.7 sec	2,088 kN
Vacuum I_{sp}	268.8 sec	452.1 sec
Initial mass	586,344 kg	93,725 kg
Empty mass	81,818 kg	20,422 kg
Propellant mass	504,516 kg	163,530 kg

The International Space Station (ISS) mission target orbit for Ares I is a -11×100 nm orbit (with an eccentricity of 0.0159) at the inclination of 51.6 degrees. The insertion altitude into this orbit is specified at 70 nm. The CEV will use its own propulsion to reach the ISS orbit after separating from Ares I. The orbital insertion conditions are summarized in the Table below

Table 18: Ares I orbital insertion condition for ISS mission (launch from KSC)

Orbit Parameter	i (deg)	e	altitude (nm)	γ (deg)
Value	51.6	0.0159	70.0	0.8091

where γ is the inertial flight path angle at orbital insertion.

On the launch pad at the Kennedy Space Center (KSC), the Ares I is positioned with crew window facing due east. It will take about 6 seconds for the vehicle to vertically ascend to clear the tower, so at 6 seconds from liftoff, the vehicle begins to maneuver toward gravity turn. At $t_2 = 20$ seconds from liftoff, the vehicle enters near gravity turn. The closed-loop
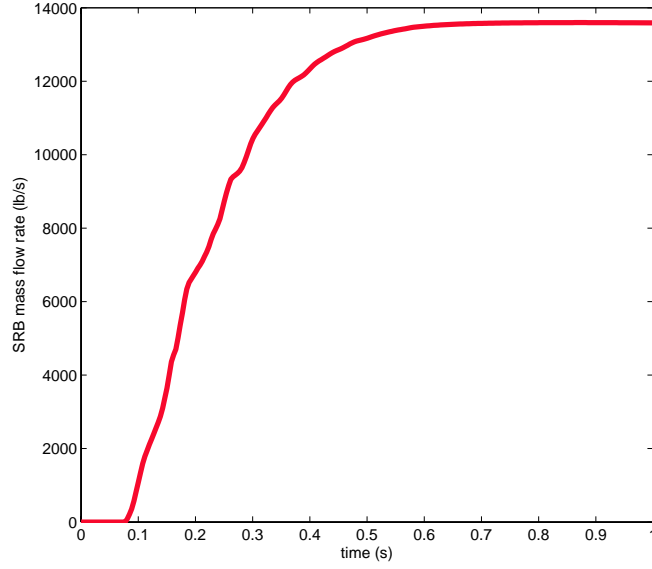
Figure 39: The vacuum mass rate profile of the Solid Rocket Booster

guidance update rate is 1 HZ while the trajectory simulation is performed at 100 HZ. For nominal mission design (no wind) a constraint of

$$\alpha_t q \leq 500 \quad \text{(psf-deg)} \tag{1}$$

is imposed, where α_t is the total angle of attack, the angle between the wind-relative velocity and the longitudinal body axis of Ares I. In the presence of winds and other dispersions, the guidance is required to maintain the constraint

$$\alpha_t q \leq 3000 \quad \text{(psf-deg)} \tag{2}$$

This constraint is critically important for Ares I because of its long slender configuration (about 200 m in length). For the structural integrity of Ares I during the ascent through the atmosphere, the bending moment due to aerodynamic forces must be kept within design bounds. The quantity $\alpha_t q$ is direct measure of the aerodynamic bending moment.

In addition to the dispersions listed in Table 19, altitude-dependent atmospheric density and pressure dispersions from the values from the 1976 US Standard Atmosphere are generated from an in-house model and used in the simulations (which are unknown to the guidance). The model can produce randomized atmospheric dispersions based on location, altitude, and season. While much simpler than NASA's GRAM-2007 atmospheric model in Ref. 40, this model produces quantitatively similar atmospheric dispersions as those by GRAM-2007.

12.2.2 Nominal Mission

All the results presented here are from closed-loop 3DOF simulations. First the nominal ascent without wind and other dispersions added is examined. Two cases are compared. One

Table 19: Dispersions used in Monte Carlo simulations for the Ares I CLV (Gaussian distributions unless indicated otherwise)

Parameter	Dispersion Mean	one-sigma value
Dispersion scaling factor for mass flow rate for SRB	0.0	0.3333%
Dispersion scaling factor for vacuum thrust for SRB	0.0	0.3333%
Dispersion scaling factor for vacuum thrust for J2-X	0.0	0.2667%
J2-X specific impulse	452.1 sec	0.73333 sec
Mass flow rate for J2-X	see above	see above
Scaling factor for dispersions in aero coefficient C_A	N/A	$\pm 1\%$
Scaling factor for dispersions in aero coefficient C_N	N/A	$\pm 1\%$

*The dispersion scaling factors for C_A and C_N are in uniform distributions within $\pm 1\%$.

is fully constrained, subject to (1). The other is freely optimized after the vertical ascent at $t_1 = 6$ sec, without any additional load or path inequality constraints. Figure 40 shows the angle of attack profiles for the two trajectories. The solid line is for the constrained trajectory. It can seen that the α profile is qualitatively very similar to that of the α in Ref. citeDukeman2 which is optimized off-line and essentially the same as the result obtained from POST.[42] On the other hand, the unconstrained optimal trajectory flies an α of approximately 5 degrees (about 10 times that of the constrained one). The corresponding $\alpha_t q$ and dynamic pressure q during the first stage are plotted in Fig. 41. It is seen that the unconstrained trajectory experiences a peak $\alpha_t q$ of 6000 psf-deg, 12 times that along the constrained trajectory. The penalty for flying this highly constrained trajectory is about 0.9% less of mass delivered, which amounts to 430 kg. This is quite remarkable, considering the severity of the constraint. This achievement demonstrates the effectiveness of the guidance optimization in the short period of $[t_1, \ t_2] = [6, 20]$. Without these initial maneuvers properly optimized, one could easily end up with the constrained trajectory suffering up to $15\% - 20\%$ performance penalty. Figure 42 shows the comparison of the Euler angles of the vehicle's body axes during the ascent. These angles are with respect to the North-East-Down (NED) coordinate system at the launch site, in the standard yaw-pitch-roll rotation sequence. Not surprisingly, the optimal yaw angle found is practically constant and only about 2.5 degrees different from the usual launch azimuth

$$\psi_{az} = \sin^{-1}\left(\frac{\cos i}{\cos \phi_c}\right)$$

where i is the target orbit inclination and ϕ_c the geocentric latitude of the launch site. Figure 11 illustrates the altitude and velocity profiles of the nominal ascent with and without the $\alpha_t q$ constraint (1).

12.2.3 Monte Carlo Simulations

Next, 500 dispersed trajectories are simulated with the dispersions and randomly selected KSC winds described earlier. In each simulation, the guidance is given only the nominal models of the vehicle and atmosphere, and the smoothed (and two-hour earlier) profile of the randomly selected "day-of-launch" wind profile. No additional guidance I-loads are
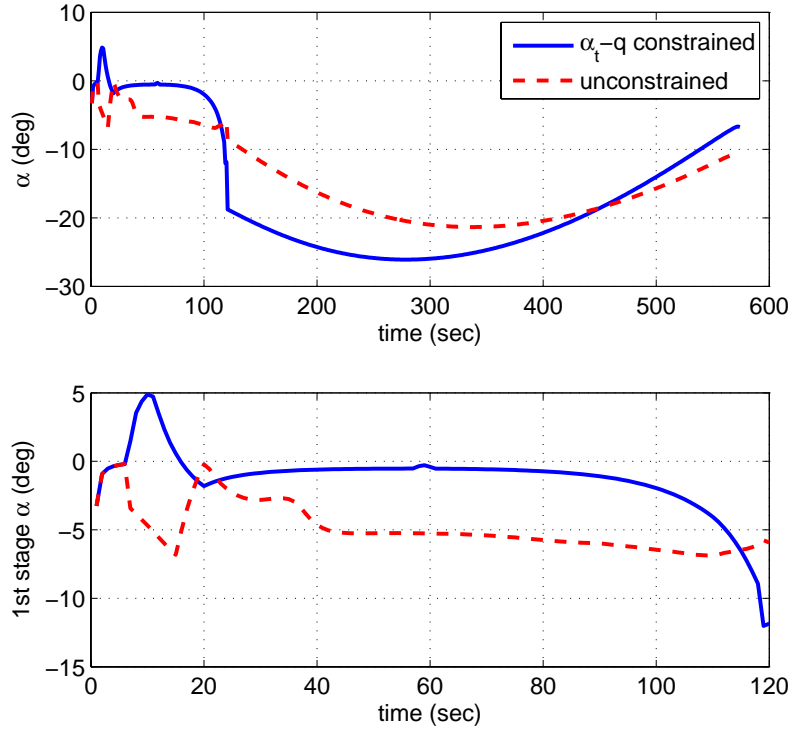
Figure 40: Angle of attack along nominal Ares I optimal ascent trajectories: top figure: the complete α profile (stage 1 and 2); bottom figure: α for the first stage

adjusted from one trajectory to another, and no pre-launch guidance computation or update is performed. Upon ignition, the CLV rieses for 6 seconds to clear off the launch tower. At this instant, the optimal closed-loop guidance described in this report takes over and steers the vehicle through the separation of the SRB, firing of the J2-X to the orbital insertion.

The statistics on the final (orbital insertion) conditions are listed in Table 20. Also included in the Table 20 are the statistics of the peak values of $\alpha_t q$ along all these trajectories. The data in the table clearly demonstrate accurate orbital insertion conditions and quite consistent performance in terms of injected mass. Figure 44, in which the geodetic altitude, inertial velocity and inertial flight path angle along the 500 dispersed trajectories are plotted, confirms the successful orbital insertion in all cases. The high accuracy of the orbital insertion conditions seen in the Table suggests that if navigation errors are included, the orbital insertion errors will be on the same order as that of the navigation errors. This high accuracy, though, should be viewed in the context that no effects of the uncertainty caused by "tailoff thrust" of the J2-X engine are included when it is commanded to shut off. Such an uncertainty can cause, for instance, the error of a few nautical miles in semi-major axis of the final orbit. Again, one of the most critical concerns during atmopheric ascent is the bending moment in the presence of the winds. The first subplot of Fig. 45 shows that the closed-loop guidance strategy is able to keep the angle of attack small throughout the flight of the first stage. The statistics on peak $\alpha_t q$ are reassuring in that the highest value is about
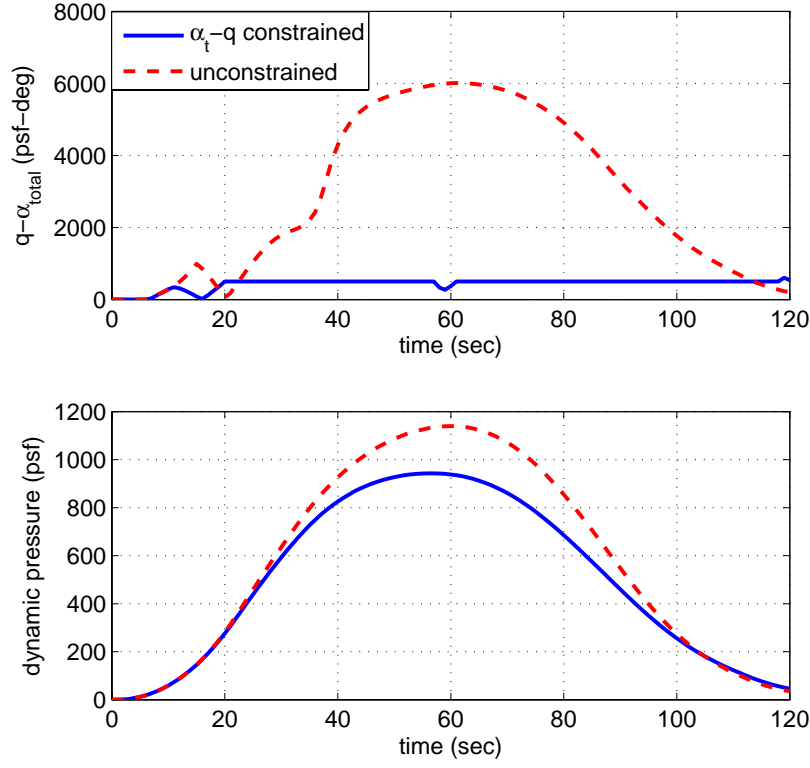
96

Figure 41: α_t-$\bar{q}$ and dynamic pressure $\bar{q}$ along the nominal Ares I optimal ascent trajectories of the first stage

2800 psf-deg, below the desired level of 3000 psf-deg. In fact, the data suggest that the 3-sigma value of the peak $\alpha_t q$ is at about 2300 psf-deg. A closer examination of the data reveals that the peak value of 2800 psf-deg occurred in only two trajectories, both with the same wind profile. This is a case when the wind is relatively strong and the measured wind data used by the guidance differs considerably from the wind encountered in ascent. The second subplot in Fig. 45 clearly shows the same conclusion.

The Euler angles (pitch, yaw and roll) of the vehicle body axes with respect to the launch NED frame during the endo-atmospheric ascent portion (which lasts about 120 seconds) along the 500 trajectories are depicted in Fig. 46. The complete pitch and yaw angle for both stages of the Ares I in all the dispersed trajectories are plotted in Fig. 47. Note that the roll angle in exo-atmospheric flight is immaterial because it does not affect the direction of the thrust vector(thus roll angle is not shown in Fig. 47), whereas in endo-atmospheric flight the roll angle affects the sidelslip angle, hence the total angle of attack α_t.
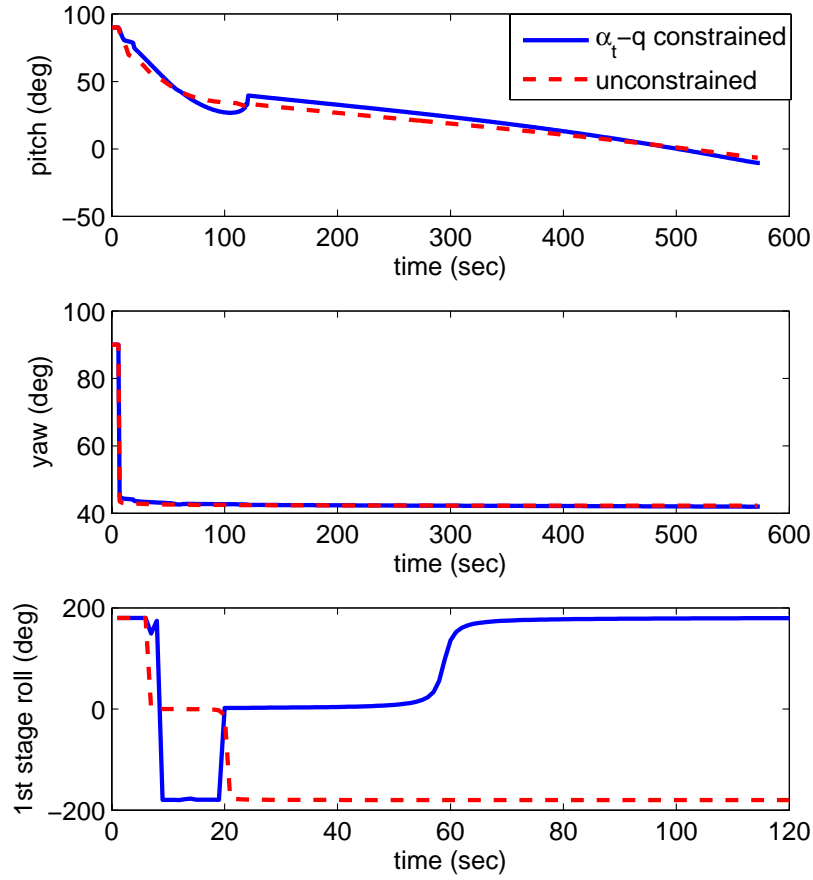
Figure 42: Euler angles along nominal Ares I optimal ascent trajectories

Table 20: Statistics of 500 dispersed trajectories: orbital insertion conditions and peak $\alpha_t q$ (where $a=$ semi-major axis, $e=$eccentricity)

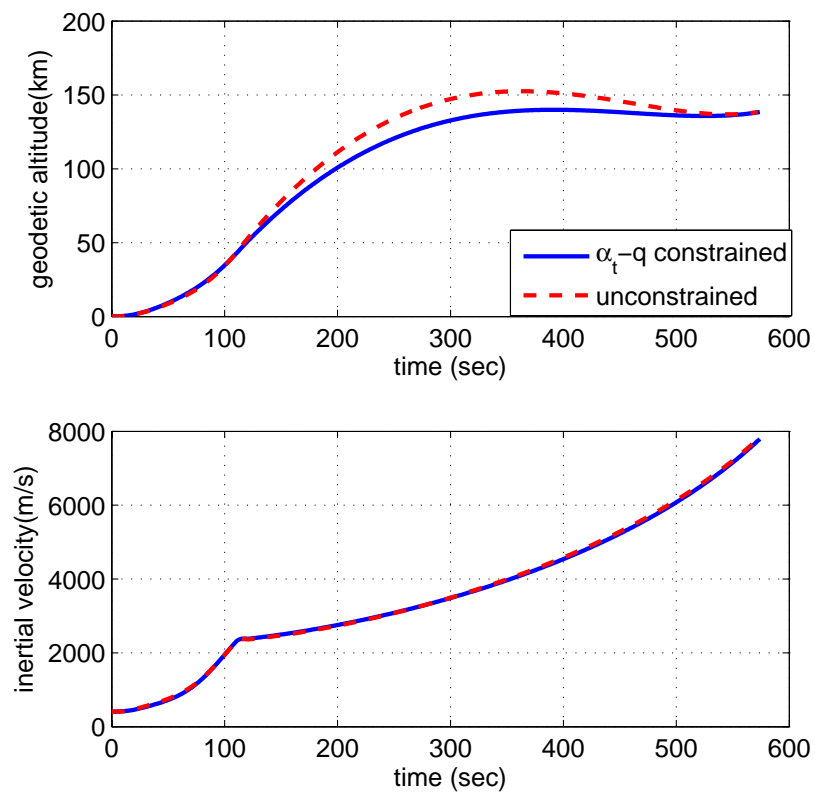|	mean	std. deviation	maximum	minimum
r_f (m)	6,507,775.52	0.56	6,507,776.95	6,507,773.02
V_f (m/s)	7,797.74	0.10	7,798.02271	7797.34
γ_f (deg)	0.8089	0.0061	0.82364	0.7832
i (deg)	51.60001	0.00001	51.60007	51.59994
a (m)	6,460,810.91	165.29	6,461,273.58	6,460,149.90
e	0.01588	0.0001	0.01611	0.01549
m_f (kg)	45,827.58	336.45	46,588.25	44,490.092
peak $\alpha_t q$ (psf-deg)	1,362.44	327.91	2,827.64	705.82

Figure 43: Altitude and velocity along nominal Ares I optimal ascent trajectories
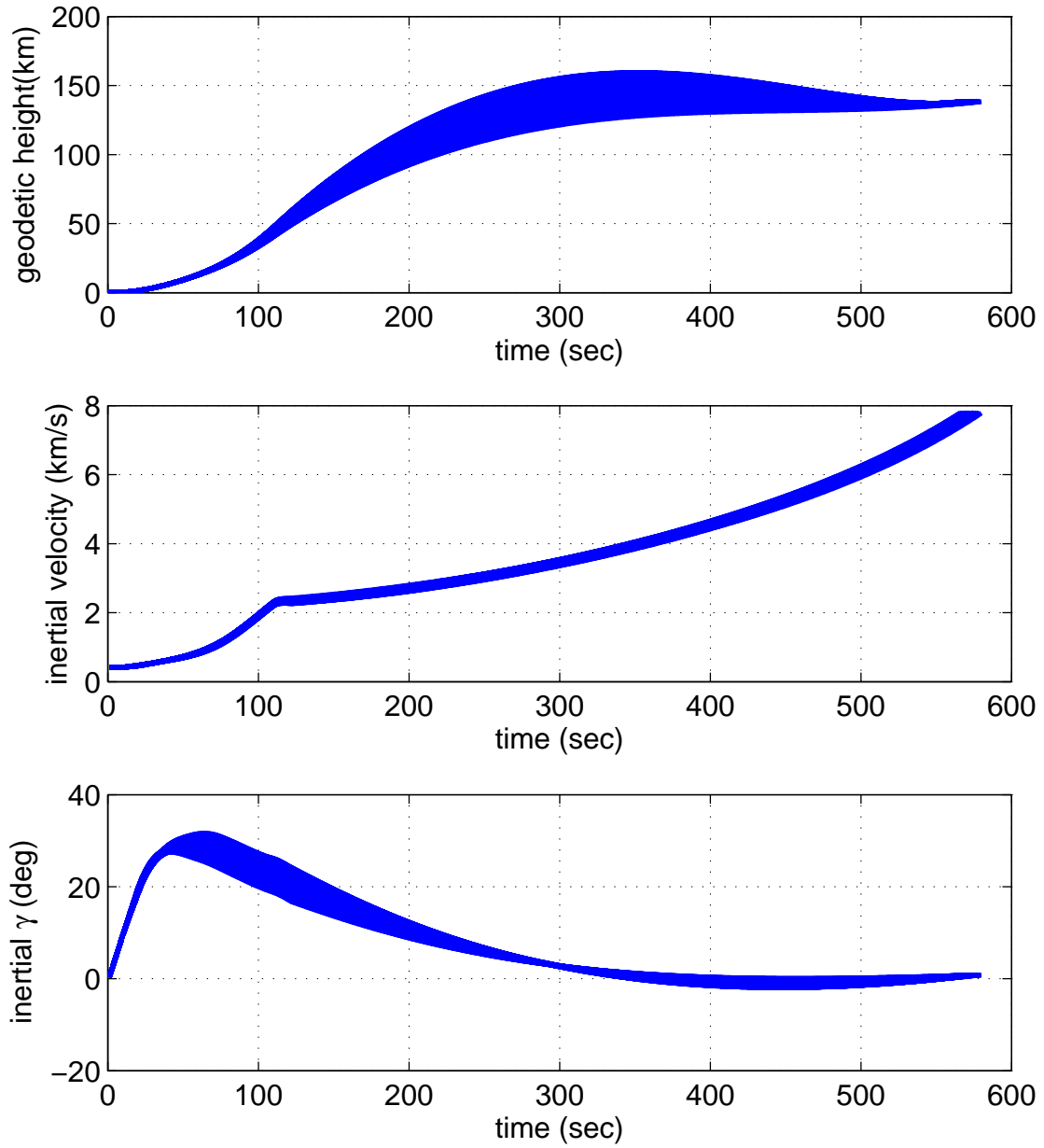
Figure 44: Geodetic altitude, inertial velocity and inertial flight path angle along 500 dispersed ascent trajectories of Ares I
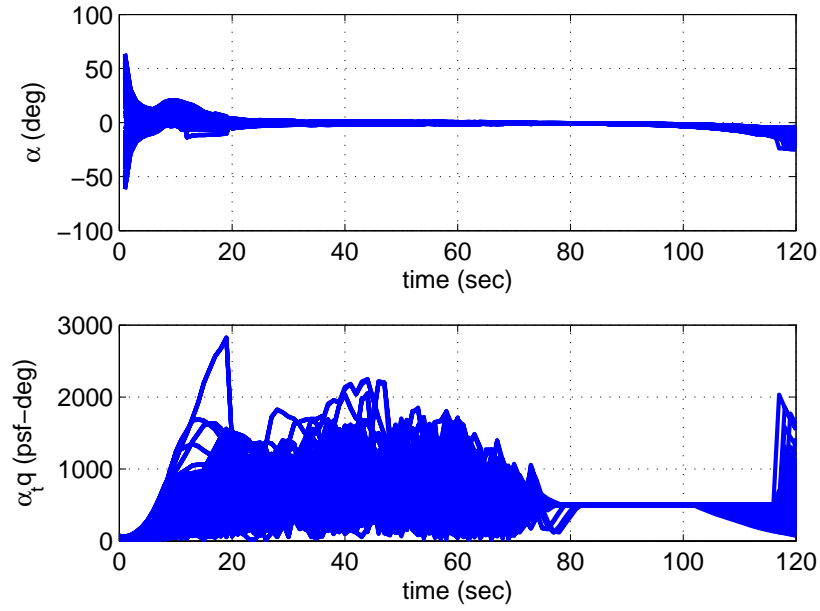
Figure 45: Variations of first-stage α and $\alpha_t q$ along 500 dispersed ascent trajectories of Ares I
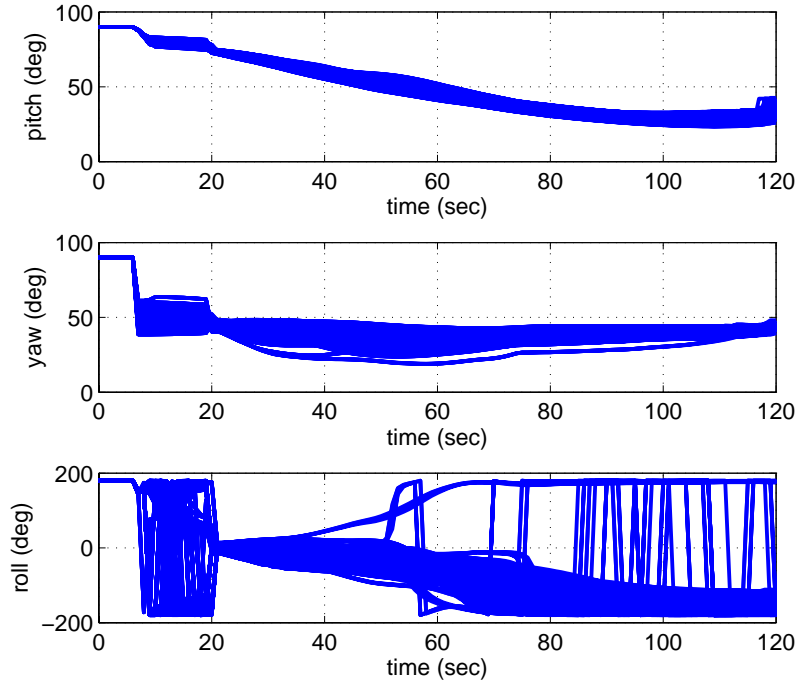

Figure 46: Variations of first-stage Euler angles along 500 dispersed ascent trajectories of Ares I
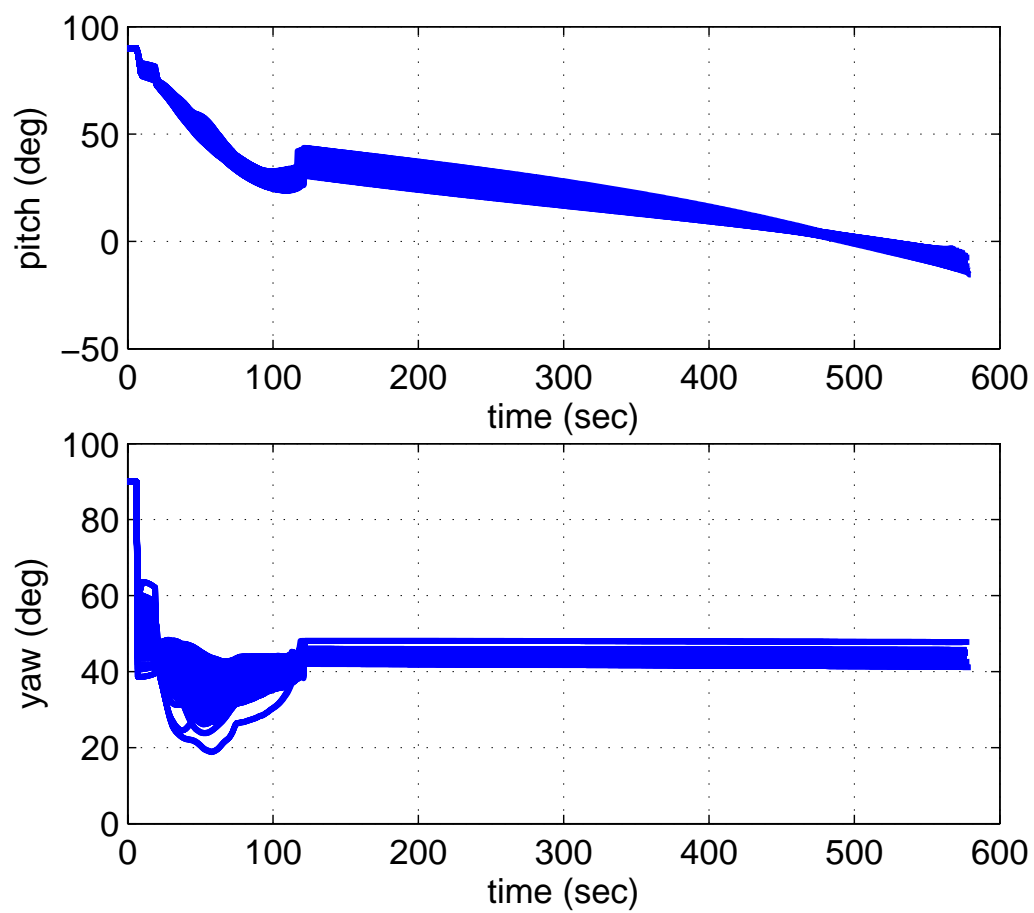
Figure 47: Variations of pitch and yaw angles (of both stages) along 500 dispersed ascent trajectories of Ares I

Appendix A

Costate Equations for 3D Endo-Atmospheric Optimal Ascent

The notation used in the following is the same as defined in Sections in Part **??** of this report. Let $\rho_r = \partial\rho/\partial r$, $T_r = \partial T/\partial r$, $C_\rho = \rho_0\rho S_{ref}R_0/m(t)$, and

$$
\begin{aligned}
A_{\rho r} &= \frac{V_r^2 S_{ref} R_0 \rho_0 C_A \rho_r}{2m(t)}, \ \ N_{\rho r} = \frac{V_r^2 S_{ref} R_0 \rho_0 C_N \rho_r}{2m(t)}, \\
C_{A_\alpha} &= \partial C_A/\partial\alpha, \ \ C_{N_\alpha} = \partial C_N/\partial\alpha, \\
C_{A_{Mach}} &= \partial C_A/\partial\text{Mach}, \ \ C_{N_{Mach}} = \partial C_N/\partial\text{Mach}, \\
a_{pvb} &= \boldsymbol{p}_V^T \boldsymbol{1}_b = p_V \cos(\Phi - \alpha), \ \ a_{pvn} = \boldsymbol{p}_V^T \boldsymbol{1}_n = p_V \sin(\Phi - \alpha)
\end{aligned}
$$

Denote the altitude-dependent speed of sound by $V_s(r)$. The complete costate equations (22) and (23), after much vector differentiation and simplification, are given by

$$
\begin{aligned}
\boldsymbol{p}_r' &= \frac{1}{r^3}\boldsymbol{p}_V - \left[\frac{3a_{pvb}}{r^4} + a_{pvb}\left(T_r - A_{\rho r} + \frac{1}{2V_r}C_\rho V_s^2 C_{A_{Mach}}\frac{\partial V_s}{\partial r}\right)\right. \\
&\quad + \left. a_{pvn}\left(N_{\rho r} - \frac{1}{2V_r}C_\rho V_s^2 C_{N_{Mach}}\frac{\partial V_s}{\partial r}\right)\right]\frac{\boldsymbol{r}}{r} \\
&\quad + C_\rho\bar{\omega}_E \times \left\{a_{pvb}\left[(C_A + \frac{1}{2V_r}V_s C_{A_{Mach}})\boldsymbol{V}_r + \frac{1}{2}C_{A_\alpha}V_r^2\frac{\partial\alpha}{\partial\boldsymbol{V}}\right]\right. \\
&\quad - \left. a_{pvn}\left[(C_N + \frac{1}{2V_r}V_s C_{N_{Mach}})\boldsymbol{V}_r + \frac{1}{2}C_{N_\alpha}V_r^2\frac{\partial\alpha}{\partial\boldsymbol{V}}\right]\right\} \quad (3) \\
\boldsymbol{p}_V' &= -\boldsymbol{p}_r + C_\rho\left[a_{pvb}(C_A + \frac{1}{2V_r}V_s C_{A_{Mach}}) - a_{pvn}(C_N + \frac{1}{2V_r}V_s C_{N_{Mach}})\right. \\
&\quad + \left.\frac{1}{2}(a_{pvb}C_{A_\alpha} - a_{pvn}C_{N_\alpha})\frac{\cos\alpha}{\sin\alpha}\right]\boldsymbol{V}_r - \frac{C_\rho V_r}{2\sin\alpha}\left(a_{pvb}C_{A_\alpha} - a_{pvn}C_{N_\alpha}\right)\boldsymbol{1}_b \quad (4)
\end{aligned}
$$

where from the first equation in Eq. (7) and $\boldsymbol{V}_r = \boldsymbol{V} - \bar{\omega}_E \times \boldsymbol{r} - \boldsymbol{V}_w$

$$
\frac{\partial\alpha}{\boldsymbol{V}} = \frac{1}{V_r\sin\alpha}(\cos\alpha\boldsymbol{1}_{V_r} - \boldsymbol{1}_b) \quad (5)
$$

Note that the costate equation (3) has been simplified by recognizing that

$$
(\boldsymbol{1}_b\boldsymbol{1}_b^T + \boldsymbol{1}_n\boldsymbol{1}_n^T - I_3)\boldsymbol{p}_V = 0 \quad (6)
$$

because $\boldsymbol{1}_b$, $\boldsymbol{1}_n$ and $\boldsymbol{p}_V$ are in the same plane in the optimal solution, and $\boldsymbol{1}_b$ and $\boldsymbol{1}_n$ are unit vectors that are orthogonal to each other.

Appendix B

Jacobians of Thrust Integrals

In the numerical solution of the burn-coast-burn problem in this report, the Jacobian of the constraint vector in Eq. (34) can be analytically obtained. While much of it just requires standard (and careful) vector differentiation, the most involved part is perhaps the Jacobians of the thrust integrals in Eqs. (16) and (17). This Appendix provides the key equations that are very useful in computing analytically these Jacobians. See Ref.[5] for some similar results. Consider the thrust integrals in an interval $[\tau_1, \tau_2]$:

$$\boldsymbol{I}_c(\tau_2, \tau_1) = \int_{\tau_1}^{\tau_2} \mathbf{1}_{p_V}(\zeta) \cos(\omega\zeta) A_T(\zeta) d\zeta \in R^3 \tag{7}$$

$$\boldsymbol{I}_s(\tau_2, \tau_1) = \int_{\tau_1}^{\tau_2} \mathbf{1}_{p_V}(\zeta) \sin(\omega\zeta) A_T(\zeta) d\zeta \in R^3 \tag{8}$$

Let $\boldsymbol{\lambda}_1 = col(\boldsymbol{p}_V(\tau_1), -\boldsymbol{p}_r(\tau_1)/\omega)$ be the initial costate vector in this interval, and h a step size parameter as follows

$$h = \frac{\tau_2 - \tau_1}{N}$$

where $N = 2$ for using the Simpson's rule to compute the above integrals and $N = 4$ for the Milne's rule. Define the following matrices for $i = 0, 1, \ldots, N$ in $R^{3 \times 6}$

$$\Lambda(ih) = \left[\cos(i\omega h) I_{3 \times 3} \ \sin(i\omega h) I_{3 \times 3} \right] \tag{9}$$

$$K(\tau_1 + ih) = \frac{1}{\|\boldsymbol{p}_V(\tau_1 + ih)\|} \left[I_{3 \times 3} - \mathbf{1}_{p_V}(\tau_1 + ih) \mathbf{1}_{p_V}^T(\tau_1 + ih) \right] \Lambda(ih) \tag{10}$$

Through the thrust direction $\mathbf{1}_{p_V}(\tau) = \boldsymbol{p}_V(\tau)/\|\boldsymbol{p}_V(\tau)\|$, both $\boldsymbol{I}_c$ and $\boldsymbol{I}_s$ are functions of $\boldsymbol{\lambda}_1$. When these integrals are evaluated by a numerical quadrature method, it can be shown that the Jacobians of $\boldsymbol{I}_c$ and $\boldsymbol{I}_s$ with respect to $\boldsymbol{\lambda}_1$ are given by

$$\frac{\partial \boldsymbol{I}_c(\tau_2, \tau_1)}{\partial \boldsymbol{\lambda}_1} = \frac{(\tau_2 - \tau_1)}{n_s} \sum_{i=0}^{N} b_i A_T(\tau_1 + ih) \cos(\tau_1 + i\omega h) K(\tau_1 + ih) \tag{11}$$

$$\frac{\partial \boldsymbol{I}_s(\tau_2, \tau_1)}{\partial \boldsymbol{\lambda}_1} = \frac{(\tau_2 - \tau_1)}{n_s} \sum_{i=0}^{N} b_i A_T(\tau_1 + ih) \sin(\tau_1 + i\omega h) K(\tau_1 + ih) \tag{12}$$

where, for the Milne's rule, we have

$$N = 4, \ n_s = 90, \ b_0 = 7, \ b_1 = 32, \ b_2 = 12, \ b_3 = 32, \ b_4 = 7$$

and for the Simpson's rule

$$N = 2, \ n_s = 6, \ b_0 = 1, \ b_1 = 4, \ b_2 = 1$$

Appendix C

Fixed-Point Approach for Endo-Atmospheric TPBVP

The Fixed-Point Problem

In Section 10, a special form of two-point-boundary-value problem (TPBVP) needs to be solved for optimal endo-atmospheric ascent. Define the state vector $\boldsymbol{x} = col(\boldsymbol{r}\ \boldsymbol{V})$ and costate vector $\boldsymbol{p} = col(\boldsymbol{p}_r\ \boldsymbol{p}_V)$. Once the the controls $\boldsymbol{1}_b$ (and $\boldsymbol{1}_n$) in right-hand sides of the state Eqs. (10), and costate Eqs. (22)–(23) are eliminated by the optimality conditions as functions of $\boldsymbol{x}$ and $\boldsymbol{p}$, the state and costate equations become homogeneous. The initial state $\boldsymbol{x}_0$ is given. Suppose that the burn out of the first stage of the launch vehicle occurs at time τ_1. With a guessed optimal state at τ_1, the exo-atmospheric algorithm solves the optimal vacuum trajectory to the orbital insertion point and returns an optimal costate required at τ_1, denoted by $\hat{\boldsymbol{p}}$. Then the TPBVP for the endo-atmospheric portion must satisfy and the special boundary condition $\boldsymbol{p}(\tau_1) = \hat{\boldsymbol{p}}$. The special TPBVP in the endo-atmospheric portion becomes

$$\boldsymbol{x}' = \boldsymbol{f}_x(\tau, \boldsymbol{x}, \boldsymbol{p}) \tag{13}$$

$$\boldsymbol{x}(0) = \boldsymbol{x}_0 \tag{14}$$

$$\boldsymbol{p}' = \boldsymbol{f}_p(\tau, \boldsymbol{x}, \boldsymbol{p}) \tag{15}$$

$$\boldsymbol{p}(\tau_1) = \hat{\boldsymbol{p}}(\tau_1) \tag{16}$$

where $\boldsymbol{f}_x$ and $\boldsymbol{f}_p$ are the resulting right-hand sides of the state and costate equations once the controls are eliminated.

The time interval $[0,\ \tau_1]$ is divided into N sub-intervals of the same length $h = \tau_1/N$. Let $\boldsymbol{x}_i = \boldsymbol{x}(ih)$ and $\boldsymbol{p}_i = \boldsymbol{p}(ih)$ be the value of the solution at the node $\tau_i = ih$, $i = 0, \ldots, N$. The middle point between τ_{i-1} and τ_i is denoted by $\tau_{i-1/2} = \tau_i - h/2$. Therefore the differential equations (13) and (15) can be approximated by central finite difference at $\tau_{i-1/2}$:

$$\frac{1}{h}(\boldsymbol{x}_i - \boldsymbol{x}_{i-1}) = \boldsymbol{f}_x\left(\tau_{i-1/2}, \frac{\boldsymbol{x}_i + \boldsymbol{x}_{i-1}}{2}, \frac{\boldsymbol{p}_i + \boldsymbol{p}_{i-1}}{2}\right), \quad i = 1, \ldots, N \tag{17}$$

$$\frac{1}{h}(\boldsymbol{p}_i - \boldsymbol{p}_{i-1}) = \boldsymbol{f}_p\left(\tau_{i-1/2}, \frac{\boldsymbol{x}_i + \boldsymbol{x}_{i-1}}{2}, \frac{\boldsymbol{p}_i + \boldsymbol{p}_{i-1}}{2}\right), \quad i = 1, \ldots, N \tag{18}$$

Re-organize above equations as

$$\boldsymbol{x}_i = \boldsymbol{x}_{i-1} + h\boldsymbol{f}_x\left(\tau_{i-1/2}, \frac{\boldsymbol{x}_i + \boldsymbol{x}_{i-1}}{2}, \frac{\boldsymbol{p}_i + \boldsymbol{p}_{i-1}}{2}\right), \quad i = 1, \ldots, N \tag{19}$$

$$\boldsymbol{p}_{i-1} = \boldsymbol{p}_i - h\boldsymbol{f}_p\left(\tau_{i-1/2}, \frac{\boldsymbol{x}_i + \boldsymbol{x}_{i-1}}{2}, \frac{\boldsymbol{p}_i + \boldsymbol{p}_{i-1}}{2}\right), \quad i = N, \ldots, 1 \tag{20}$$

The boundary condition is:

$$\boldsymbol{x}_0 = \boldsymbol{x}(0) \tag{21}$$

$$\boldsymbol{p}_N = \hat{\boldsymbol{p}}(\tau_1) \tag{22}$$

Let us take a set of initial guess on $\boldsymbol{x}_i (i = 0, 1, \ldots, N)$ and denote it as $\boldsymbol{x}_i{}^{(0)} (i = 0, 1, \ldots, N)$, where $\boldsymbol{x}_0{}^{(0)} = \boldsymbol{x}_0$ as required by the condition (21). Let $\boldsymbol{p}_i{}^{(0)} (i = 0, 1, \ldots, N)$ be the corresponding set of costate vectors that satisfy the co-state finite-difference equations Eq. (20). By the given boundary condition (22) we must have $\boldsymbol{p}_N^{(0} = \hat{\boldsymbol{p}}(\tau_1)$. With this known condition and $\boldsymbol{x}_i$ replaced by $\boldsymbol{x}_i{}^{(0)}$, Eq. (20) for $i = N$ becomes a fixed-point equation on $\boldsymbol{p}_{N-1}^{(0)}$:

$$\boldsymbol{p}_{N-1}^{(0)} = \boldsymbol{\eta}_{N-1}(\boldsymbol{p}_{N-1}^{(0)}) \tag{23}$$

where $\boldsymbol{\eta}_{N-1}(\boldsymbol{p}_{N-1}^{(0)})$ is the right hand side of Eq. (20) with $i = N - 1$. Once the solution of $\boldsymbol{p}_{N-1}^{(0)}$ is obtained, $\boldsymbol{p}_{N-2}^{(0)}$ can be found in a similar way by a fixed-point equation in $\boldsymbol{p}_{N-2}^{(0)}$. Repeating this process successively, we can conclude that after taking a set of initial guess on $\boldsymbol{x}_i (i = 1, \ldots, N)$, the costate $\boldsymbol{p}_i^{(0)}$ at the i-the node can be determined by a fixed-point equation:

$$\boldsymbol{p}_i^{(0)} = \boldsymbol{\eta}_i(\boldsymbol{p}_i^{(0)}), \quad i = N - 1, \ldots, 0 \tag{24}$$

The above process is used to find the solution for each $\boldsymbol{p}_i^{(0)}$, $i = 1, \ldots, N - 1$. Now denote the solution of the state finite-difference equation (19) by $\boldsymbol{x}_i{}^{(1)} (i = 0, 1, \ldots, N)$ with $\boldsymbol{p}_i$ in Eq. (19) replaced by the just found $\boldsymbol{p}_i{}^{(0)}$, where and note that $\boldsymbol{x}_0^{(1)} = \boldsymbol{x}_0$ again as required. In a similar fashion Eq. (19) for $i = 1$ becomes a fixed-point equation on $\boldsymbol{x}_1^{(1)}$:

$$\boldsymbol{x}_1^{(1)} = \boldsymbol{\zeta}_1(\boldsymbol{x}_1^{(1)}) \tag{25}$$

where $\boldsymbol{\zeta}_1(\boldsymbol{x}_1^{(1)})$ is the right hand side of Eq. (19) at $i = 1$.

After the solution of $\boldsymbol{x}_1^{(1)}$ is obtained, the fixed-point equation for $\boldsymbol{x}_2^{(1)}$ is formed in the same way. Repeating this process successively, the state $\boldsymbol{x}_i^{(1)}$ at i_{th} node can be obtained by a fixed-point equation:

$$\boldsymbol{x}_i^{(1)} = \boldsymbol{\zeta}_i(\boldsymbol{x}_i^{(1)}), \quad i = 1, \ldots, N \tag{26}$$

Now we compare $\boldsymbol{x}_i{}^{(1)}$ with the initial guess $\boldsymbol{x}_i{}^{(0)} (i = 1, \ldots, N)$. If they are sufficiently close to each other, stop and an endo-atmospheric ascent trajectory satisfying the finite-difference equation system Eqs. (19–22) has been found. Otherwise using the newly obtained $\boldsymbol{x}_i{}^{(1)} (i = 1, \ldots, N)$ to replace $\boldsymbol{x}_i{}^{(1)} (i = 1, \ldots, N)$ in Eq. (20), we will repeat the procedure to find $\boldsymbol{p}_i{}^{(2)} (i = 0, 1, \ldots, N)$. Therefore there is a total of three fixed-point iterations used for solving the formulated TPBVP: two inner-loop fixed-point iterations described in Eqs. (24) and (26) above, and one outer-loop fixed-point iteration that determines the junction point τ_1 between the endo- and exo-atmospheric portion of the complete ascent trajectory.

Described above is a brief review of the fixed-point formulation for solving the special form of TPBVP in endo-atmospheric ascent portion. The convergence of the fixed-point iterations is still an open question. In the following some additional ideas are discussed to facilitate the convergence of the fixed-point iterations.

Contraction Mapping

There are totally three fixed-point iterations in the presented algorithm. To avoid possible confusion and for convenience of expression, a general fixed-point iteration expression will be used in discussion in this section.

Consider a fixed-point equation

$$z = f(z) \tag{27}$$

The fixed-point iteration applied to this equation is:

$$\hat{z}^{(j+1)} = f(z^{(j)}), \quad j = 0, 1, 2, \ldots \tag{28}$$

where

$$z^{(j)} = \hat{z}^{(j)}, \quad j = 1, 2, \ldots \tag{29}$$

The convergence of this iteration depends on whether the mapping on the right hand of Eq. (27) is a contractive. For a fixed-point iteration, it is possible to facilitate the convergence of the iteration through redefining the fixed-point iteration with an appropriate coefficient θ in the following modified equation (cf. Isaacson *et al* 1994).

$$z^{(j+1)} = \theta \hat{z}^{(j+1)} + (1 - \theta) z^{(j)}, \quad j = 0, 1, 2, \ldots \tag{30}$$

With Eq. (28) and Eq. (30), we have just defined a new fixed-point equation:

$$z = F(z) := \theta f(z) + (1 - \theta) z \tag{31}$$

Evidently the solutions to Eq. (31) and Eq. (27) are the same for any $\theta \neq 0$. The difference is that in the cases where fixed-point iteration (27) does not converge, we may be able to find a proper θ to enable the convergence of the fixed-point iteration (34). In other words, we are trying to formulate a contraction mapping $z = F(z)$ instead of solving the fixed-point iteration (27) directly. It should be mentioned that θ can be either a scalar or a matrix. See Ref.[37] for more. Reference[38] proposes and compares several numerical techniques toward the solution of the above special TPBVP.

References

[1] Smith, I. E., "General Formulation of the Iterative Guidance Mode," NASA TM X-53414, March, 1966.

[2] McHenry, R. L., Brand, T. J., Long, A. D., Cockrell, B. F., and Thibodeau III, J. R., "Space Shuttle Ascent Guidance, Navigation, and Control," *Journal of the Astronautical Sciences*, Vol. XXVII, No. 1, 1979, pp. 1-38.

[3] Hanson, J. M, Shrader, M. W., and Cruzen, A,"Ascent Guidance Comparisons," *Proceedings of the AIAA Guidance, Navigation, and Control Conference*, Scottsdale, AZ, August 1-3, 1994.

[4] Brown, K. R., Harrold, E. F., Johnhson, G. W., "Some New Results on Space Shuttle Atmospheric Ascent Optimization," AIAA Paper No. 70-978, 1970.

[5] Leung, M. S. K., and Calise, A. J., "Hybrid Approach to Near-Optimal Launch Vehicle Guidance," *Journal of Guidance, Control, and Dynamics*, Vol. 17, No.5, 1994, pp. 881-888.

[6] Calise, A. J, Melamed, N., and Lee, S., "Design and Evaluation of a Three-Dimensional Optimal Ascent Guidance Algorithm," *Journal of Guidance, Control, and Dynamics*, Vol. 21, No. 6, 1998, pp. 867–875.

[7] Gath, P. F., and Calise, A. J., "Optimization of Launch Vehicle Ascent Trajectories with Path Constraints and Coast Arcs," *Journal of Guidance, Control, and Dynamics*, Vol. 24, No. 2, 2001, pp. 296–304.

[8] Calise, A. J., and Brandt, N., "Generation of Launch Vehicle Abort Trajectories Using a Hybrid Optimization Method," AIAA paper 2002-4560, AIAA Guidance, Navigation, and Control Conference, Monterey, CA, August 5–8, 2002.

[9] Dukeman, G.A., "Atmospheric Ascent Guidance for Rocket-Powered Launch Vehicles," AIAA paper 2002-4559, AIAA Guidance, Navigation, and Control Conference, Monterey, CA, August 5–8, 2002.

[10] Dukeman, G., and Calise, A., "Enhancements to an Atmospheric Ascent Guidance Algorithm," AIAA paper 2003-5638, August 2003.

[11] Dukeman, G., "Closed-Loop Nominal and Abort Atmospheric Ascent Guidance for Rocket-Powered Launch Vehicles," Ph.D. Dissertation, Georgia Institute of Technology, May 2005.

[12] Lu, P., Sun, H., and Tsai, B., "Closed-Loop Endo-Atmospheric Ascent Guidance," *Journal of Guidance, Control, and Dynamics*, Vol. 26, No. 2, 2003, pp. 283-294.

[13] Gath, P. F., and Well, K. H., *HISTOS Technical Report 1*, Institute of Flight Mechanics and Control, University of Stuttgart, Germany, June, 1999.

[14] Bryson, A. E, and Y. C. Ho, *Applied Optimal Control*, Hemisphere, Washington, D. C., 1975, pp. 42–87.

[15] Vinh, N. X., "General Theory of Optimal Trajectory for Rocket Flight in a Resisting Medium," *Journal of Optimization Theory and Applications*, Vol. 11, No. 2, 1973, pp. 189–202.

[16] Lu, P., "Nonlinear Systems with Control and State Constraints," *Optimal Control Applications and Methods*, Vol. 18, 1997, pp. 313-326.

[17] Betts, J. T., and Huffman, W. P., *Sparse Optimal Control Software: Version 5.0*, The Boeing Company, June 2000, Seattle, WA.

[18] Ross, I. M., and Fahroo, F., *User's Manual for DIDO 2001 (α): A MATLAB^{TM} Application Package for Dynamic Optimization*, Technical Report NPS-AA-01-003, October 2001, Naval Postgraduate School, Monterey, CA.

[19] Corvin, M. A., "Ascent Guidance for a Winged Boost Vehicle," NASA CR-172083, August, 1988.

[20] Keller, H. B., *Numerical Methods for Two-Point Boundary-Value Problems*, Blaisdell Publishing Company, Waltham, MA, 1968, pp. 91–100.

[21] Stoer, J., and Bulirsch, R., *Introduction to Numerical Analysis*, Springer-Verlag, New York, 1980, pp. 256-262.

[22] Press, W. H. *et al*, *Numerical Recipes in FORTRAN*, Cambridge University Press, Cambridge, UK, 1992, pp. 753–759.

[23] McAdoo, S. F., Jezewski, D. J., and Dawkins, G.S., "Development of a Method for Optimal Maneuver Analysis of Complex Space Missions", NASA TN D-7882, April, 1975.

[24] Brown, K. R., Harrold, E. F., and Johnson, G. W., "Rapid Optimization of Multiple-Burn Rocket Trajectories," NASA CR-1430, September 1969.

[25] Jezewski, D. J.,"Optimal Analytic Multiburn Trajectories," *AIAA Journal*,Vol. 10, No. 5, 1972, pp. 680–685.

[26] Jezewski, D. J.,"N-Burn Optimal Analytic Trajectories," *AIAA Journal*,Vol. 11, No. 10, 1973, pp. 1373–1376.

[27] Lu, P., Zhang, L., and Sun, H., "Ascent Guidance for Responsive Launch: a Fixed-Point Approach," AIAA Paper 2005-6453, August 2005.

[28] Powell, M. J. D., "A Hybrid Method for Nonlinear Equations," Chapt. 6, *Numerical Methods for Nonlinear Algebraic Equations*, edited by Rabinpwitz, P., Gorden and Breach Science Publisher, Inc., New York, 1970, pp. 87–114.

[29] Hargraves, C. R., and Paris, S. W., "Direct Trajectory Optimization Using Nonlinear Programming and Collocation," *Journal of Guidance, Control, and Dynamics*, Vol. 10, No. 4, 1987, pp. 338-342.

[30] Jezewski, D. J.,"An Optimal, Analytic Solution to the Linear Gravity, Constant-Thrust Trajectory Problem," *Journal of Spacecraft and Rockets*, Vol. 8, No. 1, 1971, pp. 793–796.

[31] Lawden, D. F., *Optimal Trajectories for Space Navigation*, Butterworth, London, UK, 1963, pp. 54–68.

[32] Robbins, H. M., "Optimality of Intermediate-Trust Arcs of Rocket Trajectories," *AIAA Journal*, Vol. 3, No. 6, 1965, pp. 1094-1098.

[33] Danby, J. M. A., *Fundamentals of Celestial Mechanics*, 2nd edition, Willmann-Bell Inc., Richmond, VA, 1988, pp. 162–177.

[34] Goodyear, W., "Completely General Closed-Form Solution for Coordinates and Partial Derivatives of the Two-Body Problem," *The Astronomical Journal*, Vol. 70, No. 3, 1965, pp. 189–192.

[35] Pontryagin, L. S., Boltyanskii,V. G., Gramkreledze, Q. V., and Mishchenko, E. F., *The Mathematical Theory of Optimal Processes*, Intersciences, New York, 1962, pp. 20–21.

[36] Bradt, J., Jessick, M., and Hardtla, W., 1987, Optimal Guidance for Future Space Applications, *AIAA Guidance, Navigation and Control Conference*, Monterey, CA.

[37] Isaacson, E., and Keller, H., 1994, *Analysis of Numerical Methods*, Dover Publications, Inc., Mineola, NY.

[38] Zhang, L., and Lu, P., "Fixed-Point Algorithms for Optimal trajectories of Launch Vehicles," *Engineering Optimization*, Vol. 40, No. 4, 2008, pp. 361-381

[39] Hämmerlin, G., and Hoffmann, K., 1991, *Numerical Mathematics*, Springer-Verlag New York, Inc., New York.

[40] Justus, C. G., and Leslie, F. W., "The NASA/MSFC Earth Global Reference Atmospheric Model – 2007 Version (Earth-GRAM2007)," NASA/TM-2008-215581, November 2008.

[41] Dukeman, G., and Hill, A., "Rapid Trajectory Optimization for the ARES I Launch Vehicle," AIAA Paper 2008-6288, August, 2008.

[42] Brauer, G., Cornick, D., Habeger, A., and Peterson, F., "Program to Optimize Simulated Trajectories (POST). Volume 3: Programmer's Manual," Final Report, Martin Marietta Corp., Denver, CO, April 1975.

DISTRIBUTION LIST

DTIC/OCP
8725 John J. Kingman Rd, Suite 0944
Ft Belvoir, VA 22060-6218   1 cy

AFRL/RVIL
Kirtland AFB, NM 87117-5776   2 cys

Official Record Copy
AFRL/RVES/Frank R. Chavez   1 cy

This page is intentionally left blank.